Synthesis and spectroscopy of upconverting lanthanide-doped nanocrystals
Boyer, John-Christopher
ProQuest Dissertations and Theses; 2007; ProQuest
pg. n/a

Synthesis and Spectroscopy of Upconverting Lanthanide-Doped Nanocrystals

John-Christopher Boyer

A Thesis
In
The Department
of
Chemistry and Biochemistry

Presented in Partial Fulfilment of the Requirements
for the Degree of Doctor of Philosophy at
Concordia University
Montreal, Quebec, Canada

December 2006

Library and
Archives Canada

Published Heritage
Branch

395 Wellington Street
Ottawa ON K1A 0N4
Canada

Bibliothèque et
Archives Canada

Direction du
Patrimoine de l'édition

395, rue Wellington
Ottawa ON K1A 0N4
Canada

Your file Votre référence
ISBN: 978-0-494-30116-6
Our file Notre référence
ISBN: 978-0-494-30116-6

NOTICE:
The author has granted a non-exclusive license allowing Library and Archives Canada to reproduce, publish, archive, preserve, conserve, communicate to the public by telecommunication or on the Internet, loan, distribute and sell theses worldwide, for commercial or non-commercial purposes, in microform, paper, electronic and/or any other formats.

The author retains copyright ownership and moral rights in this thesis. Neither the thesis nor substantial extracts from it may be printed or otherwise reproduced without the author's permission.

AVIS:
L'auteur a accordé une licence non exclusive permettant à la Bibliothèque et Archives Canada de reproduire, publier, archiver, sauvegarder, conserver, transmettre au public par télécommunication ou par l'Internet, prêter, distribuer et vendre des thèses partout dans le monde, à des fins commerciales ou autres, sur support microforme, papier, électronique et/ou autres formats.

L'auteur conserve la propriété du droit d'auteur et des droits moraux qui protège cette thèse. Ni la thèse ni des extraits substantiels de celle-ci ne doivent être imprimés ou autrement reproduits sans son autorisation.

In compliance with the Canadian Privacy Act some supporting forms may have been removed from this thesis.

While these forms may be included in the document page count, their removal does not represent any loss of content from the thesis.

Conformément à la loi canadienne sur la protection de la vie privée, quelques formulaires secondaires ont été enlevés de cette thèse.

Bien que ces formulaires aient inclus dans la pagination, il n'y aura aucun contenu manquant.

Canada

Reproduced with permission of the copyright owner. Further reproduction prohibited without permission.

ABSTRACT

Synthesis and Spectroscopy of Upconverting Lanthanide-Doped Nanocrystals

John-Christopher Boyer
Concordia University, 2006

In the past two decades it has been widely demonstrated that the optical properties of select inorganic materials may be modified by changing either their size or shape on the nanometer level (sub-nanometer to 100 nm length scale). Much of the early research on this topic focused on semiconducting nanocrystals, where it has been effectively demonstrated that reducing particle size below their Bohr radius produced a characteristic blue shift of the band gap absorption. A little over a decade after the initial work on semiconducting nanocrystals, the first scientific articles on insulating nanocrystals doped with lanthanide ions started to appear. While numerous studies have focused on examining the luminescence generated by exciting with ultraviolet (UV) light, very few have examined the upconversion phenomenon in nanocrystalline materials. Upconversion is the generation of higher energy light from lower energy radiation typically through the use of lanthanide ions doped into a solid state host. Much of the interest in upconverting nanocrystalline materials is due to their prospective application as fluorescent biological labels.

In this thesis the synthesis, spectroscopic, and upconversion properties of lanthanide-doped nanocrystalline materials will be discussed. We report on our efforts to date to achieve viable upconversion luminescence from Ho^{3+} doped nanocrystalline Y_2O_3 and $Gd_3Ga_5O_{12}$ prepared via the combustion synthesis. These studies have determined that, while upconversion occurs in Y_2O_3 bulk samples, it is severely reduced

or nonexistent in the nanocrystal samples. This behaviour is attributed to the presence of high vibrational energies, 1500 and 3350 cm^{-1}, due to adsorbed atmospheric CO_3^{2-} and OH^- anions, respectively, on the surface of the nanocrystals. A substantial increase in the upconversion efficiencies was observed in the case of the garnet ($Gd_3Ga_5O_{12}$) nanocrystals due to considerably less surface contamination. The effect of Yb^{3+} co-doping on the upconversion luminescence in the $Gd_3Ga_5O_{12}$ sample will also be introduced.

We also evaluate the spectroscopic properties of lutetium oxide nanocrystals doped with trivalent europium ($Lu_2O_3:Eu^{3+}$) prepared by the same combustion synthesis technique. These results are compared and contrasted to those of a bulk $Lu_2O_3:Eu^{3+}$ sample. In the case of Lu_2O_3 we observe significant changes in the luminescence behaviour that we attribute to the vastly different particle sizes of the two different materials.

Finally, we present a new procedure for synthesizing $NaYF_4:Er^{3+}$, Yb^{3+} nanoparticles that are capable of colloidal dispersion in non-polar organic solvents. The highly luminescent nanoparticles are synthesized via the thermal decomposition of trifluoroacetate precusors in a mixture of oleic acid and octadecene. The Er^{3+}, Yb^{3+} and Tm^{3+}, Yb^{3+} doped cubic $NaYF_4$ nanocrystals exhibit green/red and blue upconversion luminescence, respectively under 980 nm laser excitation with low power densities while colloidally dispersed. A brief discussion on our current attempts and future efforts towards modifying the nanoparticles surface will also be given.

ACKNOWLEDGMENTS

I would like to express my extreme gratitude to my supervisor Dr. John A. Capobianco for giving me the opportunity to work in his lab over the past seven years. You provided me with the freedom to try what I wanted and it resulted in big things (actually very small things).

I wish to thank our collaborators, Dr. Marco Bettinelli and Dr. Adolfo Speghini, from the Università di Verona for their scientific insights and encouragement. I would also like to thank Erica Viviani (Università di Verona) for preparing many of the samples utilized in this study.

I must also express my gratitude to Dr. Louis Cuccia not only for his suggestions towards the synthesis but also for his friendship during the past few years.

To the members of my thesis committee, Prof. Ann M. English and Prof. Peter Bird, I wish to express my thanks and appreciation for your encouragement and support throughout the years. I am also grateful to Prof. Anna M. Ritcey (Université Laval) for agreeing to serve as the external on my thesis examination committee.

I must also extend my appreciation to all present and former colleagues of the Lanthanide Research Group, especially my friends and colleagues Sean Hughes, Rafik Naccache, and Fiorenzo Vetrone. Over the course of my degree they have made the lab environment not only entertaining and interesting but also intellectually stimulating as well. I would also like to deeply thank Nabil Al-Yassir for his companionship as well as for the many interesting scientific discussions.

I would like to sincerely thank my parents, Roland and Pollyanna, for their support and encouragement through these past years. I would also like to express my

gratitude to my sister, Danielle Becker, and her family for believing in me. Most of all, I would like to thank my wife Danielle for her everlasting love and without whose unfailing support this thesis may have never been completed. You have always been there for me during difficult times and I hope I am able to return the favour someday.

This work was financially supported by grants from the Natural Sciences and Engineering Research Council (NSERC) of Canada. I would like to acknowledge NSERC, Le Fonds Québécois de la Recherche sur la Nature et les Technologies (FQRNT) and Concordia University for personal funding during my Ph.D. studies.

This thesis is dedicated to my wife

Danielle Menzies-Toman

I have and always will love you

"Those who dare to fail miserably can achieve greatly."

- John F. Kennedy

TABLE OF CONTENTS

LIST OF FIGURES x

LIST OF TABLES xv

CONTRIBUTIONS OF AUTHORS xvi

Chapter 1

General Introduction .... - 1 -

1.1. PREAMBLE .... - 2 -
1.2. THE LANTHANIDES .... - 5 -
1.3. UPCONVERSION .... - 12 -
  1.3.1. Excited State Absortion (ESA) Upconversion .... - 14 -
  1.3.2. Energy Transfer Upconversion (ETU) .... - 15 -
  1.3.3. Photon Avalanche Upconversion .... - 17 -
1.4. LANTHANIDE DOPED UPCONVERTING NANOCRYSTALS .... - 19 -
1.5. UPCONVERTING NANOCRYSTALS AS BIOLABELS .... - 27 -
1.6. STATEMENT OF THE PROBLEM .... - 33 -
1.7. OUTLINE .... - 35 -

Chapter 2

Optical Spectroscopy and Upconversion Studies of Ho^{3+} Doped Bulk and Nanocrystalline Y_2O_3 .... - 41 -

2.1. ABSTRACT .... - 42 -
2.2. INTRODUCTION .... - 43 -
2.3. EXPERIMENTAL .... - 46 -
  2.3.1. Sample preparation .... - 46 -
  2.3.2. IR spectroscopy .... - 46 -
  2.3.3. Luminescence spectroscopy .... - 47 -
  2.2.4 Luminescence decay times measurements .... - 47 -
2.4. RESULTS AND DISCUSSION .... - 48 -
  2.4.1. Particle Size .... - 48 -
  2.4.2. Luminescence spectroscopy .... - 48 -
  2.4.3. Emission Decay Times .... - 54 -
  2.3.4. Upconversion upon excitation into the $^5F_5$ *manifold* .... - 57 -
  2.4.5. Upconversion upon excitation into the $^5I_4$ *manifold* .... - 62 -
2.5. CONLUSIONS .... - 66 -
2.6. AUTHOR'S NOTES AND SIGNIFICANCE OF THIS PAPER .... - 67 -

Chapter 3

Variation of Fluorescence Lifetimes and Judd-Ofelt Parameters between Eu^{3+} Doped Bulk and Nanocrystalline Cubic Lu_2O_3 .... - 68 -

3.1. ABSTRACT .... - 69 -
3.2. INTRODUCTION .... - 70 -
3.3. EXPERIMENTAL .... - 73 -
  3.3.1. Samples preparation .... - 73 -
  3.3.2. Emission spectroscopy .... - 73 -
  3.3.3. Decay times measurements .... - 74 -
3.4. RESULTS AND DISCUSSION .... - 75 -
  3.4.1. Luminescence spectroscopy .... - 75 -
  3.4.2. Site-Selective Spectroscopy .... - 82 -
  3.4.3. Luminescence Decay Times .... - 86 -
  3.4.4. Judd-Ofelt Parameters .... - 90 -
3.5. CONCLUSIONS .... - 93 -
3.6. AUTHOR'S NOTES AND SIGNIFICANCE OF THIS PAPER .... - 94 -

Chapter 4

Investigation of the Upconversion Processes in Nanocrystalline $Gd_3Ga_5O_{12}$:Ho^{3+} .... - 95 -

4.1. ABSTRACT .... - 96 -
4.3. EXPERIMENTAL .... - 99 -
4.4. RESULTS AND DISCUSSION .... - 101 -
4.5. CONLUSIONS .... - 109 -
4.6. AUTHOR'S NOTES AND SIGNIFICANCE OF THIS PAPER .... - 110 -

Chapter 5

Yb^{3+} Ion as a Sensitizer for the Upconversion Luminescence in Nanocrystalline $Gd_3Ga_5O_{12}$:Ho^{3+} .... - 111 -

5.1. ABSTRACT .... - 112 -
5.2. INTRODUCTION .... - 113 -
5.3. EXPERIMENTAL .... - 115 -
5.4. RESULTS AND DISCUSSION .... - 117 -
5.5. CONLUSIONS .... - 127 -
5.6. AUTHOR'S NOTES AND SIGNIFICANCE OF THIS PAPER .... - 128 -

Chapter 6

Synthesis of Colloidal Upconverting $NaYF_4$ Nanocrystals Doped with Er^{3+}, Yb^{3+} and Tm^{3+}, Yb^{3+} via Thermal Decomposition of Lanthanide Trifluoroacetate Precursors. - 129 -

6.1. SUPPORTING INFORMATION - 137 -
6.1.1. Synthesis of Ln^{3+} doped $NaYF_4$ nanocrystals - 137 -
6.1.2. NMR Measurements - 138 -
6.1.3. Powder X-ray Diffraction Analysis - 139 -
6.1.4. Transmission Electron Microscopy (TEM) Studies - 139 -
6.1.5. Visible and NIR Room Temperature Emission Spectroscopy (λ_{exc} = 977 nm) - 139 -
6.2. AUTHOR'S NOTES AND SIGNIFICANCE OF THIS PAPER - 144 -

Chapter 7

Synthesis of Colloidal Upconverting $NaYF_4$: Er^{3+}/Yb^{3+} and Tm^{3+}/Yb^{3+} Monodisperse Nanocrystals - 145 -
7.1. SUPPORTING INFORMATION - 162 -
7.1.1. Synthesis of Ln^{3+} doped $NaYF_4$ nanocrystals - 162 -
7.1.2. NMR Measurements - 164 -
7.1.3. Powder X-ray Diffraction Analysis - 164 -
7.1.4. Transmission Electron Microscopy (TEM) Studies - 164 -
7.1.5. Visible and NIR Room Temperature Upconversion Emission Spectroscopy (λ_{exc} = 980 nm) - 165 -
7.2. AUTHOR'S NOTES AND SIGNIFICANCE OF THIS PAPER - 168 -

Chapter 8

Conclusions and Future Work - 169 -
8.1. CONCLUSIONS - 170 -
8.2 FUTURE WORK - 176 -
REFERENCES - 178 -

LIST OF FIGURES

Figure 1.1. The periodic table of the elements with the lanthanides (yellow) and similar ions (blue) highlighted. .... - 6 -

Figure 1.2. The Dieke diagram: an overview of the experimentally observed 4*f* levels of the trivalent lanthanide ions (Ln^{3+}) in $LaCl_3$ .... - 11 -

Figure 1.3. Schematic representation of an Excited State Absorption (ESA) upconversion mechanism in a simple three-level ion. .... - 15 -

Figure 1.4. Schematic representation of an Energy Transfer Upconversion (ETU) mechanism in simple three-level ions. .... - 16 -

Figure 1.5. Schematic representation of an Photon avalanche upconversion in modified three-level ions. .... - 18 -

Figure 1.6. Reactor for the combustion synthesis of nanocrystalline Y_2O_3 and $Gd_3Ga_5O_{12}$. .... - 23 -

Figure 1.7. Schematic representation of the thermolysis reaction and photo of the experimental setup. .... - 26 -

Figure 1.8. Illustration of a sandwich type assay utilizing an upconverting label. .... - 29 -

Figure 1.9. Diagram representing a conventional FRET assay. .... - 30 -

Figure 1.10. Diagram representing a FRET assay using upconverting technology. ...... - 32 -

Figure 2.1. Room temperature luminescence of bulk Y_2O_3:Ho^{3+} upon excitation at 457.9 nm. (i) $^5F_3 \rightarrow {}^5I_8$ (ii) $({}^5F_4, {}^5S_2) \rightarrow {}^5I_8$ (iii) $^5F_5 \rightarrow {}^5I_8$ (iv) $({}^5F_4, {}^5S_2) \rightarrow {}^5I_7$. .... - 49 -

Figure 2.2. Room temperature luminescence of nanocrystalline Y_2O_3:Ho^{3+} upon excitation at 457.9 nm. (i) $^5F_3 \rightarrow {}^5I_8$ (ii) $({}^5F_4, {}^5S_2) \rightarrow {}^5I_8$ (iii) $^5F_5 \rightarrow {}^5I_8$ (iv) $({}^5F_4, {}^5S_2) \rightarrow {}^5I_7$. .... - 50 -

Figure 2.3. Upconverted emission of bulk Ho^{3+} doped Y_2O_3 at room temperature upon 646 nm excitation, showing (i) $^5F_3 \rightarrow {}^5I_8$ and (ii) $({}^5F_4, {}^5S_2) \rightarrow {}^5I_8$. .... - 58 -

Figure 2.4. Upconverted emission of Ho^{3+} doped Y_2O_3 nanocrystals at room temperature upon 646 nm excitation, showing (i) $^5F_3 \rightarrow {}^5I_8$ and (ii) $({}^5F_4, {}^5S_2) \rightarrow {}^5I_8$. .... - 59 -

Figure 2.5. Power study of the ($^5F_4$, $^5S_2$) → $^5I_8$ transition in 10 mol% bulk Y_2O_3:Ho^{3+} at room temperature upon 646 nm excitation. Inset: Power dependence of the upconversion luminescence intensity observed with 646 nm excitation..- 61 -

Figure 2.6. Upconverted emission of bulk Ho^{3+} doped Y_2O_3 at room temperature upon 754 nm excitation, showing (i) $^5F_3$ → $^5I_8$, (ii) ($^5F_4$, $^5S_2$) → $^5I_8$ and (iii) $^5F_5$ → $^5I_8$....- 63 -

Figure 2.7. Two excitation mechanisms for Ho^{3+} upconversion in Y_2O_3: (left) 646 nm excitation resulting in excited state absorption via the $^5I_7$ level (right) 754 nm excitation resulting in excited state absorption via the $^5I_7$ level. ....- 65 -

Figure 3.1. Room temperature orange-red luminescence of bulk and nanocrystalline Lu_2O_3:Eu^{3+} 1 mol% upon excitation at 257.25 nm. (i) $^5D_0$ → $^7F_0$ (ii) $^5D_0$ → $^7F_1$ (iii) $^5D_0$ → $^7F_2$ (C_{3i} emissions are noted by *.)..- 77 -

Figure 3.2. Detailed structure of $^5D_0$ → $^7F_0$, $^7F_1$ luminescence of bulk and nanocrystalline Lu_2O_3:Eu^{3+} 1 mol% at 78 K (λ_{exc} = 257.25 nm). (i) $^5D_0$ → $^7F_0$ (ii) $^5D_0$ → $^7F_1$.............- 80 -

Figure 3.3. Detailed structure of $^5D_0$ → $^7F_0$, $^7F_1$ luminescence of nanocrystalline Lu_2O_3:Eu^{3+} 1 mol% at RT and 78 K (λ_{exc} = 257.25 nm). (i) $^5D_0$ → $^7F_0$ (ii) $^5D_0$ → $^7F_1$.....- 81 -

Figure 3.4. Emission spectra $^5D_0$ → $^7F_1$ for selective excitation into the $^5D_0$ level (C_2 Exc. – 580.5 nm, C_{3i} Exc. 582.5 nm) of bulk and nanocrystalline Lu_2O_3:Eu^{3+} 1 mol% at RT. Note the presence of weak C_{3i} peak at 582.5 nm in both spectra obtained under C_2 excitation (marked with arrow)..- 84 -

Figure 3.5. Emission spectra $^5D_0$ → $^7F_1$ for selective excitation into the $^5D_0$ level (C_2 Exc. – 580.5 nm, C_{3i} Exc. 582.5 nm) of bulk and nanocrystalline Lu_2O_3:Eu^{3+} 1 mol% at 78K. Note the presence of weak C_{3i} peak at 582.5 nm in both spectra obtained under C_2 excitation (marked with arrow)..- 85 -

Figure 3.6. Dependence of the $^5D_0$ lifetime for the Eu^{3+} C_2 and C_{3i} sites on the index of refraction of the media n_{med} at T = 298 K...- 88 -

Figure 4.1. Room temperature upconverted luminescence of nanocrystalline $Gd_3Ga_5O_{12}$: Ho^{3+} upon excitation at 647 nm or 756 nm. Room temperature emission spectrum under

λex = 457.9 nm is also shown for comparative purposes. (i) $^5F_3 \rightarrow {}^5I_8$ (ii) ($^5F_4$, $^5S_2$) → $^5I_8$ (iii) $^5F_5 \rightarrow {}^5I_8$ .... - 102 -

Figure 4.2. Room temperature power dependence of the upconverted ($^5F_4$, $^5S_2$) → $^5I_8$ luminescence intensity for the nanocrystalline $Gd_3Ga_5O_{12}$: Ho^{3+} observed with 647 nm and 756 nm excitation. .... - 104 -

Figure 4.3. Principal ESA upconversion mechanisms for 647 nm excitation (left) and 756 nm excitation (right) in nanocrystalline $Gd_3Ga_5O_{12}$: Ho^{3+}. .... - 106 -

Figure 5.1. Room temperature (a) emission spectrum under λ_{ex} = 457.9 nm shown for comparative purposes. (b) anti-Stokes luminescence of nanocrystalline Gd3Ga5O12: Ho^{3+}, Yb^{3+} upon excitation at 978 nm. (i) ($^5F_4$, $^5S_2$) → $^5I_8$ (ii) $^5F_5 \rightarrow {}^5I_8$ (iii) ($^5F_4$, $^5S_2$) → $^5I_7$ Inset: Weak blue $^5F_3 \rightarrow {}^5I_8$ luminescence observed under (a) 457.9 nm and (b) 978 nm excitation. Extra peak character under 978 nm excitation is noted by *. .... - 118 -

Figure 5.2. Room temperature power dependence of the upconverted blue $^5F_3 \rightarrow {}^5I_8$, green ($^5F_4$, $^5S_2$) → $^5I_8$ and red $^5F_5 \rightarrow {}^5I_8$ luminescence intensity for nanocrystalline $Gd_3Ga_5O_{12}$: Ho^{3+}, Yb^{3+} upon 978 nm excitation. .... - 121 -

Figure 5.3. Temporal evolution of the green ($^5F_4$, $^5S_2$) → $^5I_8$ and red $^5F_5 \rightarrow {}^5I_8$ upconverted luminescence in nanocrystalline $Gd_3Ga_5O_{12}$: Ho^{3+}, Yb^{3+} under 978 nm excitation. .... - 123 -

Figure 5.4. Principal upconversion mechanisms for the anti-Stokes green ($^5F_4$, $^5S_2$) → $^5I_8$ (left) and red $^5F_5 \rightarrow {}^5I_8$ (right) luminescence in nanocrystalline $Gd_3Ga_5O_{12}$: Ho^{3+}, Yb^{3+} under 978 nm excitation .... - 124 -

Figure 6.1. Characterization data for $NaYF_4$: Er^{3+} 2%, Yb^{3+} 20% nanocrystals. A) Transmission electron microscopy (TEM) image. Inset: High resolution TEM (HRTEM) image of a single nanocrystal. B) Histogram of the particle sizes obtained from TEM images of ~1400 nanocrystals. C) Experimental powder x-ray diffraction (XRD) pattern (upper) and the calculated line pattern for α-$NaYF_4$ (lower). .... - 133 -

Figure 6.2. 1 wt.% colloidal solutions of nanocrystals in dichloromethane excited at 977 nm demonstrating upconversion luminescence. A) $NaYF_4$: Er^{3+} 2%, Yb^{3+} 20% solution

showing its transparency. B) Total upconversion luminescence of NaYF$_4$: Er^{3+} 2%, Yb^{3+} 20% solution. C, D) NaYF$_4$: Er^{3+} 2%, Yb^{3+} 20% upconversion viewed through green and red filters, respectively. E) NaYF$_4$: Tm^{3+} 2%, Yb^{3+} 20% solution. .... - 134 -

Figure 6.3. Luminescence emission spectra of 1 wt.% colloidal solutions of nanocrystals in dichloromethane excited at 977 nm. A) NaYF$_4$: Er^{3+} 2%, Yb^{3+} 20% and B) NaYF$_4$: Tm^{3+} 2%, Yb^{3+} 20%. .... - 135 -

Figure 6.4. The ^{1}H NMR spectrum of an undoped NaYF$_4$ sample dispersed in CDCl$_3$ recorded on a Varian 300 MHz spectrometer. Chemical shifts are reported in parts-per-million δ: 5.3-5.45 (broad, -HC=CH-), 2.0-2.1 (broad, CH$_3$-(CH$_2$)$_6$-CH$_2$-CH=CH-CH$_2$-(CH$_2$)$_6$-COOH), 1.2-1.4 (broad, -(CH$_2$)$_6$-) and 0.85-1.00 (broad, -CH$_3$). .... - 141 -

Figure 6.5. Power dependence of the upconverted emissions of 1 wt.% colloidal solutions of nanocrystals in dichloromethane excited at 977 nm. A) NaYF$_4$: Er^{3+} 2%, Yb^{3+} 20% and B) NaYF$_4$: Tm^{3+} 2%, Yb^{3+} 20%. In the case of the NaYF$_4$: Er^{3+} 2%, Yb^{3+} 20% sample, the straight lines are least-squares fit to the low power data points. At higher excitation densities the power dependence of the emissions are observed to level off due to saturation of the upconversion processes. For the NaYF$_4$: Tm^{3+} 2%, Yb^{3+} 20% sample, the least-squares fit to the data points give a value that is lower than the expected due to the saturation of the upconversion processes. .... - 142 -

Figure 6.6. The energy level diagrams of the Er^{3+}, Tm^{3+} and Yb^{3+} dopant ions and upconversion mechanisms following excitation with 977 nm. The full, dotted, and curly arrows represent emission, energy transfer and multiphonon relaxation processes, respectively. .... - 143 -

Figure 7.1. (A-B) Low resolution transmission electron micrographs of NaYF$_4$: 2% Er^{3+}, 20% Yb^{3+} sample showing uniformity of the particles. (C) High resolution micrographs of a single NaYF$_4$: 2% Er^{3+}, 20% Yb^{3+} particle showing lattice fringes. (D) Selected area electron diffraction pattern (SAED) of NaYF$_4$: 2% Er^{3+}, 20% Yb^{3+} particles. .... - 150 -

Figure 7.2. Experimental powder X-ray diffraction (XRD) patterns of α-NaYF$_4$, α-NaYF$_4$: 2% Er^{3+}, 20% Yb^{3+}, and α-NaYF$_4$: 2% Tm^{3+}, 20% Yb^{3+}nanocrystals. Calculated line pattern for α-NaYF$_4$ (bottom plot) is shown for reference. .... - 153 -

Figure 7.3. 1 wt.% colloidal solutions of nanocrystals in toluene excited with a 980 nm laser diode (power density = 100 W/cm^2) demonstrating upconversion luminescence. A) $NaYF_4$: 2% Er^{3+}, 20% Yb^{3+} solution showing its transparency. B) Total upconversion luminescence of $NaYF_4$: 2% Er^{3+}, 20% Yb^{3+} solution. C, D) $NaYF_4$: 2% Er^{3+}, 20% Yb^{3+} upconversion viewed through green and red filters, respectively. E) Total upconversion luminescence of $NaYF_4$: 2% Tm^{3+}, 20% Yb^{3+} solution.. - 155 -

Figure 7.4. Luminescence emission spectra of 1 wt.% colloidal solutions of nanocrystals in toluene excited with a 980 nm laser diode. A) $NaYF_4$: 2% Er^{3+}, 20% Yb^{3+} and B) $NaYF_4$: 2% Tm^{3+}, 20% Yb^{3+}.. - 156 -

Figure 7.5. Power dependence of the upconverted emissions of 1 wt.% colloidal solutions of nanocrystals in toluene excited at 980 nm. A) $NaYF_4$: 2% Er^{3+}, 20% Yb^{3+} and B) $NaYF_4$: 2% Tm^{3+}, 20% Yb^{3+}. In the case of the $NaYF_4$: 2% Er^{3+}, 20% Yb^{3+} sample, the straight lines are least-squares fits to the low power data points.............................. - 158 -

Figure 7.6. The energy level diagrams of the Er^{3+}, Tm^{3+} and Yb^{3+} dopant ions and upconversion mechanisms following 980 nm laser diode excitation. The full, dotted, and curly arrows represent emission, energy transfer and multiphonon relaxation processes, respectively. .... - 160 -

Figure 7.7. Histogram of the particle sizes obtained from TEM images of ~500 $NaYF_4$: 2% Er^{3+}, 20% Yb^{3+} nanocrystals (average particle size = 27.6 ± 1.6 nm)................. - 166 -

Figure 7.8. The ^1H NMR spectra of A) an undoped $NaYF_4$ sample and B) free oleic acid in $CDCl_3$ recorded on a Varian 300 MHz spectrometer. Chemical shifts for $NaYF_4$ sample are reported in parts-per-million δ: 5.3-5.45 (broad, -HC=CH-), 2.3-2.4 (broad, -CH_2-COOH), 2.0-2.1 (broad, CH_3-$(CH_2)_6$-CH_2-CH=CH-CH_2-$(CH_2)_6$-COOH), 1.2-1.4 (broad, -$(CH_2)_6$-) and 0.85-1.00 (broad, -CH_3). .... - 167 -

LIST OF TABLES

Table 1.1. Electron Configuration of Lanthanide Atoms and Ions................................- 8 -

Table 2.1. Decay times obtained from an exponential fit of the room temperature decay curves for the ($^5F_4$, $^5S_2$) → $^5I_8$ transition upon 457.9 nm excitation. ....- 55 -

Table 3.1. Observed transition energies from the emission spectra of bulk and nanocrystalline Lu_2O_3:Eu^{3+} 1 mol% at RT and 78 K. ....- 76 -

Table 3.2. $^5D_0$ luminescence decay times for bulk and nanocrystalline Lu_2O_3:Eu^{3+} 1 mol% at RT and 78 K (λ_{exc} = 257.25 nm)..- 90 -

Table 3.3. Ω_λ, Judd-Ofelt intensity parameters for the nanocrystalline and bulk Lu_2O_3:Eu^{3+} 1 mol%. R_{02}: ratio between the emission intensities of the $^5D_0 \rightarrow {}^7F_0$ and $^5D_0 \rightarrow {}^7F_2$ transitions. ....- 92 -

Table 5.1. Decay times obtained from an effective decay fit of the room temperature decay curves for the ($^5F_4$, $^5S_2$) → $^5I_8$ and $^5F_5$ → $^5I_8$ transitions for 457.9 nm and 978 nm excitations. ....- 120 -

Table 7.1. *d*-spacing values for $NaYF_4$: 2% Er^{3+}, 20% Yb^{3+}; $NaYF_4$: 2% Tm^{3+}, 20% Yb^{3+}; and $NaYF_4$ determined via electron diffraction (ED) and X-ray diffraction (XRD)..- 154 -

CONTRIBUTIONS OF AUTHORS

The following summarizes the contributions of each of the authors cited in this thesis.

CHAPTER 2: "Optical Spectroscopy and Upconversion Studies of Ho^{3+} Doped Bulk and Nanocrystalline Y_2O_3"

J. C. Boyer: experimental work and manuscript preparation
F. Vetrone: aided in experimental work
J. A. Capobianco: project supervisor
A. Speghini: sample preparation
M. Bettinelli: sample preparation

CHAPTER 3: "Variation of Fluorescence Lifetimes and Judd-Ofelt Parameters between Eu^{3+} Doped Bulk and Nanocrystalline Cubic Lu_2O_3"

J. C. Boyer: experimental work and manuscript preparation
F. Vetrone: aided in experimental work
J. A. Capobianco: project supervisor
A. Speghini: sample preparation
M. Bettinelli: sample preparation

CHAPTER 4: "Investigation of the upconversion processes in nanocrystalline $Gd_3Ga_5O_{12}:Ho^{3+}$"

J. C. Boyer: experimental work and manuscript preparation
F. Vetrone: aided in experimental work
J. A. Capobianco: project supervisor
A. Speghini: sample preparation
M. Zambelli: sample preparation
M. Bettinelli: sample preparation

CHAPTER 5: "Yb^{3+} ion as a sensitizer for the upconversion luminescence in nanocrystalline $Gd_3Ga_5O_{12}$:Ho^{3+}"

J. C. Boyer: experimental work and manuscript preparation

F. Vetrone: aided in experimental work

J. A. Capobianco: project supervisor

A. Speghini: sample preparation

M. Bettinelli: sample preparation

CHAPTER 6: "Synthesis of Colloidal Upconverting $NaYF_4$ Nanocrystals Doped with Er^{3+}, Yb^{3+} and Tm^{3+}, Yb^{3+} via Thermal Decomposition of Lanthanide Trifluoroacetate Precursors"

J. C. Boyer: experimental work and manuscript preparation

F. Vetrone: proofread manuscript

L. A. Cuccia: project collaborator

J. A. Capobianco: project supervisor

CHAPTER 7: "Synthesis of Colloidal Upconverting $NaYF_4$: Er^{3+}/Yb^{3+} and Tm^{3+}/Yb^{3+} Monodisperse Nanocrystals"

J. C. Boyer: experimental work and manuscript preparation

L. A. Cuccia: project collaborator

J. A. Capobianco: project supervisor

Chapter 1

General Introduction

1.1. PREAMBLE

In the past, when given the task of modifying a physical property of a particular material, a chemist would typically vary the structural or elemental composition of the material to achieve that change. In essence, the properties of crystalline solids were ordinarily categorized by their chemical constitution without reference to their size.[1] However, in the past two decades it has been widely demonstrated that the properties of select inorganic materials may be modified by changing either their size or shape on the nanometer level.[2] The variations in the physical properties are propagated by reducing the size of the crystals, not by varying their chemical composition.

The variations in nanocrystal properties with size have been attributed to two major effects when one enters the nanometer size range.[1] First, in nanocrystals, a significant fraction of the atoms are at or near the surface of the particles. In any nanocrystalline material, the surface atoms make a distinct contribution to material properties, thus surface effects can have a large influence on the nanocrystals' physical properties. Secondly, the intrinsic properties of the nanocrystals' interior are altered by quantum size effects.

Since the early 1980's, research in the field of nanocrystalline materials has grown markedly as exemplified by the increasing number of publications on the topic every year. A few isolated areas of research have now spawned a global 'nanoscience' initiative combining ideas and techniques from biology, chemistry, physics, materials science and engineering. Nanoscience is the attempt to synthesize and arrange materials on the sub-nanometer to 100 nm length scale. At the same time, researchers can utilize nanomaterials to understand the evolution of bulk properties from the molecular discovery phase.[3] Much of the early research on this topic was driven by investigations focused on semiconducting nanocrystals (quantum dots), where it was effectively demonstrated that reducing particle size below their Bohr radius produced a characteristic blue shift of the band gap absorption (and thus the nanoparticles color).[4]

This initial interest was not only confined to the realm of semiconducting phosphors. A little over a decade after the initial work on semiconducting nanocrystals, the first scientific articles on nanocrystalline insulating nanocrystals doped with lanthanide ions started to appear.[5-8] This innovative class of materials demonstrate striking particle-size-dependent phenomena that affect: emission lifetime;[9-11] luminescence quantum efficiency[12] and concentration quenching.[13-16] The optical properties and applications of lanthanide-doped nanocrystals stand amongst the most exciting research fields in chemistry, physics and biology.[17]

The development of several new synthetic and processing methods in the last two decades has made it possible to prepare lanthanide doped nanocrystalline insulators with nanometer dimensions. Some of the numerous methods for synthesizing insulating nanoparticles include vaporization/condensation of ceramics,[5-8] laser ablation,[18] laser-driven reactions,[19] flame and plasma processing,[20] solution-phase synthesis,[21-29] precipitation in emulsions and microemulsions,[30-35] sol-gel processing,[36-38] spray pyrolysis,[39] combustion synthesis,[40-45] and high-energy mechanical milling.[46] By preparing the host material in nanocrystalline form, one is capable of modifying its physical and surface properties thereby affecting the luminescence and dynamics of the lanthanide dopant ion.[6]

The luminescence efficiency of these lanthanide-doped nanocrystals is often limited by the dynamics (emission lifetime) of the lanthanide ion, which is dependant on its interactions with the insulating host as well as the medium surrounding the nanocrystal itself.[6, 7, 9, 11, 47] The motivation behind the study of lanthanide doped nanocrystals is the tremendous changes that are observed in the spectroscopic properties of well known luminescent materials that are brought on by reducing their dimensions into the nanometer size range. It is hoped that by synthesizing many common luminescent materials in nanocrystalline form we will unlock fascinating new optical properties. In addition, the ability to synthesize these materials as discrete nanocrystals also opens up new avenues for their use that could never have been dreamt of beforehand. Thus it is of the utmost importance to investigate and gain an understanding of these novel materials in an attempt to optimize their spectroscopic and physical properties for use in future technological applications.

1.2. THE LANTHANIDES

The fourteen elements that follow lanthanum in the periodic table ranging in atomic number from 57 to 71 are known as the lanthanoids.[48] They form a special group of chemically similar elements found at the bottom of the periodic table (see Figure 1.1) that have in common an open 4*f* shell. The history of the rare earths stems back to 1787 when Carl Axel Arrhenius found a black stone near Ytterby, Sweden. The mineral was named Ytterbite (later renamed gadolinte) after its place of discovery. From this mineral the first lanthanide, an impure form of yttrium oxide, was extracted in 1794 by Finnish chemist Johann Gadolin and termed Yttria (Yttrium). A second lanthanide named Ceria (Cerium) was discovered by Klaproth in 1803. It was later revealed that these two minerals were actually mixtures of several new elements. Over the next few decades, research on the mineral Ceria resulted in its separation into the lighter lanthanides: cerium (1803) lanthanum (1839), praseodymium (1885), neodymium (1885), samarium (1879), europium (1896), and gadolinium (1880).[49] Over the same period of time Yttria was separated into oxides of erbium (1843), terbium (1878), ytterbium (1878), holmium (1878), thulium (1879), dysprosium (1886), and lutetium (1907).[49] Overall it took nearly a century for all the lanthanides, excluding promethium, to be identified due to the fact that this group of elements has similar chemical properties. The missing element number 61, promethium, was only synthesized and characterized in 1947 due to its radioactive nature, completing the lanthanide series.[50]

It is often argued that lanthanum should not be considered a member of the lanthanide family as it lacks *f*-electrons. Nevertheless it is included in the lanthanide series as it possesses many similar chemical and physical properties to the other members of the group. The Group III transition metals Y and Sc are also frequently included in discussions about the lanthanides as they too have many similar properties to the lanthanide family of elements. In fact, scandium and yttrium are often found in the same minerals as other lanthanide ions as noted above.

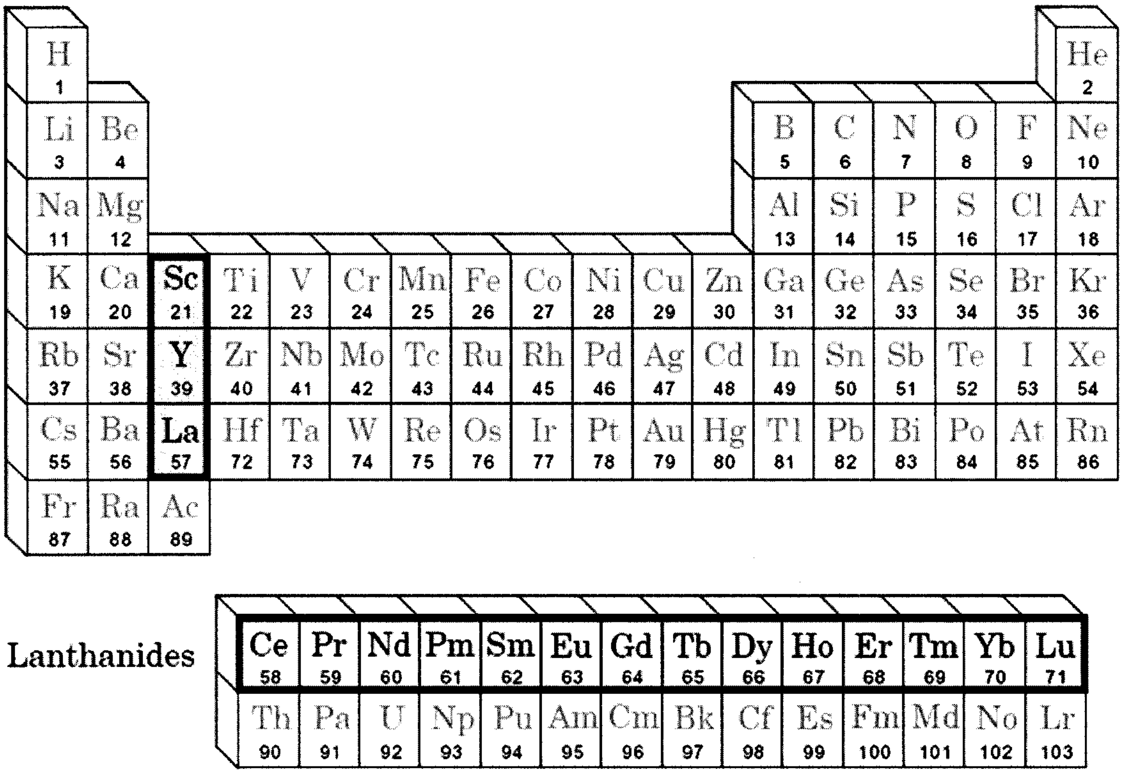

Figure 1.1. The periodic table of the elements with the lanthanides (yellow) and similar ions (blue) highlighted.

It should also be noted that the lanthanides are sometimes referred to as the 'rare-earths'. The term 'rare-earth' originates from the difficulty researchers had in isolating these elements early in their discovery. In fact, the rare earth elements are never found as pure metals in nature, but normal exist as the oxides. However, the name is somewhat of a misnomer as a fair number of the rare-earth elements are quite common.[51] For instance, Ce, the most abundant lanthanide in the Earth's crust, at 60 parts per million, is more abundant than copper.[52] Cerium is followed closely by yttrium at 33 parts per million, lanthanum at 30 parts per million, and neodymium at 29 parts per million.[52] Even the least abundant of the lanthanides, thulium and lutetium, at 0.5 parts per million are more abundant in the earth's crust than antimony, bismuth, cadmium, gold, silver, and thallium.[52]

The electron configuration of the lanthanides range from [Xe] $6s^2 5d^1$ for lanthanum (La) to [Xe] $6s^2 4f^{14} 5d^1$ for lutetium (Lu).[48] The ground-state and trivalent electronic configurations of the lanthanides are provided in Table 1.1. The lanthanide ions are chiefly trivalent and it is principally the properties of the trivalent ions which are important rather than those of the neutral atoms. The progression of the electron configuration is completely regular for Ln^{3+} ions (Ln is the generic symbol for any one of the lanthanides), from $4f^0$(La), $4f^1$(Ce) to $4f^{14}$(Lu). All trivalent ions have the xenon-like gas shell of 54 electrons in common and contain N $4f$ electrons, with N ranging from zero for La^{3+} to 14 for Lu^{3+}.

The $4f$ orbitals lie well inside the electronic shell and are well protected from external influences by the filled $5s$ and $5p$ orbitals. As a consequence of the poor shielding offered by the $4f$ electrons, there is a steady increase in effective nuclear charge and an associated reduction in size with increasing atomic number. Although the trend is observed from the atomic radii, it is best shown by the radii of the trivalent cations. A consequence of the lanthanide contraction is that holmium (Ho^{3+}) is the same size as the much lighter Y^{3+} with corresponding similar properties.

Table 1.1. Electron Configuration of Lanthanide Atoms and Ions

Atomic Number	**Name**	**Symbol**	**Electron Configuration**	
			Atom	**M^{3+}**
57	Lanthanum	La	[Xe] $6s^2 4f^0 5d^1$	[Xe]
58	Cerium	Ce	[Xe] $6s^2 4f^1 5d^1$	$4f^1$
59	Praseodymium	Pr	[Xe] $6s^2 4f^3$	$4f^2$
60	Neodymium	Nd	[Xe] $6s^2 4f^4$	$4f^3$
61	Promethium	Pm	[Xe] $6s^2 4f^5$	$4f^4$
62	Samarium	Sm	[Xe] $6s^2 4f^6$	$4f^5$
63	Europium	Eu	[Xe] $6s^2 4f^7$	$4f^6$
64	Gadolinium	Gd	[Xe] $6s^2 4f^7 5d^1$	$4f^7$
65	Terbium	Tb	[Xe] $6s^2 4f^9$	$4f^8$
66	Dysprosium	Dy	[Xe] $6s^2 4f^{10}$	$4f^9$
67	Holmium	Ho	[Xe] $6s^2 4f^{11}$	$4f^{10}$
68	Erbium	Er	[Xe] $6s^2 4f^{12}$	$4f^{11}$
69	Thulium	Tm	[Xe] $6s^2 4f^{13}$	$4f^{12}$
70	Ytterbium	Yb	[Xe] $6s^2 4f^{14}$	$4f^{13}$
71	Lutetium	Lu	[Xe] $6s^2 4f^{14} 5d^1$	$4f^{14}$

The majority of the optical properties of the lanthanide ions can also be attributed to the shielded nature of the $4f$ orbitals. Almost all of the spectroscopic research on the lanthanides ions has occurred exclusively in the past century. The origins of the characteristic sharp spectral lines of the lanthanide ions mystified scientists until the early 1900's. It was at this time that Bethe, Kramers, and Becquerel using an atomic model attributed the spectral lines to transitions with the $4f^n$ configuration of the lanthanide ions.[53-55] Problems still existed with this theory as the interconfigurational $4f \rightarrow 4f$ electric dipole transitions should be forbidden by selection rules and thus should be much weaker than what was observed. The explanation of this phenomenon had to wait until

1937 when Van Vleck and coworkers concluded that the $4f^n$ states had small contributions from opposite parity states ($4f^n - 5d$ or charge-transfer states) leading to a small change in the dipole moment during the transition.[56] The $5d$ states can mix with $4f$ states through odd-parity crystal-field components. Research on the optical properties of the lanthanide ions has advanced considerably since these early investigations. Currently lanthanide luminescence is very well understood and researchers can now calculate the energies of the $4f^n$ levels with great accuracy,[56-62] determine transition probabilities using Judd-Ofelt theory,[63, 64] and relate non-radiative relaxations rates to multiphonon relaxation.[65-67]

The first detailed experimental study of the lanthanide $4f \rightarrow 4f$ transitions in the range spanning from 0-40,000 cm^{-1} was undertaken by Dieke and coworker in the 1950's and 1960's.[62] The work resulted in the impressive tabulation of all the observable energy levels of the trivalent lanthanide ions in the $LaCl_3$ host lattice up to 250 nm. The energy level diagram that resulted from this work is called the Dieke diagram (see figure 1.1 below).[62] It is used by spectroscopists as a reference for the $4f^n$ energy levels of the trivalent lanthanide ions, irrespective of the host lattice, since their locations are relatively insensitive to changes in the surrounding environment.

The majority of the applications of the lanthanide elements revolve around the optical properties of the trivalent ions. The most common application of lanthanides is the generation of artificial light. Several lanthanide ions, such as Eu^{3+} and Tb^{3+}, when doped into solid state hosts find use as phosphors in fluorescent lights and cathode ray tubes (CRTs).[68] Several of the lanthanide ions are used as the active ion in laser crystals and glasses, the most common being the 1.06 μm laser line of neodymium in yttrium aluminum garnet.[48] The lanthanides can also be widely found in catalysts for the petroleum industry where they are utilized in the cracking of crude oil.[49] Several lanthanide complexes are also used in the biological sciences and medical field for assay and imaging purposes.[69] For instance, gadolinium complexes are used extensively in Magnetic Resonance Imaging (MRI) as contrasting agents due to the gadolinium ions large magnetic moment.[70]

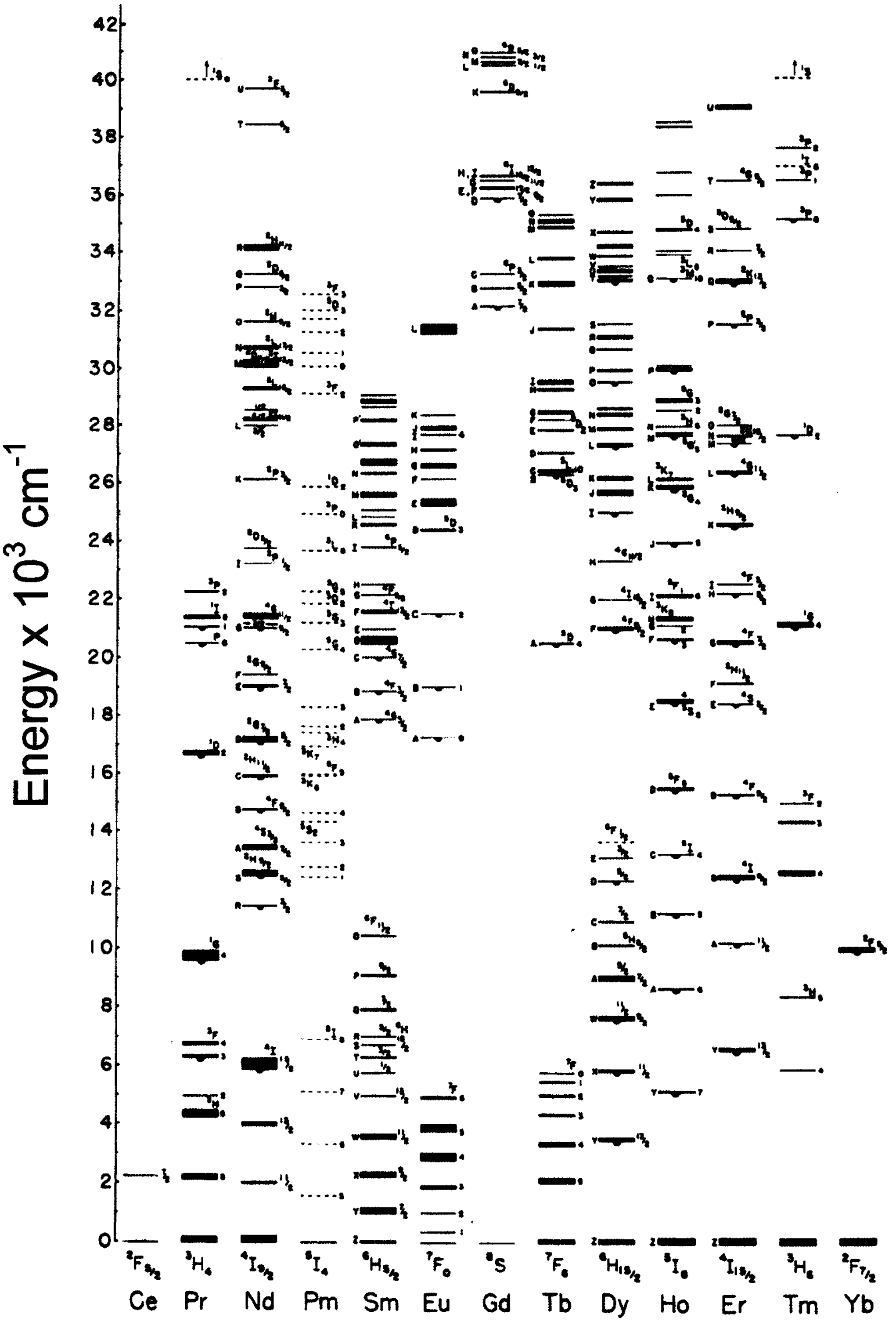

Figure 1.2. The Dieke diagram: an overview of the experimentally observed 4*f* levels of the trivalent lanthanide ions (Ln^{3+}) in LaCl$_3$.

1.3. UPCONVERSION

Upconversion is the generation of visible or UV light from lower energy radiation, usually NIR or IR, through the use of transition metal, lanthanide or actinide ions doped into a solid state host. What makes upconversion attractive is the possibility of generating luminescence at a shorter wavelength than that of the pump laser.[71] This is accomplished through the population of an excited state whose energy is greater than that of the pump laser via the absorption of two or more pump photons. In bulk glasses and crystals, upconversion can be utilized instead of frequency doubling crystals for the generation of visible and near ultraviolet energy from infrared or near-infrared lasers.[71]

Upconversion requires the absorption of two or more photons but, unlike multi-photon absorption observed in organic dyes and quantum dots, the photons are absorbed sequentially rather than simultaneously. A requirement for efficient upconversion is the presence of a metastable intermediate electronic state which can be populated with the exciting radiation and the presence of an efficient luminescent state in VIS and UV. It is this metastable intermediate state which acts as a population reservoir from which a second photon or energy transfer can populate the upper emitting state. These requirements for efficient upconversion make trivalent lanthanide solid-state materials ideal for this application. The transitions within the $4f^n$ levels of the lanthanide ions are significantly shielded from outside influences keeping their position relatively constant from one host lattice to the next and making them relatively insensitive to external influences such as solvent or ligands. As well, the sharp spectroscopic lines have high emission cross sections when doped into solid-state materials resulting in efficient luminescence. Many of the upconversion mechanisms observed in the lanthanide ions involve energy transfers between the ions. The crystal field splitting (Stark levels) observed in the lanthanide ions provide many intermediate levels from which these energy transfers may occur.

Several of the trivalent lanthanide ions (Pr^{3+}, Nd^{3+}, Ho^{3+}, Er^{3+} Tm^{3+}) meet these requirements and are particularly well suited for upconversion emission. These ions possess numerous intermediate metastable levels that can be populated by absorptions from common NIR lasers such as a tunable Ti:sapphire laser or relatively inexpensive semiconductor laser diodes. In addition, these ions have several long-lived upper excited states that give rise to strong visible emission. The upconversion efficiencies of some of these ions can be increased further by co-doping with Yb^{3+} due to its intense absorption cross-section around 980 nm and comparable energy difference with several of the above mentioned ions. Depending on the dopant ions and the exciting wavelength utilized, these trivalent lanthanide ions are capable of producing upconversion emissions over a range of wavelengths making the realization of numerous upconverting nanocrystalline phosphors with unique spectral characteristics a possibility.

There are three major types of mechanisms that have been observed to produce the upconversion process. The processes are illustrated below using hypothetical 3 level ions. Details of individual upconversion mechanism in specific lanthanide ions will be left for discussion in subsequent chapters since even the simplest mechanism may involve numerous multiphonon relaxations or energy-transfers. The introduction given below is fundamental and will deal with upconversion mechanisms in their simplest forms. For additional information the reader may choose several excellent reviews examining specific lanthanide doped systems[71-74] and the mathematics governing the upconversion processes.[75]

1.3.1. Excited State Absortion (ESA) Upconversion

The first case is sequential two-photon absorption or excited state absorption (ESA) upconversion, in which the upper excited state is populated by the sequential absorption of two photons. This mechanism was first postulated by Bloembergen in 1959 as a method for detecting and counting IR photons.[76] ESA upconversion is illustrated in Figure 1.3. The first photon populates a metastable state (energy Level 2) intermediate in energy between the ground state (Energy Level 1) and the upper fluorescing level (Energy Level 3). Pumping is initiated by absorption of a photon resonant with the wavelength of the 1 → 2 transition. The intermediate state (Energy Level 2) is metastable and can decay radiatively to the ground state. If a second photon arrives at the excited ion site before this metastable state decays to the ground state it can induce the transition to Energy Level 3. The radiative 3 → 1 transition produces the observed upconversion visible emission.

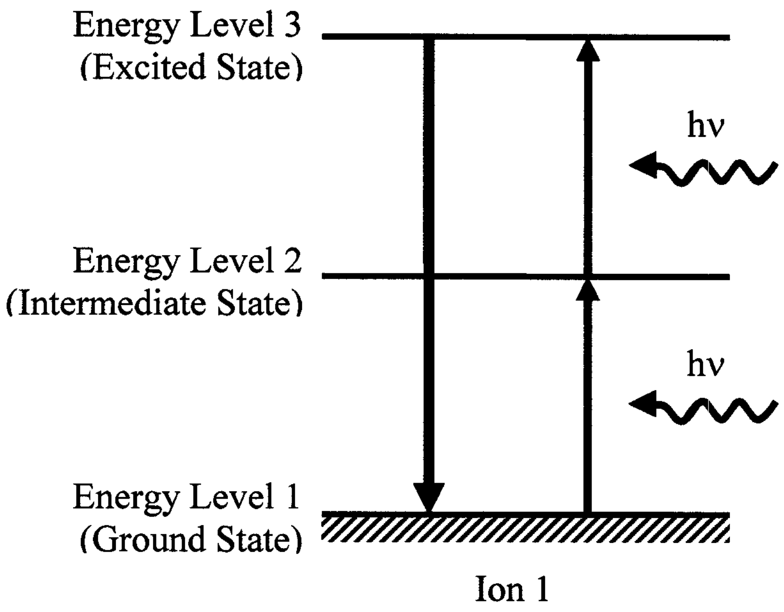

Figure 1.3. Schematic representation of an Excited State Absorption (ESA) upconversion mechanism in a simple three-level ion.

1.3.2. Energy Transfer Upconversion (ETU)

Upconversion luminescence involving energy transfer between ions was first observed by Auzel; who initially termed the processes APTE (*addition de photon par transfer d'energie*).[77] This mechanism was latter renamed Energy Transfer Upconversion (ETU).[75] Much of the early work on this type of upconversion mechanism was carried out on Er^{3+}/Yb^{3+} or Tm^{3+}/Yb^{3+} co-doped crystals in the 1960s. Figure 1.4 illustrates cooperative energy transfer upconversion in an ion pair. Pumping is initiated by the absorption of a photon by each of two dopant ions in close proximity. Effective cooperative upconversion requires that the donor-acceptor pair be located near one another and thus is highly dependent on the dopant concentration. In the case of cooperative upconversion, two ions in excited states interact as a donor-acceptor ion pair.

Pumping is initiated by the absorption of a photon by each of the ions labeled “Acceptor” and “Donor”. The photon corresponds to the 1 → 2 transition. As in sequential upconversion Energy Level 2 is metastable. Population in Energy Level 2 may decay by radiation to the ground state or may be removed by cooperative upconversion. In the latter case the donor ion transfers its energy to the acceptor ion. This process is indicated in the figure with dashed lines and results in the “Acceptor“ ion being promoted to Energy Level 3. The population in Energy Level 3 can subsequently radiate in the visible through the 3 → 1 transition. Effective cooperative upconversion requires that the donor-acceptor pair be located near one another.

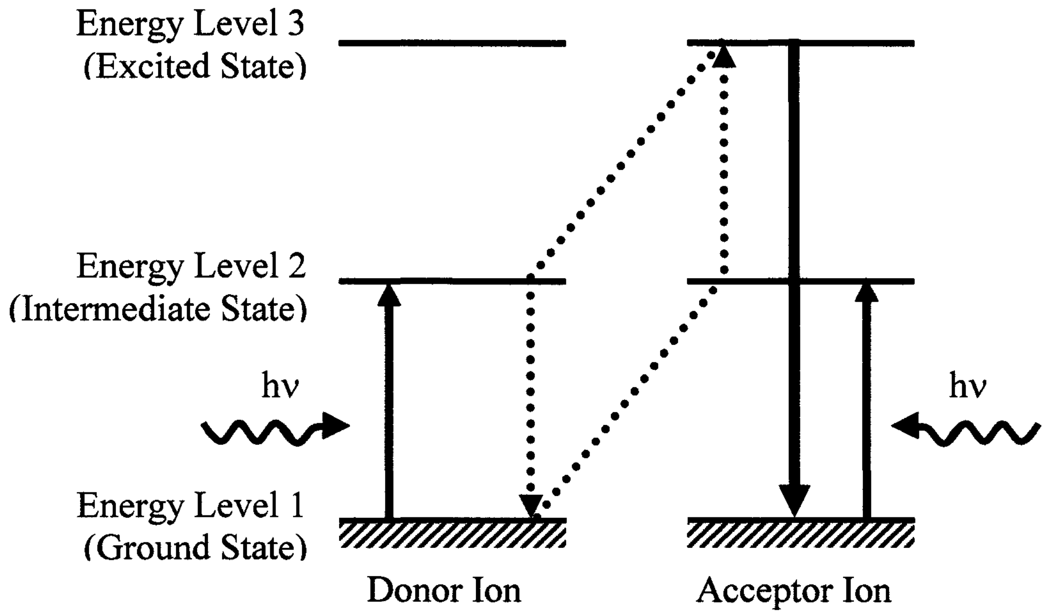

Figure 1.4. Schematic representation of an Energy Transfer Upconversion (ETU) mechanism in simple three-level ions.

1.3.3. Photon Avalanche Upconversion

The third case, photon avalanche upconversion involves energy transfer between an excited "donor" ion and a neighboring "acceptor" ion in the ground state.[78] Figure 1.5 shows a schematic representation of a donor-acceptor ion pair involved in the photon avalanche upconversion mechanism. In this mechanism the exciting radiation is resonant with the transition from Energy Level 2 to upper Energy Level 3' excited state. The donor ion is initially excited into the metastable intermediate state (Energy Level 2) through a non-resonant absorption. The donor ion then absorbs a subsequent photon via the Energy Level 2 → Energy Level 3' followed by a rapid relaxation that populated the upper emitting Energy Level 3. Emission from this level via the Energy Level 3 → Energy Level 1 radiative transition produces visible emission and constitutes one of the steps in the photon avalanche upconversion process. An alternative decay mechanism involves energy transfer from the donor ion in Energy Level 3 to a neighboring acceptor ion in the Energy Level 1 ground state. The result of this ion pair interaction is that the donor ion loses part of its energy to the acceptor, producing two ions in the Energy Level 2 metastable state. As the initial step in this mechanism involves a non-resonant absorption, it is characterized by a threshold power which must be achieved for efficient upconversion to occur. This threshold condition is a distinct feature of the photon avalanche mechanism and can be useful in determining experimentally whether it is responsible for an observed upconversion luminescence.

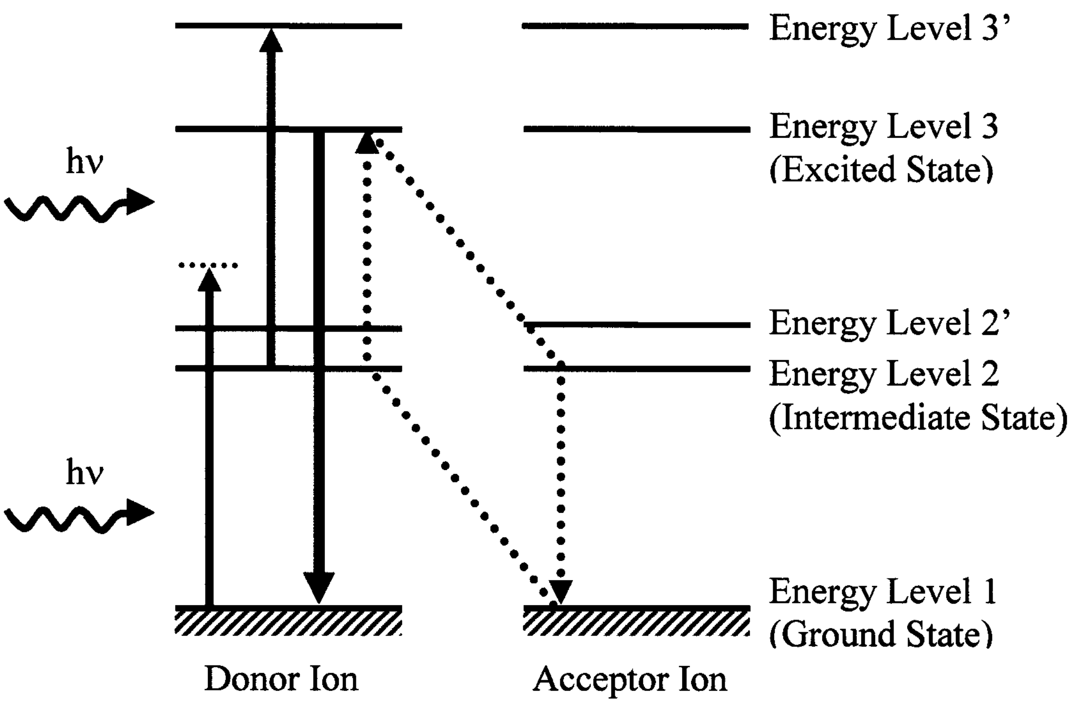

Figure 1.5. Schematic representation of an Photon avalanche upconversion in modified three-level ions.

1.4. LANTHANIDE DOPED UPCONVERTING NANOCRYSTALS

Recent discoveries in materials synthesis have given rise to an important new field of research, that of luminescent lanthanide-doped nanoparticles. The wide-ranging potential applications for these nanoparticles have sparked research aimed at both gaining a better understanding of the science behind their synthesis as well as their physical and spectroscopic characteristics. Recently, numerous comprehensive studies have been carried out to examine the effect that synthesizing lanthanide-doped materials in the nanoscale has on their optical properties.[7-9, 79-84]

Conventional micron-sized lanthanide-doped phosphors are utilized in a wide range of applications. These include phosphors for fluorescent lighting, display monitors and x-ray imaging; scintillators, lasers and amplifiers for fiber-optic communication.[6] Phosphors are high-purity inorganic materials that emit light when exposed to various excitation sources such as photons, electrons or an electric field.[68] The host crystal can itself emit radiation or contain controlled levels of impurity ions (activators) which stimulate or enhance luminescence. Typically, phosphors are composed of an inert host lattice and an optically excited activator, usually a 3*d* or 4*f* electron metal. The development of several new synthetic and processing methods has made it possible to prepare these materials with nanometer dimensions. The two methods examined in this thesis are the combustion synthesis technique and the thermolysis of trifluoroacetate precursors in the presence of a coordinating ligand.

The development of High Definition Television (HDTV) and Field Emission Displays (FED) in the early 1990's created a need for new phosphors with reduced particle sizes that were thermally stable, resistant to degradation, and had high luminous efficiencies.[45] The demands of these newer technologies produced a search for new materials and synthetic techniques to improve the performance of traditional phosphors. At the time, lanthanide-doped nanocrystalline materials exhibited considerable promise in delivering these sought-after qualities. Initial research on nanocrystalline Tb^{3+}-doped Y_2O_3 claimed an increase in luminescence efficiency over a traditional green emitting phosphor LaOBr: Tb^{3+}.[38] This result went against conventional theory that small phosphor size leads to a reduction in luminescence due to surface defects. Activators located on the surface, or on the grain boundaries, are thought to be non-luminescent or even luminescence quenching regions.[45] Thus the discovery of an efficient nano-scale phosphor greatly intrigued researchers world-wide as this result would have a significant impact on the display technology industry. Unfortunately, the claims reporting increased luminescence in lanthanide-doped nanocrystals turned out to be false. It is now widely accepted that the luminescence efficiencies of these nanocrystals will never match those of the corresponding bulk materials due to the numereous surface effects encountered in the nanomaterials.

While numerous studies have focused on the display applications of lanthanide-doped nanocrystals,[45, 85-87] examining the luminescence generated by exciting with UV light or electrons, very few have examined the upconversion phenomenon in these materials.[15, 80, 81, 88] Much of the interest in upconverting nanocrystalline materials is due to their prospective applications as fluorescent biological labels, security labeling, or as IR sensitive phosphors. The materials selected for the majority of this initial research were nanocrystalline oxides and garnets.[13, 80, 81] This was due in part to their superior physical properties and the availability of numerous methods to prepare these materials in the nanocrystalline form.[89-92] Furthermore, there is a wealth of literature on the spectroscopic and optical properties of lanthanide ions in single crystal and microcrystalline oxides and garnets to compare prospective results.[66, 93-99]

Preparation of nanocrystalline luminescent materials doped with rare earth ions by conventional ceramic methods are cumbersome; involving high-temperature solid-state reactions with sequential grinding and firing steps. However, advances in materials research resulted in the development of a combustion synthesis technique capable of producing large quantities of nanocrystalline material under relative mild conditions without the need for any sophisticated equipment.[40, 42] Luminescent materials powders synthesized by means of this method are generally more homogeneous, have fewer impurities and have higher surface areas than powders prepared by conventional solid-state methods.[6]

In this method metal nitrates (oxidizer) react with an organic fuel such as glycine. The reactants are mixed in an aqueous precursor solution and the reaction is initiated by evaporating the water in a muffle furnace at temperatures of 500°C or less. Alternatively, the reaction can be initiated by heating the resulting solution with a Bunsen burner (*cf.* Figure 1.6.) until combustion occurs. The mechanism of the combustion reaction is quite complex. The parameters that influence the reaction include: type of fuel, fuel to oxidizer ratio, use of excess oxidizer, ignition temperature, and water content of the precursor mixture.[42, 43, 100] A desirable fuel should react non-violently, produce non-toxic gases, and act as a complexing agent for metal cations. Complexes increase the solubility of metal cations, thereby preventing crystallization as the water in the precursor solution evaporates. The rapidity of the reaction results in particles with nanoscale diameters, which can be controlled by adjusting the fuel-to-oxidizer ratio. When complete combustion occurs, the only gaseous products obtained are N_2, CO_2 and H_2O, thus making this an environmentally clean processing technique. The evolution of these gasses is advantageous as they disintegrate agglomerates and more heat is carried from the system thereby hindering particle growth.[42, 43, 100]

Much of the early work on upconverting lanthanide-doped nanocrystalline powders focused on oxide and garnet materials synthesized via this method.[13, 15, 40, 42, 43, 100] If was found that the upconversion efficiencies of the materials could be maximized by optimizing several reaction conditions such as the type of fuel utilized, fuel-to-oxidizer ratio, furnace temperature and the amount of water remaining in the precursor solution at the ignition temperature. Annealing the prepared powders was also shown to improve brightness by eliminating any residual nitrate or carbon from the reaction itself.

All of these early studies on upconverting nanomaterials examined the upconversion luminescence of the dried powdered materials. However, for many of the potential applications of these materials it is required that the nanocrystals be dispersed as a clear transparent solution and the upconversion luminescence generated in this fluid state. By dispersing the nanocrystals as colloidal solutions one can also get a good indication of the degree of agglomeration in the nanopowder in question. For the upconversion phenomenon to be observed in solution the nanocrystals must be highly crystalline and possess a narrow particle size distribution. As well, the surface of the nanoparticles should be properly modified to ensure colloidal solubility.

To achieve high quality nanoparticles that meet these requirements, various solution-phase synthesis routes have been adopted to reduce the reaction temperature and avoid anealling of the particles.[26, 27, 82, 101, 102] Solution-phase synthetic processes are attractive means of synthesizing nanocrystalline materials since they offer a higher level of control over the particle size, crystallinity and microstructure than alternate techniques. The control is important from an application standpoint as the performance of material largely depends on these properties. These solution phase methods allow for preparing nanocrystalline fluorescent materials at a low temperature (<300°C) while at the same time allowing for a high degree of homogeneity of the particles, improved fluorescence properties and better processability than combustion synthesized powders.

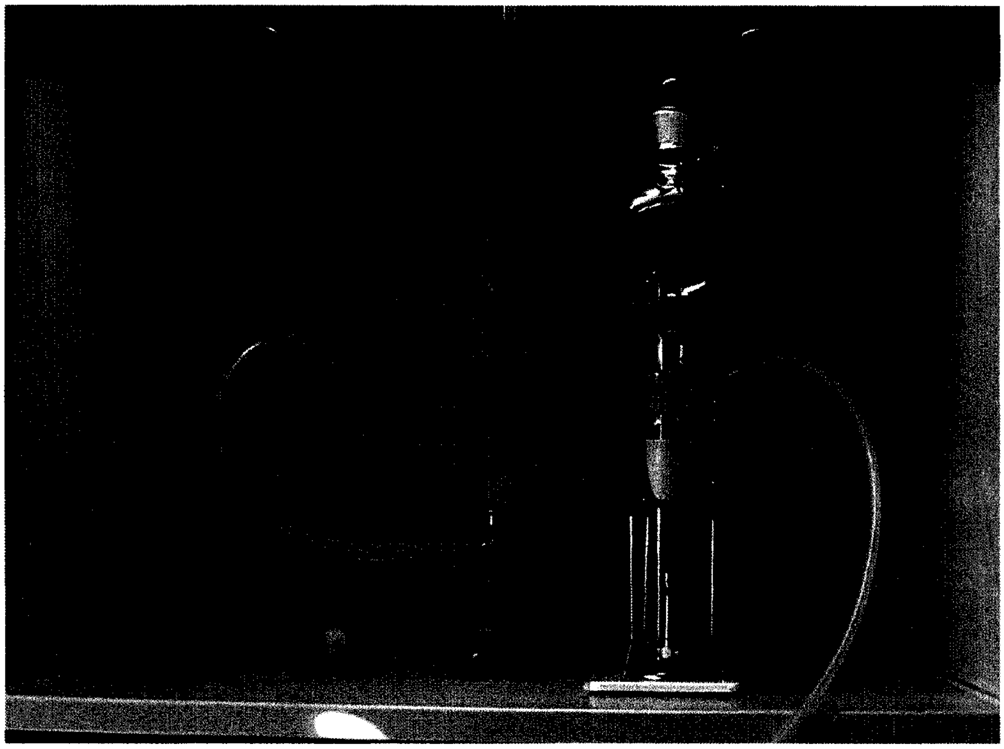

Figure 1.6. Reactor for the combustion synthesis of nanocrystalline Y_2O_3 and $Gd_3Ga_5O_{12}$.

The first report of upconversion in the nanocrystals dispersed in the liquid state focused on the upconversion luminescence of $YbPO_4$: 5% Er^{3+} and $LuPO_4$: 1% Tm^{3+}, 49% Yb^{3+} nanoparticles synthesized via a well known chemical precipitation route in a nonaqueous environment.[26] Blue, green and red upconversion was observed from the particles while colloidally dispersed in chloroform under excitation at 978 nm. Though this was a huge step in the development of upconverting nanoparticles the luminescence from these colloidal solutions was very poor when compared to traditional solid state upconverting phosphors.

Shortly after the feasibility of inducing upconversion in solution was demonstrated, numereous other studies appeared on upconverting nanoparticles capable of colloidal dispersion.[27-29, 82, 103] Almost all of these researchers choose to focus on the well known upconverting material Tm^{3+}/Yb^{3+} or Er^{3+}/Yb^{3+} doped $NaYF_4$ due to its high upconversion efficiency when synthesized as the bulk material.[104, 105] These materials were synthesized using the precipitation method described above or a high pressure method[103, 106, 107] where the necessary reagents were combined in solution and placed in a high pressure reactor for a set period of time.

Though these synthetized nanoparticles are capable of upconversion while dispersed in solution, there are disadvantages in both methods. The precipitation synthesis requires the preparation of a cationic educt-solution containing the lanthanide ions, as well as a fluoride educt-solution that are then combined and heated to obtain the nanoparticles. The technique requires several steps as well as sodium metal. In the high pressure reactions, appropriate sodium, lanthanide, and fluorine sources are mixed in an aqueous solution and placed in a high pressure reactor for up to 24 hours at temperatures ranging from 100 to 200 °C. This technique required fewer steps than the precipitation reaction but long wait times as well as high pressures and specialized equipment are required.

For the synthesis of colloial $NaYF_4$: Er^{3+}, Yb^{3+} and Tm^{3+}, Yb^{3+} nanoparticles we chose to focus on the co-thermolysis of sodium trifluoroacetate and rare eath trifluoroacetate in a mixture of coordinating and non-coordinating solvents. A similar approach was also used in the literature to produce sodium rare-earth fluoride nanocrystals and LaF_3 nanoplates.[101, 102] This technique is based on the well known fact that metal trifluoroacetates thermal decompose to produce the corresponding metal fluorides at relatively low temperatures (200-300 °C).[108-111] In these methods the noncordinating solvent octadecene was used as the primary solvent due to its high boiling point (315 °C). Oleic acid was chosen as the coordinating ligand due to its successful use in the synthesis of an assortment of nanocrystals.[112, 113] This technique is advantageous as it utilizies simple laboratory equipment (hot plates and heating mantles), has a short reaction time (one or two hours) and requires only a single round-bottom flask. A schematic representation of the reaction is given below (Figure 1.7.) along with a photo of the experimental setup.

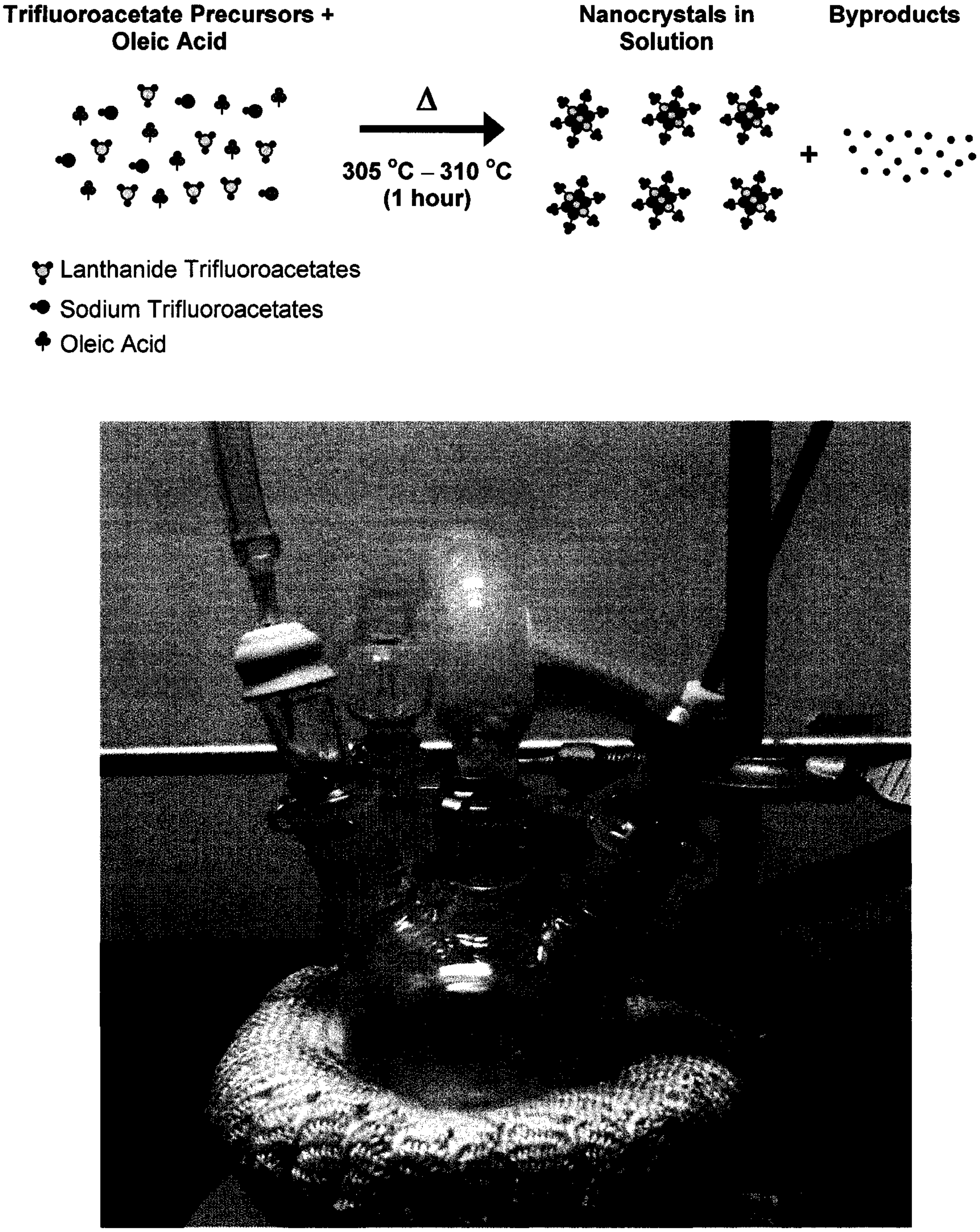

Figure 1.7. Schematic representation of the thermolysis reaction and photo of the experimental setup.

1.5. UPCONVERTING NANOCRYSTALS AS BIOLABELS

The realization of efficient upconverting nanocrystals has resulted in growing interest in their use for bioimaging and in biological assays.[33, 34, 106, 107, 114-117] Compared to other fluorescent media currently utilized in these tasks, such as organic dyes and semiconductor quantum dots, insulating nanocrystals are particular robust and resistant to chemical and photoinduced degradation. Photobleaching has not been observed to occur in upconversion nanocrystals at the power densities that are used for excitation (200 W/cm^2). The additional problem of intermittence in emission known as blinking, which is encountered in quantum dots, does not occur in lanthanide doped nanocrystals as they contain multiple luminescing ions per particle.

Upconverting phosphors have a number of properties that are advantageous for use in the *in vitro* imaging and detection of biological compounds.[33, 34, 114, 116, 117] The only substances capable of producing visible light from the NIR radiation under the excitation conditions used in these techniques (980 nm light) would be the upconverting nanoparticles themselves. Thus any background fluorescence from the carrier fluid, assay biochemistry, or sample itself should be eliminated when using upconverting nanoparticles as labels. The only remaining sources of background signal would be stray light and detector noise (e.g. dark current) which can be minimized through careful detector selection and experimental setup. Additionally, colloidal suspensions of nanoparticles remain in solution for extended periods of time and do not sediment out during assays.

An additional benefit of using inorganic nanocrystals is the relatively insensitive of their optical properties to the surrounding environment (for example, buffer chemistry and assay temperature) when compared to organic dyes, since the upconversion process occurs solely within the nanocrystal. As a consequence the detection process is unaffected by the fluid composition and temperature range of the assay.

Additionally, the upconverting nanoparticles are capable of being excited using relatively inexpensive 980 nm infrared laser diodes. These laser diodes are compact in size yet are capable of producing the excitation densities required to excite the nanophoshors. The use of upconverting fluorophores also simplifies the detection process. The emission wavelengths of the nanocrystals (400-700 nm) are considerably removed from the 980 nm excitation wavelength; consequently no complitcated detection equipment or time-resolved detection technique is required to improve sensitivity.

A number of different phosphor colors can also be obtained by varying the luminescencing ion or dopant concentrations. Each spectrally unique upconverting nanophosphor can then be attached to a different detection probe (for example, antibody or nucleic acid oligomer) to allow for multiplexing assays. Moreover, the upconversion emission bands of lanthanide ions are narrow when compared to those of other fluorescent media, allowing for easy detection and quantization of the distinctive optical signature of each nanophosphor.

There has been a growing development of an innovative class of detection labels by coupling upconverting phosphors to biological compounds.[33, 34] In these commericial labels, the 100-400 nm upconverting phosphors are detected through their upconversion emission and can be functionilzed by attaching biological compounds that recognize specific analytes, such as protein, DNA, or viruses. Once functionalized these nanoparticles would be biocompatible and can be utilized in immunoassays and DNA assays, such as the sandwich type immunoassay illustrated below (Figure 1.8.).

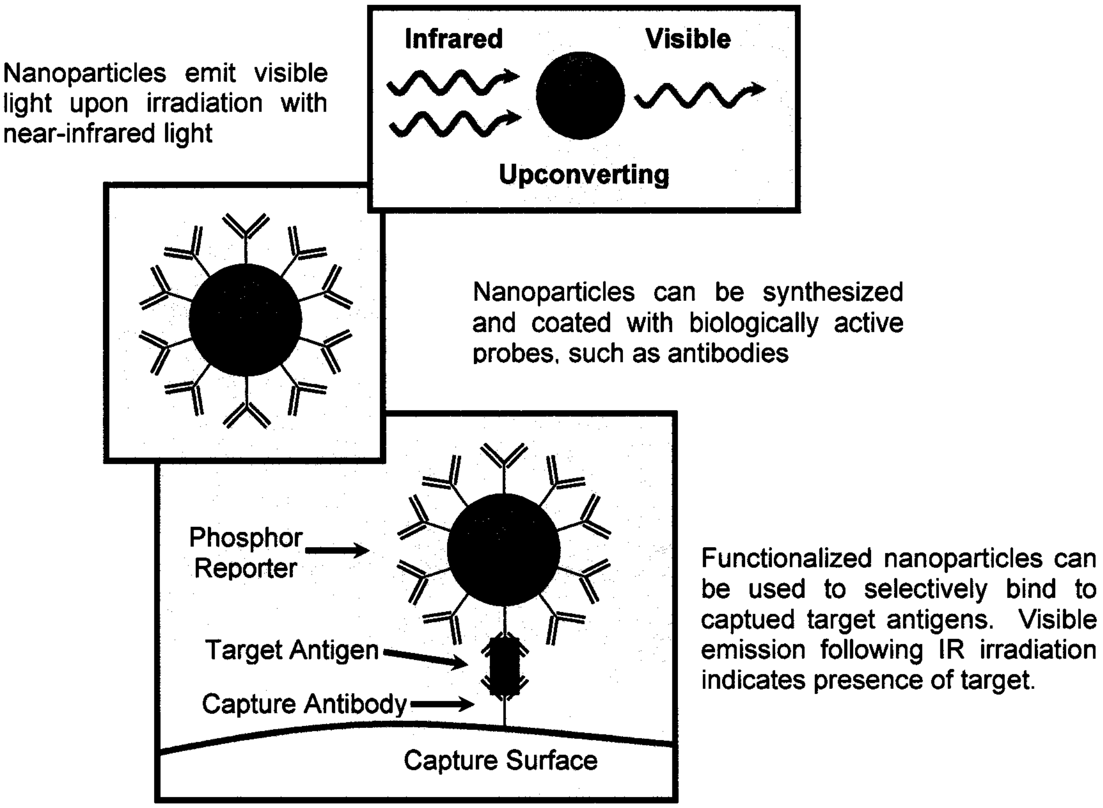

Figure 1.8. Illustration of a sandwich type assay utilizing an upconverting label.

The synthesis of upconverting nanocrystals with sizes below 30 nm allows for the possibility of designing new Fluorescence Resonance Energy Transfer (FRET) biological assays based on upconversion phenomenon.[101, 106, 114, 118] Currently biological assays which detect binding interactions rely heavily on FRET. Though this has proven to be a powerful and useful technique, there are still several drawbacks that limit its sensitivity. Most FRET assays that are designed to detect binding interactions are based around non-radiative energy transfer between a 'donor' fluorophore and an 'acceptor' species that occurs when the two species are brought in close proximity. FRET is a short range interaction and can only occur over a distance of a few nanometers.

In a FRET assay, binding interactions are detected in one of two ways: (i) quenching of the donor fluorophore emission or (ii) the increased in emission from the acceptor species due to sensitization via energy transfer from the donor.[101, 118] A typical FRET assay is illustrated in Figure 1.9. There are several limitations to these assays as it currently stands. First, if one is relying on donor quenching to detect binding one can experience interference from other colored species in the sample. Furthermore, there can be non-specific quenching of the donor from species in the sample itself. As for assays

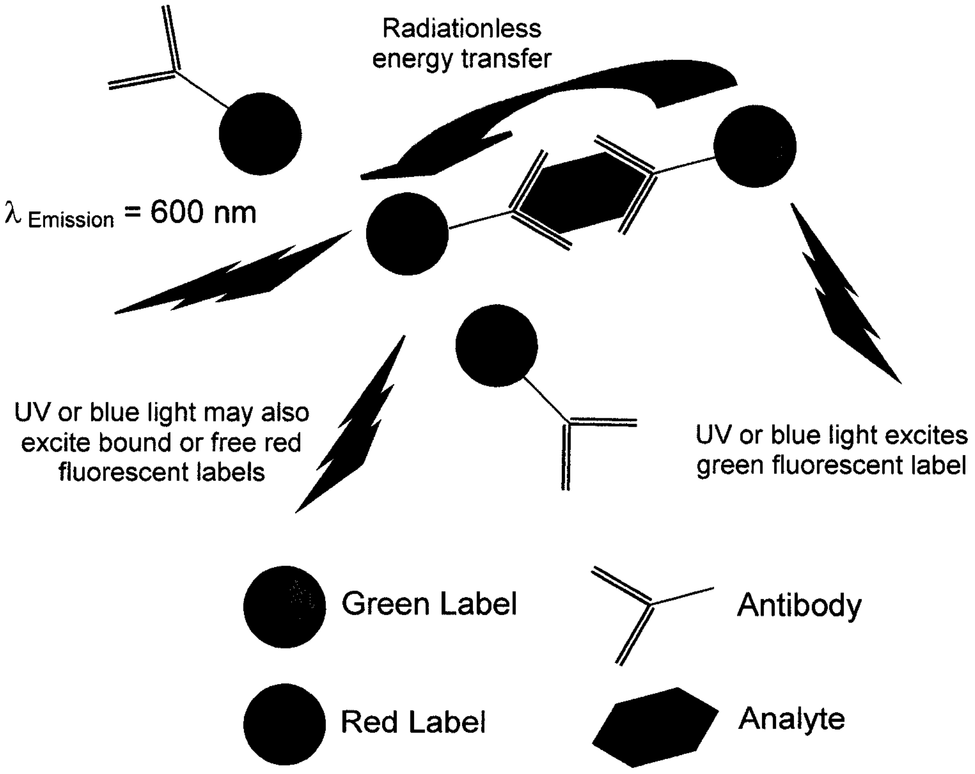

Figure 1.9. Diagram representing a conventional FRET assay.

based on sensitizied fluorescence, there are numerous problems that affect sensitivity. Ideally, the exciting radiation should not induce any luminescence from the acceptor directly. At present, this is almost impossible as current assay technologies utilize either UV or blue light to excite the donor species. Thus direct emissions must be taken into account when measuring the sensitized emission from the acceptor fluorophore. Emission from the donor may also occur in the same region as that of the acceptor as well as emissions from other impurities. In many cases a strong autofluorescence from the sample may be observed due to the fact that many assays are "mix-and-measure' with no washing steps to remove impurities. All of these factors contribute to effectively reducing the sensitivity of these assays.

The use of upconverting nanoparticles essentially eliminates all of the above mentioned drawbacks to a traditional FRET based assay. A schematic representation of a upconverting FRET assay is illustrate in Figure 1.10. As the excitation is in the NIR region of the spectrum it cannot excite the acceptor species directly, neither will it induce any autofluorescence from the sample itself. The narrow emission band of the lanthanide luminescence is also easily distinguished from that of the broad emission of the acceptor species. As mentioned previously, upconverting labels in the size range of 400-100 nm have already been realized. FRET assay labels must be less than 30 nm in size for efficient energy transfer to occur between the donor and acceptor species since only lanthanide ions near the surface can contribute. Many of the other nanocrystalline materials studied in the past were found to be considerably less efficient than their corresponding bulk materials due to deactivation of the lanthanide ions attributed to surface effects. Thus a material with high efficiencies must be chosen. As well surface treatments or coatings should be added to the particles to minimize these unfavorable surface effects. It is important to note that any additional material added to the particle surface will act as a spacer between the donor and acceptor species reducing the efficiency of the energy transfer.

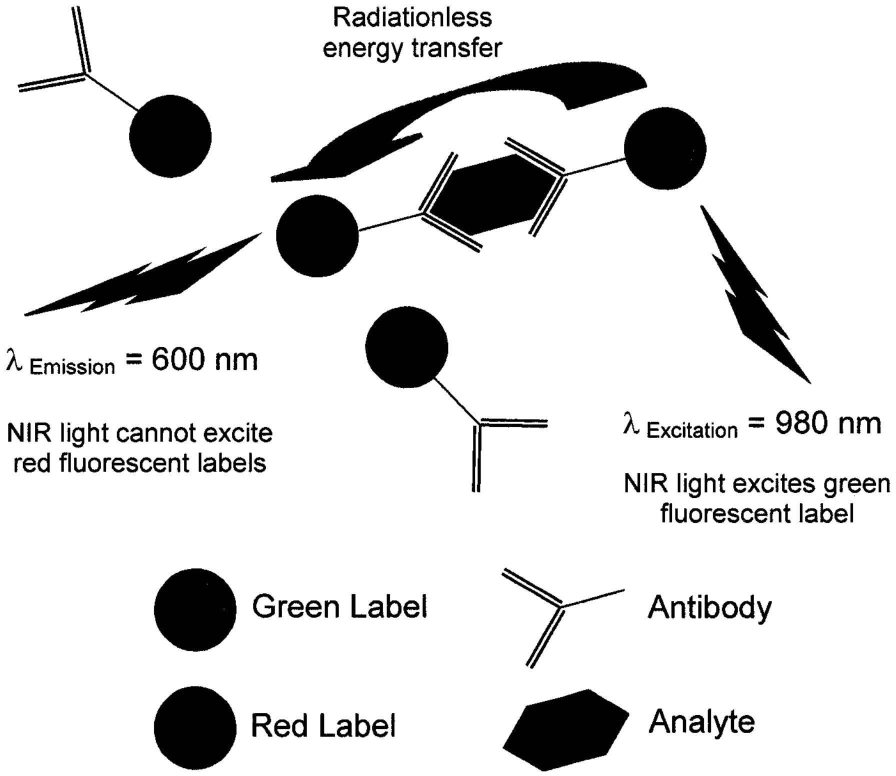

Figure 1.10. Diagram representing a FRET assay using upconverting technology.

1.6. STATEMENT OF THE PROBLEM

The large volume of work performed on semiconducting nanocrystals has not only resulted in numerous synthetic methods to obtain these materials but also to a comprehensive theoretical picture of their physical and optical properties. In comparison, relatively little work has been directed towards lanthanide-doped nanocrystalline materials. Theories on localized emissive ions in bulk crystals and glasses have been shown to be inadequate to describe the optical properties of lanthanide luminescence in nanocrystals. Thus characterization of various lanthanide-doped nanocrystals, and relating their optical properties to their physical characteristics, is imperative to gain a better understanding of these materials.

Overall, preparation of lanthanide-doped nanocrystals gives one the ability to examine materials that display distinctive optical properties. For instance, very little work has addressed dopant distribution and surface effects in these materials. The large surface-to-volume ratio for nanocrystals is expected to affect the dopant distribution between the interior and surface of the particles as well as increasing the amount of surface effects on the lanthanide ions. Lanthanide-doped nanocrystals are ideal to study surfaces effects since the high surface-to-volume ratio of nanocrystalline particles results in a significant fraction of all atoms being at or near the surface. By doping the nanocrystals with lanthanide ions, a probe is placed at the particles surface, which will be sensitive to changes in surface crystallinity and contaminants. The presence of surface defects and contaminants is a major factor affecting the efficiency of lanthanide-doped nanocrystals. Insight into the distribution of dopant ions and surface effects in lanthanide-doped nanocrystals is essential to designing new synthetic methods for the next generation of nanocrystalline materials.

This thesis will illustrate our initial research on upconverting lanthanide-doped nanocrystals as well as new methods for their production. In particular, we will examine how preparing well known luminescent materials, such as lanthanide-doped sesquioxides and garnets, in the nanometer size range affects their spectroscopic and upconversion properties. We investigate changes in the spectra, concentration quenching, luminescence decay times and upconversion mechanisms in these nanomaterials. With the achievement of these goals, an understanding of the physical processes which occur in nanocrystalline materials will be obtained allowing us to design the next generation of upconverting nanocrystals.

The knowledge acquired from these initial studies will be used in designing a new synthetic procedure to obtain discrete and dispersible upconverting nanoparticles. The search for new synthetic procedures is motivated by the fact that these materials have potential to make a significant impact in the areas of three-dimensional displays, display devices, security labeling and biolabelling. Before many of these technologies can be realized it is necessary to synthesize nanoparticles which can be transparently dispersed in solution. Thus, a novel method will be presented for the synthesis of inorganic upconverting nanoparticle phosphors, which emit visible light upon excitation with NIR radiation and are capable of being dispersed as clear colloidal solutions.

1.7. OUTLINE

This section outlines the format of this manuscript-based Thesis.

Chapter 1

This chapter provides a general introduction to upconverting lanthanide-doped nanoparticles and any necessary background information required to read this thesis. A short introduction to the lanthanide ions and upconversion in general is presented as well as a brief review of the work performed to date in the literature on upconverting nanocrystals. The potential advantages of using upconverting nanoparticles as biolabels and in biological assays are also presented.

Chapter 2

This chapter presents a comparison of the spectroscopic and upconversion properties between nanocrystalline and micron-sized Ho^{3+} doped Y_2O_3. The effect of adsorbed carbon dioxide and/or water on the surface of the nanocrystals was investigated by examining the differences in the luminescence, upconversion and decays of the excited states between the two materials. The drastic effect of the adsorbed species on the luminescent properties of the nanomaterials is most evident in their upconversion luminescence which was found to be severely reduced, or nonexistent, in the nanocrystalline sample when compared to samples with micron particle sizes. This work clearly demonstrated that Ho^{3+} luminescence and upconversion is significantly different in oxide nanopowders produced by the combustion synthesis method than in bulk materials.

Chapter 3

Following the discovery of the inherent problem in nanocrystalline Y_2O_3 towards lanthanide upconversion, other nanocrystalline oxide materials were investigate as potential hosts. Initial research on lanthanide doped Lu_2O_3 nanocrystalline samples indicated that this host might allow for higher upconversion efficiencies than Y_2O_3. Using the relatively simple structure of the Eu^{3+} spectrum as a probe for ion-host interactions, a detailed examination was performed on Eu^{3+} doped nanocrystalline and bulk Lu_2O_3 materials to determine what effect the nanocrystalline host has on the spectroscopy of the lanthanide ions. By examining the spectroscopy, fluorescence lifetimes and Judd-Ofelt parameters of a 1 mol % Eu^{3+}-doped cubic Lu_2O_3 nanocrystalline sample prepared by a combustion synthesis route we were able to deduce that the structural environment surrounding the dopant Eu^{3+} ion is distorted when compared to a sample with a micron particle size. The change in the Eu^{3+} environment was also reflected in the lifetimes of the $^5D_0$ excited state which were found to be severely lengthened in the nanocrystalline sample. This behavior indicates that the effective refractive index of the nanocrystals is considerably different from that of the bulk material thus modifying the oscillator strength of the $4f \leftrightarrow 4f$ transitions. The results of this study are presented in Chapter 3.

Chapter 4

After examining in detail the upconversion properties of several lanthanides in oxide-based nanocrystals, it was determined that a host with better physical characteristics was still required. Gadolinium Gallium Garnet ($Gd_3Ga_5O_{12}$) was known to exhibit a decreased tendency towards adsorbed CO_3^{2-} and OH^- ions when compared to the previously investigated lanthanide-doped oxide materials. It was hoped that this reduction in surface contaminants would result in a significant increase in upconversion efficiency. Thus, the main objective of Chapter 4 was the investigation of the luminescent and upconversion properties of 1% Ho^{3+} doped $Gd_3Ga_5O_{12}$ (GGG) nanocrystals. The upconversion properties were examined under two different excitation conditions: 647 nm excitation into the $^5F_5$ level and 756 nm excitation into the $^5I_4$ level. Temporal evolution studies were also undertaken to determine the intermediate state from which the upconversion takes place.

Chapter 5

To increase the upconversion efficiency of the Ho^{3+} doped nanocrystalline $Gd_3Ga_5O_{12}$ to a greater extent, a new sample was synthesized co-doped with 1% ytterbium (Yb^{3+}) as a sensitizer. The low absorption cross-sections of most lanthanide ions in the NIR region results in lower upconversion efficiencies in upconversion systems based solely on one lanthanide ion. Co-doping with Yb^{3+} overcomes this problem as it has the highest absorption cross section of any of the lanthanide ions in the NIR region. Yb^{3+} is also capable of transferring the excitation energy to the Ho^{3+} ion thus acting as an effective channel through which the upconversion processes can occur. Chapter 5 discusses the results of this study.

The effect of co-doping with Yb^{3+} was examined by investigating the upconversion properties of the nanocrystalline $Gd_3Ga_5O_{12}$: 1% Ho^{3+}, 1% Yb^{3+} sample under 978 nm excitation. The power dependencies and lifetimes of all observed emissions were determined to aid in the elucidation of the upconversion mechanisms. Careful comparison of the Stokes and anti-Stokes spectra revealed an enhancement of the red luminescence under 978 nm excitation leading to the conclusion that two distinct Energy Transfer Upconversion (ETU) mechanisms were active that preferentially populate the ($^5F_4$, $^5S_2$) and $^5F_5$ levels.

Chapter 6

Though nanocrystalline $Gd_3Ga_5O_{12}$: Ho^{3+}, Yb^{3+} proved to be an efficient upconverter, it has one drawback limiting its usefulness for biolabeling purposes. This material cannot be dispersed as a clear colloidal solution due to agglomeration of the individual nanocrystals. To rectify this problem, new synthetic procedures were sought to synthesis well-known upconverting materials as discrete, dispersible nanoparticles. The material with the highest measured upconversion efficiency in bulk materials is hexagonal $NaYF_4$ doped with the Er^{3+}/Yb^{3+} or Tm^{3+}/Yb^{3+} ion couples. Thus a new procedure was sought to allow for the synthesis of upconverting $NaYF_4$ nanocrystals doped with these two ion couples that could be dispersed as clear colloidal solutions.

Thus, Chapter 6 details the initial efforts in synthesizing and characterizing colloidal upconverting $NaYF_4$ nanoparticles. Taking advantage of the fact that lanthanide trifluoroacetates thermally decompose at relatively low temperatures, upconverting lanthanide-doped nanoparticles were synthesize in a heated mixture of oleic acid and octadecene. The use of lanthanide and sodium trifluoroacetates eliminates the use of hazardous chemicals such as sodium metal and/or hydrofluoric acid. The procedure is relatively simple and requires no complicated equipment or techniques compared to other methods presented in the literature that utilize high pressure reaction vessels.

The use of oleic acid as the surface ligand keeps the nanoparticles well separated during the synthesis thus reducing agglomeration and allows for their dispersal in a variety of nonpolar organic solvents. The synthesized nanoparticles were characterized in terms of their physical characteristics and upconversion properties. Physical characterization entailed X-ray diffraction to determine the crystalline phase and crystallite size; transmission electron microscopy (TEM) to examine sample morphology and individual particle size and ^{1}H NMR to detect the presence of surface species. The upconversion properties of the colloidal nanoparticle solutions were also investigated under 977 nm excitation.

Chapter 7

Though the colloidal solutions of the synthesized nanoparticles as described in Chapter 6 were capable of upconversion, the nanoparticles themselves were irregularly shaped and suffered from a broad particle size range. Thus further refinement of the synthesis was still needed to obtain nanoparticles with a defined shape and a narrower particles size distribution. The work presented in Chapter 7 details the modifications made to the previously discussed synthetic method resulting in upconverting nanoparticles with uniform size and shape. By introducing the lanthanide precursors slowly into the high temperature reaction mixture through a stainless-steel canula the nucleation and growth of the nanoparticles was slowed resulting in nanoparticles with a regular truncated-octahedral shape and a monodisperse particle size of ~28 nm. The resulting nanoparticles were thoroughly characterized through the use of transmission electron microscopy (TEM), selected area electron diffraction (SAED), ^{1}H NMR, powder X-ray diffraction (XRD) and high resolution luminescence spectroscopy. The $NaYF_4$ nanoparticles are capable of being of dispersed in nonpolar organic solvents thus forming colloidally stable solutions. The upconversion properties of the dispersed Er^{3+}, Yb^{3+} and

Tm^{3+}, Yb^{3+} doped nanoparticles were also investigated under 980 nm laser diode excitation and found to exhibit green/red and blue upconversion luminescence, respectively, with low power densities.

Chapter 8

Brief conclusions of the work presented in this Thesis are given as well as some suggestions for future work.

At the end of each section, linking text will be provided summarizing the key points required for proceeding onto the next chapters.

Chapter 2

Optical Spectroscopy and Upconversion Studies of Ho^{3+} Doped Bulk and Nanocrystalline Y_2O_3

Published as:

J. A. Capobianco, J. C. Boyer, F. Vetrone, A. Speghini and M. Bettinelli

Chemistry of Materials **2002**, *14*, 2915-2921.

2.1. ABSTRACT

In this paper we report on the optical spectroscopy and upconversion studies of Ho^{3+} doped nanocrystalline and bulk Y_2O_3, as a function of holmium concentration (0.1, 0.5, 1, 2, 5 and 10 mol%). Emission from the blue, green, red and NIR portions of the spectrum are recorded after 457.9 nm excitation. Red (646 nm) pumping results in blue and green emission through a two-photon excited-state absorption (ESA) upconversion process. NIR (754 nm) pumping results in blue, green and red emission. Overall luminescence of the nanocrystalline samples under one-photon excitation or 646 nm pumping is severely reduced when compared to that of the bulk sample, or non-existent in the case of the 754 nm pumping, which is attributed to absorbed atmospheric carbon dioxide and/or water on the surface of the nanocrystals. A quenching of the green ($^5F_4$, $^5S_2$) $\rightarrow$ $^5I_8$ emission is noted with increasing Ho^{3+} concentration that is attributed to a cross-relaxation mechanism involving two holmium ions.

2.2. INTRODUCTION

Recent advances in flat-panel display technology have ignited the search for new powdered phosphors with nanometer dimensions. Currently, phosphors in the micrometer size range find applications in a wide variety of information display devices such as cathode-ray tubes (CRTs), field emission displays (FEDs), vacuum fluorescent displays (VFDs) and electroluminescent (EL) devices.[45] It is anticipated that the advent of nano-sized phosphors will lead not only to improved resolution but also to an increase in luminescent efficiency. A class of materials that has shown considerable promise in delivering these qualities are doped nanocrystalline materials.

Since the early 1990's research in the field of nanocrystalline materials has grown markedly with more articles being published on the topic every year. Nanocrystalline materials are usually defined as polycrystalline solids with particle diameters or grain sizes ranging from sub-nanometers up to 100nm. This innovative class of materials demonstrate striking particle-size-dependent phenomena that affect: (i) emission lifetime; (ii) luminescence quantum efficiency and (iii) concentration quenching. As the size of the crystal decreases there is a continuous transition from bulk to molecular properties with a number of these effects being attributed to quantum confinement or more generally to restricted geometry.

A sub-group of nanocrystalline materials that has attracted considerable attention for use as potential phosphors are rare earth doped yttrium oxide (Y_2O_3) nanocrystals. Micrometer sized $Y_2O_3:Eu^{3+}$ phosphors have been used since the 1970's as the red component in television projection tubes and fluorescent lighting devices.[119] Recently, numerous studies have focused on the optical properties of nano-dimensioned

$Y_2O_3:Eu^{3+}$.[6, 40, 120-122] Tissue et al. have thoroughly investigated and reported results on Eu^{3+} doped monoclinic Y_2O_3 noting changes in the luminescent spectra and lifetime of the red $^5D_0 \rightarrow {}^7F_2$ transition with decreasing particle size.[122]

Upconversion is a process by which excitation to lower lying levels with low energy radiation (e.g. near infrared radiation) results in higher energy emission (e.g. visible and near UV radiation) from higher electronic levels.[73] This process requires the absorption of at least two photons to provide sufficient energy for the upconverted emission to occur. When certain rare-earth ion impurities such as Er^{3+}, Ho^{3+} and Tm^{3+} are introduced in sufficient concentrations into a suitable host lattice, they are capable of upconverting infrared radiation to various shorter wavelengths. The recent advent of low-cost near-infrared (NIR) laser diodes has generated interest in upconversion materials for uses in all-solid state visible lasers. These materials have other possible applications such as phosphors emitting in the visible spectral range, solid-state displays, detectors for the infrared range, or in possible other opto-electronic devices.[123] Trivalent holmium possesses several energy levels in the NIR portion of the spectrum that can be pumped with NIR radiation along with several metastable energy levels ($^5I_6$ and $^5I_7$) which act as good population reservoirs for possible energy-transfer upconversion (ETU) or excited state absorption (ESA) processes. Consequently, there has been a great deal of interest recently in Ho^{3+} doped crystals and glasses as upconversion materials.[123, 124] Several others have demonstrated continuous wave (cw) green upconversion lasing from Ho^{3+} doped glass fibers pumped with red light.[125-128]

In previous studies we have investigated in detail the emission and upconversion spectra of Er^{3+} doped cubic Y_2O_3 and Lu_2O_3 nanocrystals.[13, 15, 16] Others have examined the upconversion of Er^{3+} in sol-gel derived nanocrystalline $BaTiO_3$ powders.[129] To our knowledge, no detailed study of the upconversion properties of Ho^{3+} in a nanocrystal host has yet been performed. In this paper we discuss and report the optical properties of Ho^{3+} doped cubic Y_2O_3 nanocrystals in an attempt to further broaden the understanding of these novel materials.

2.3. EXPERIMENTAL

2.3.1. *Sample preparation*

Nanosized Y_2O_3 crystals doped with 0.1, 0.5, 1, 2, 5 and 10 mol % Ho_2O_3 ($Y_{1.998}Ho_{0.002}O_3$, $Y_{1.99}Ho_{0.01}O_3$, $Y_{1.98}Ho_{0.02}O_3$, $Y_{1.96}Ho_{0.04}O_3$, $Y_{1.9}Ho_{0.1}O_3$ and $Y_{1.8}Ho_{0.2}O_3$, respectively) were prepared using a solution combustion synthesis procedure.[40, 42] Details of the synthesis have been given in a previous article.[15] The synthesis reaction is:

$$6\ M(NO_3)_3 + 10\ NH_2CH_2COOH + 18\ O_2 \rightarrow 3\ M_2O_3 + 5\ N_2 + 18\ NO_2 + 20\ CO_2 + 25\ H_2O$$

where M = Y, Ho. A glycine-to-metal nitrate molar ratio of 1.2:1 was employed to prepare the aqueous precursor solution. According to literature, this nitrate rich composition should allow the formation of small size yttria particles.[40, 42] After the combustion, the powders were fired for 1 hour at 500 °C in order to decompose the residual nitrate ions.

For comparison purposes, bulk $Y_{1.98}Ho_{0.02}O_3$ and $Y_{1.8}Ho_{0.2}O_3$ samples was prepared by conventional solid state reaction. An appropriate amount of powders of Y_2O_3 (Aldrich, 99.99 %) and Ho_2O_3 (Aldrich, 99.99+ %) were intimately mixed, pressed into pellets under 10 tons of pressure and fired in air at 1500 °C for 48 hours. At this temperature, the optimum homogeneity (verified using scanning electron microscopy) was obtained. Spectroscopic measurements were carried out also on these samples, which had undergone this heat treatment.

All yttria samples were kept in air without any further precaution.

2.3.2. *IR spectroscopy*

The diffuse reflectance spectrum in the IR region was measured using a Nicolet Magna 760 FTIR spectrometer with a resolution of 2 cm^{-1}. The sample was carefully mixed with KBr (about 5%) and the spectrum was measured using pure KBr as a reference.

2.3.3. Luminescence spectroscopy

Luminescence spectra were measured by exciting either at 457.9 nm using a Coherent Sabre Innova, 20 W argon ion laser, at 754 nm using a Spectra-Physics Model 3900 Titanium Sapphire pumped by the 514 nm line of a Coherent Sabre Innova argon ion laser, or at 646 nm using a Spectra-Physics 375 dye-laser operating with DCM (Exciton), also pumped by the 514 nm line of the argon laser. The concentration of the dye was 1.2 x 10^{-3} mol/dm^3 in a mixture of benzyl alcohol/ethylene glycol 3:7 (Aldrich, spectrophotometric, 99+ %). The visible emissions were then collected and dispersed using a Jarrell-Ash 1-meter Czerny Turner double monochromator. The signals were monitored with a thermoelectrically cooled Hamamatsu R943-02 photomultiplier tube. A preamplifier, model SR440 Stanford Research Systems, processed the photomultiplier signals and a gated photon counter model SR400 Stanford Research Systems data acquisition system was used as an interface between the computer and the spectroscopic hardware.

2.2.4 Luminescence decay times measurements

Luminescence decay times were measured at each of the excitation wavelengths by modulating the excitation light with a chopper (SR540 Stanford Research Systems). They were recorded using the same gated photon counter mentioned above.

2.4. RESULTS AND DISCUSSION

2.4.1. Particle Size

The average crystallite sizes of the end members of the series under investigation, $Y_{1.998}Ho_{0.002}O_3$ and $Y_{1.8}Ho_{0.2}O_3$, were found to be 13 and 10 nm, respectively, from a line broadening analysis of the 222/444 and 400/800 pairs of X-ray reflections.[43] Moreover, the particle size for $Y_{1.8}Ho_{0.2}O_3$ was confirmed by a detailed structural investigation carried out by small angle X-ray diffraction and electron microscopy.[43] It is therefore reasonable to assume that the sizes of the other members of the series are comparable to these values, as the present synthetic technique appears to be remarkably reproducible, and to yield particle sizes which are independent on the chemical identity and concentration of the lanthanide dopant.[42-44] On the other hand, the size of the particles in the bulk sample is at least 10 times larger.

2.4.2. Luminescence spectroscopy

The room temperature visible luminescence spectra of bulk and nanocrystalline samples excited at 457.9 nm are shown in Figures 2.1. and 2.2. respectively. The spectra exhibit four distinct emission bands. Blue emission was observed between 480-500 nm corresponding to the $^5F_3 \rightarrow {}^5I_8$ transition. The yellow emission in the region of 530-580 nm is attributed to the transition from the thermalized $^5F_4$ and $^5S_2$ states to the $^5I_8$ ground state. Red emission was observed between 630-680 nm corresponding to the $^5F_5 \rightarrow {}^5I_8$ transition. NIR emission was observed between 735-775 nm corresponding to the transition from the thermalized $^5F_4$ and $^5S_2$ states to the $^5I_7$ excited state. The transition energies were similar for both the nanocrystalline and bulk samples and there is no

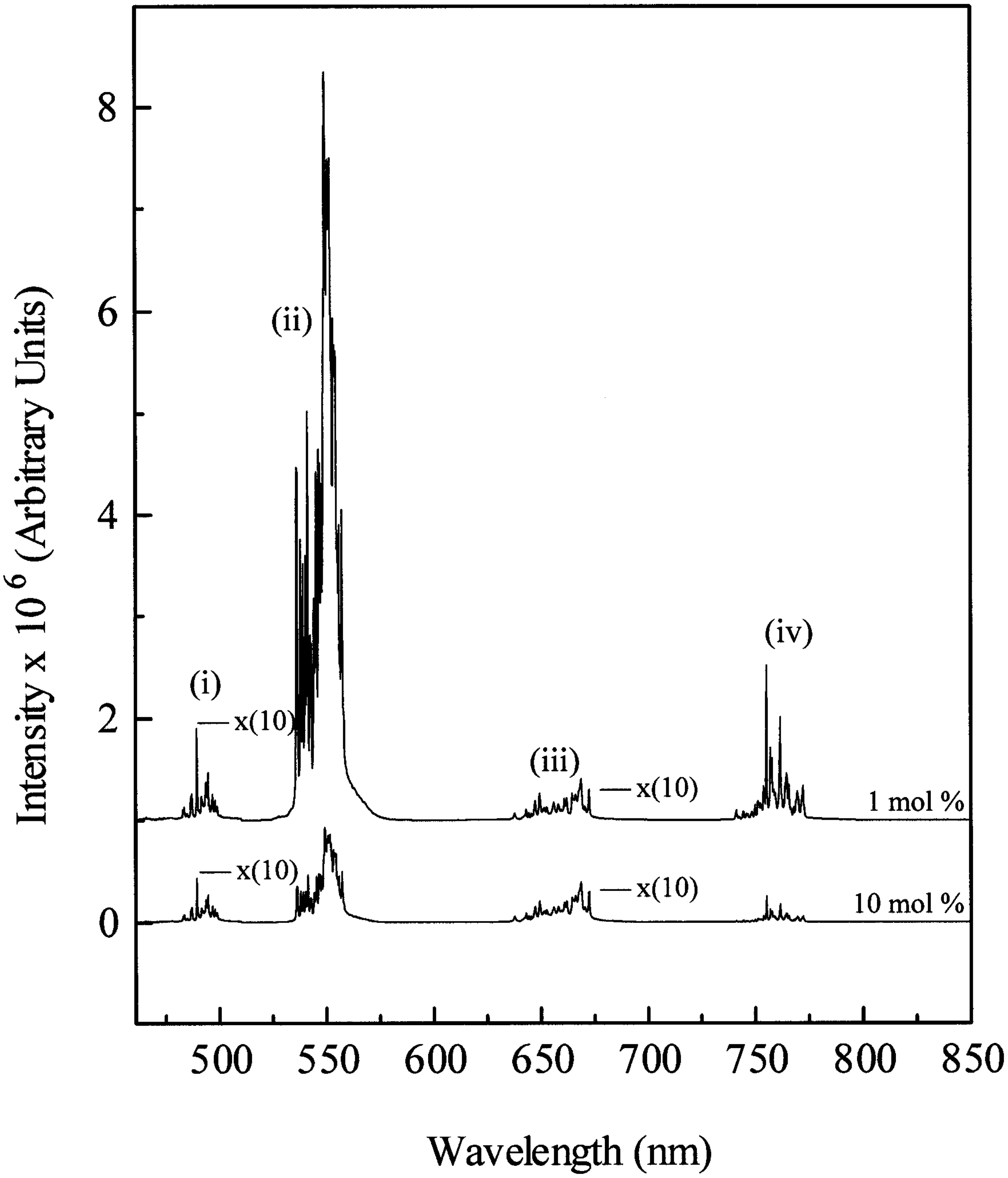

Figure 2.1. Room temperature luminescence of bulk $Y_2O_3{:}Ho^{3+}$ upon excitation at 457.9 nm. (i) $^5F_3 \rightarrow {}^5I_8$ (ii) $({}^5F_4, {}^5S_2) \rightarrow {}^5I_8$ (iii) $^5F_5 \rightarrow {}^5I_8$ (iv) $({}^5F_4, {}^5S_2) \rightarrow {}^5I_7$.

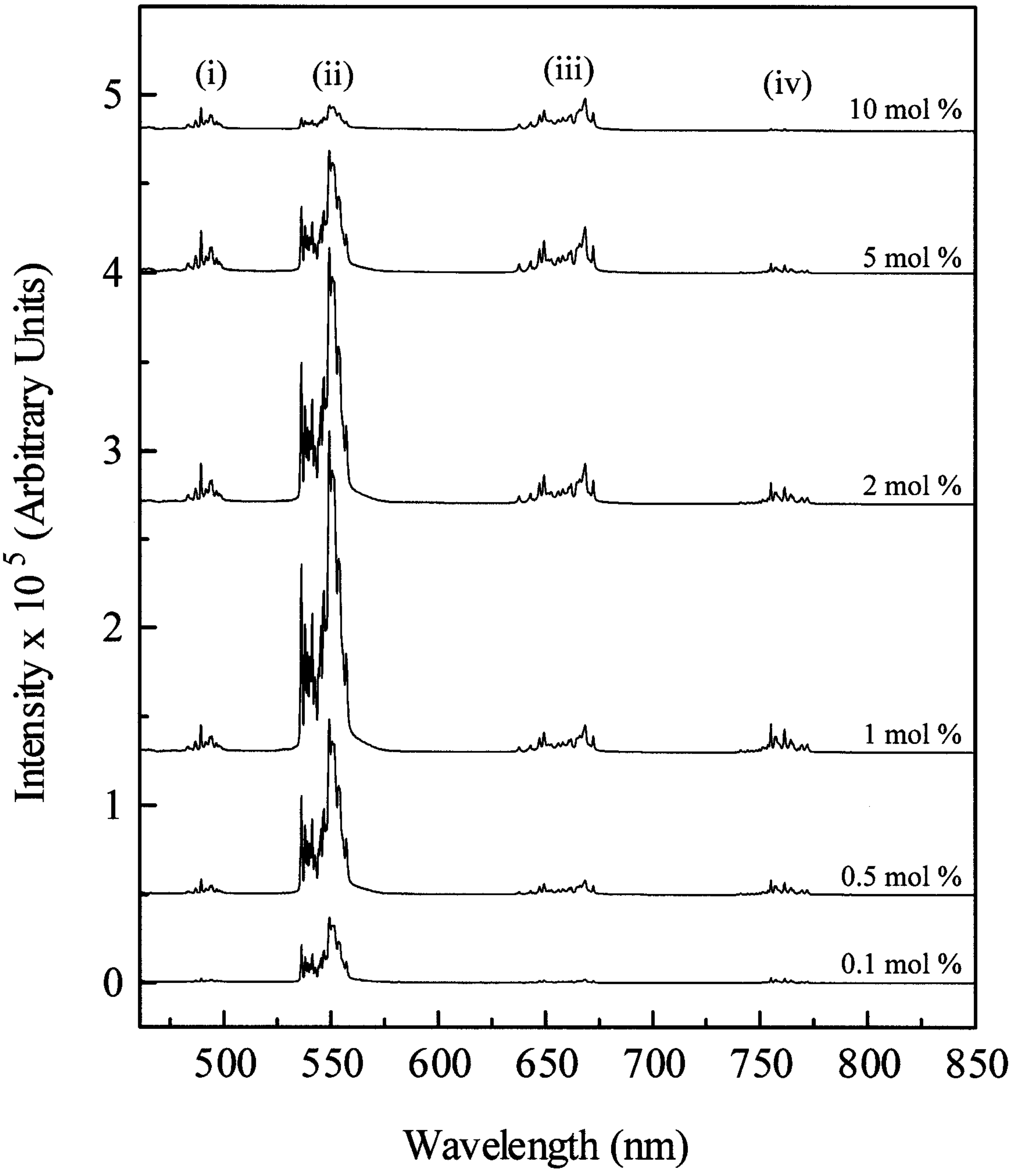

Figure 2.2. Room temperature luminescence of nanocrystalline $Y_2O_3:Ho^{3+}$ upon excitation at 457.9 nm. (i) $^5F_3 \rightarrow {}^5I_8$ (ii) $(^5F_4, {}^5S_2) \rightarrow {}^5I_8$ (iii) $^5F_5 \rightarrow {}^5I_8$ (iv) $(^5F_4, {}^5S_2) \rightarrow {}^5I_7$.

noticeable shifting of peaks in any of the samples. The crystal field energy is therefore reasonably similar for the nanocrystalline and bulk samples.

When comparing the emission spectra of the bulk samples to those of the nanocrystals one notices that the relative intensities of the peaks do change considerably. In the 1% doped nanocrystalline sample the integrated intensity of the $(^5F_4, ^5S_2) \rightarrow ^5I_8$ transition was roughly ten times that of the $^5F_5 \rightarrow ^5I_8$ transition, while in the 1% doped bulk sample the ratio of the relative intensities of these two transitions was approximately 150:1. One also notices that the overall luminescence is severely reduced by about one order of magnitude in the nanocrystal samples compared to the bulk samples. In a previous paper on $Y_2O_3:Er^{3+}$ nanocrystals we have attributed this type of behaviour to an increase in multiphonon relaxation due to adsorbed atmospheric carbon dioxide and/or water.[15]

Similar to the $Y_2O_3:Er^{3+}$ nanocrystals, the medium IR spectra of the nanocrystalline $Y_2O_3:Ho^{3+}$ samples under investigation show that the materials have adsorbed atmospheric CO_2 and H_2O. In fact, the MIR spectra show bands around 1500 and 3400 cm^{-1} which can be attributed to stretching modes of carbonate and hydroxide ions. The presence of these ions on the surface of the nanocrystalline materials yields vibrational quanta of higher wavenumbers compared to the intrinsic phonons of yttria ($\approx$ 600 cm^{-1}) resulting in an increase of multiphonon relaxations from all excited levels under consideration. Since the radiative decay rates for the Ho^{3+} ions in the bulk and nanocrystalline samples should be of the same order of magnitude, the larger non-radiative decay probability in the nanocrystals leads to lower emission efficiencies when compared to their bulk counterparts.

The rapid quenching of the ($^5F_4$, $^5S_2$) → $^5I_8$ transition relative to the $^5F_5$ → $^5I_8$ transition in the nanocrystalline samples can also be attributed to the presence of the adsorbed atmospheric molecules. The conditions necessary for efficient non-radiative decay are well known.[130] In particular, the energy difference ΔE between the levels in question should be equal to or less than 4-5 times the highest vibrational frequency of the surroundings. The energy gap between the $^5S_2$ and $^5F_5$ levels for the Ho^{3+} ion in Y_2O_3 single crystals[131] has been reported to be 2666 cm^{-1}. As this gap is slightly higher than 4 high energy phonons of the bulk material (about 600 cm-1) the $^5S_2$ level is slightly affected by multiphonon decay. In the nanocrystals this gap could be spanned with 2 of the high energy carbonate ion phonons available or just 1 hydroxide high energy phonon making multiphonon relaxation of ($^5F_4$, $^5S_2$) levels much more probable than for its bulk counterpart.

The energy gap between the $^5F_5$ and $^5I_4$ levels is just 1793 cm^{-1}. This gap can be spanned by 3 of the intrinsic yttria phonons meaning it would undergo a significant amount of non-radiative relaxation already in the bulk sample. The multiphonon relaxation quantum efficiency for this level is approximately 1.0 in Y_2O_3 single crystal.[132] In the nanocrystals the number of phonons needed is reduced to slightly more than one if one considers the high energy carbonate ion phonons available or just one hydroxide ion high energy phonon.

In the bulk materials there is a difference of at least one phonon needed for multiphonon decay of the $^5S_2$ and $^5F_5$ levels. If one examines the energy-gap dependence of the spontaneous multiphonon transition rate in single crystal Y_2O_3[66, 132] this would then lead to an approximately 10^2 greater multiphonon relaxation rate for the $^5F_5$ level as compared to the $^5S_2$ level. In the nanocrystalline samples the same number of phonons is needed either in considering carbonate or hydroxide ion high energy phonons for the relaxation of both levels. This should result in a similar rate of multiphonon relaxation for the $^5S_2$ and $^5F_5$ levels in the nanocrystalline samples and therefore a quenching of the ($^5F_4$, $^5S_2$) → $^5I_8$ transition relative to the $^5F_5$ → $^5I_8$ transition when compared to the bulk materials.

In a previous study on Er^{3+} doped nanocrystalline Y_2O_3 different heat treatments were carried out on a nanocrystalline $Y_{1.8}Er_{0.2}O_3$ sample in order to reduce the amount of carbonate and hydroxide ions on the surface of the nanoparticles.[14] First, the sample was treated at 800 °C for 17 hours and subsequently cooled to room temperature. The same sample was then treated at 1000 °C for 65 hours and again cooled to room temperature. The MIR spectra of the doped nanocrystalline yttria sample after both heat treatments still showed bands at approximately 1500 and 3350 cm^{-1}, which indicated the presence of carbonate and hydroxide ions, respectively. On the other hand, the bulk sample showed no bands at 1500 and 3350 cm^{-1} indicating the lack of carbonate and hydroxide ions. A reduction of the overall intensities of the bands at 1500 and 3350 cm^{-1} after both heat treatments was noted indicating a reduction, not a complete removal, of the overall surface contamination. A consequence of these long heat treatments at higher temperatures is a possible aggregation (combination) of the nanoparticles to form larger particles. This creates a difficulty in comparing the luminescence of heat-treated and non-heat treated nanocrystalline materials as the spectroscopy of the nanocrystalline material is particle size dependent.

When examining the behaviour of the relative intensities of the ($^5F_4$, $^5S_2$) → $^5I_8$ transition to the $^5F_3$ → $^5I_8$ and $^5F_5$ → $^5I_8$ transitions in the bulk and nanocrystalline samples, one notices a rapid quenching of the ($^5F_4$, $^5S_2$) → $^5I_8$ transition as the Ho^{3+} dopant concentration increases from 1% to 10%. This type of behaviour suggests a rapid energy transfer from the ($^5F_4$, $^5S_2$) level. For samples with Ho^{3+} concentration less than 1%, non-radiative relaxation by ion-ion interactions can be assumed to be negligible. As the concentration increases the continuous spectral changes observed indicate that interactions between ions develop at doping levels above 1%. By examining the energy levels of Y_2O_3:Ho^{3+} [131] one is capable of elucidating ion-pair cross-relaxation processes that are likely to occur. One such resonant cross-relaxation is represented by the $^5S_2$ → $^5I_4$ and $^5I_7$ ← $^5I_8$ transitions. In this energy transfer process a donor Ho^{3+} ion in the $^5S_2$ excited state relaxes non-radiatively to the $^5I_4$ state, while in another simultaneous nonradiative process an acceptor Ho^{3+} ion in a ground $^5I_8$ state is excited to the $^5I_7$ state, thereby quenching the luminescence of the ($^5F_4$, $^5S_2$) level. This energy transfer from the ($^5F_4$, $^5S_2$) level is well documented and has also been observed in Ho^{3+} doped $ZnCl_2$-based glasses[133] and $YAlO_3$:Ho^{3+} crystals.[134] The concentration quenching observed in the nanocrystal samples can be attributed to this cross relaxation process.

2.4.3. Emission Decay Times

Room temperature emission decay curves of the ($^5F_4$, $^5S_2$) → $^5I_8$ transition upon 457.9 nm excitation were monitored for both the bulk and nanocrystalline samples. The lifetimes are reported in Table 2.1. Decay curves for the bulk samples were fitted with a single exponential model. However, a deviation from first exponential behaviour was observed in all decay curves obtained for the nanocrystalline samples. The difficulty in fitting with a single exponential model in the more diluted nanocrystalline samples (0.1 – 2 mol%) arises because there is a distribution of dopant ions within the individual nanocrystals that are coupled in various degrees to the absorbed surface molecules. The dopant ions located close to the surface would have a faster decay than those ions located inside the nanocrystals. This distribution of ions thus leads to a non-exponential decay as a significant portion of the dopant atoms reside near the surface due to the particles' small size (about 10 nm).

Table 2.1. Decay times obtained from an exponential fit of the room temperature decay curves for the ($^5F_4$, $^5S_2$) → $^5I_8$ transition upon 457.9 nm excitation.

Sample	Decay time (μs)	
Bulk		
$Y_{1.98}Ho_{0.02}O_3$	135	
$Y_{1.80}Ho_{0.20}O_3$	60	
Nanocrystalline	**1st Decay time (μs)**	**2nd Decay time (μs)**
$Y_{1.998}Ho_{0.002}O_3$	17	77
$Y_{1.99}Ho_{0.01}O_3$	20	73
$Y_{1.98}Ho_{0.02}O_3$	14	57
$Y_{1.96}Ho_{0.04}O_3$	9	40
$Y_{1.90}Ho_{0.10}O_3$	3	14
$Y_{1.80}Ho_{0.20}O_3$	2	4

It is possible to fit the curves of the nanocrystalline samples with a double exponential model since theoretically; one would expect two time constants: one for the ions at the surface and a second for the ions inside the nanocrystals. The value of the first time constant is relatively low with respect to the second one and both remain reasonably constant in the low concentration regime (0.1 mol% - 1 mol%). This behaviour is not observed in the samples with dopant concentrations greater than 1 mol% as the decay process in now influenced by the energy transfer process between the holmium ions.

Both time constants decrease steadily as the concentration of the dopant ion is raised. As the concentration of the dopant ion is increased up to 5 mol% the deviation from first order exponential behaviour increases as interactions between the dopant ions become significant. As mentioned previously, a strong cross-relaxation process involving energy transfer between two holmium ions is observed which depopulates the ($^5F_4$, $^5S_2$) level. This process increases the rate of nonradiative relaxations thus explaining the rapid decrease of the lifetime of this level with increasing Ho^{3+} concentration.

The lifetimes of the excited states were found to be significantly shorter in the nanocrystal samples than in the bulk samples. For example, the ($^5F_4$, $^5S_2$) → $^5I_8$ lifetime in the 1 mol% bulk sample was found to be 135 μs as opposed to 14 μs (1st time constant) or 57 μs (2nd time constant) in the similarly doped nanocrystalline sample. The lifetime of an excited state **a** is given by:

$$\frac{1}{\tau_c} = \sum_b \left(A_{ab} + W_{ab}\right)$$

where A_{ab} and W_{ab} are the radiative and nonradiative transition probabilities respectfully from level **a** to level **b**, and the summation is over all terminal levels **b** [135]. Nonradiative processes include multiphonon relaxations and energy transfer between ions. Differences in the rate of nonradiative decay from a given rare-earth level arise from the highest phonon energy available in the sample and the number of phonons required to bridge the energy gap. Because phonons of higher energy are present in the nanocrystals as opposed to the bulk samples, nonradiative transitions from the ($^5F_4$, $^5S_2$) level to the $^5F_5$ level will require a lower-order multiphonon process resulting in a rapid relaxation. This accounts for the larger rate of nonradiative processes in the nanocrystalline samples for a given size energy gap. The resulting lifetime of the ($^5F_4$, $^5S_2$) level is therefore shorter.

2.3.4. Upconversion upon excitation into the $^5F_5$ manifold

Upon excitation with 646 nm radiation from a dye laser that populates the $^5F_5$ level, anti-Stokes emission corresponding to the $^5F_3 \rightarrow {}^5I_8$ and ($^5F_4$, $^5S_2$) $\rightarrow {}^5I_8$ transitions were observed. The luminescence spectra of the bulk and nanocrystalline samples are shown in Figure 2.3. and 2.4. respectively. The intensity of the upconverted luminescence I_o is proportional to some power n of the pump intensity I_i ($I_o \alpha I_i^n$) [136] where n, which is called the order of the upconversion process, is the number of pump photons required to populate the emitting state. The intensity of the upconverted blue and green emission has been measured as a function of the 646 nm excitation intensity. From a fit of the curve $\ln I_i$ versus $\ln I_0$ we have obtained a slope of 1.9, which indicates a two-photon upconversion process, as shown in Fig. 2.5.

The decay times of the ($^5F_4$, $^5S_2$) $\rightarrow {}^5I_8$ upconversion transition are identical to those obtained with 457.9 nm excitation for all the concentrations. No change in the relative intensity of the blue and green luminescence between the direct emission and upconversion spectra is observed. An energy transfer upconversion (ETU) process seems to be unlikely because the upconversion luminescence decreases with increasing Ho^{3+} concentration. If an ETU process were occurring the luminescence should increase with

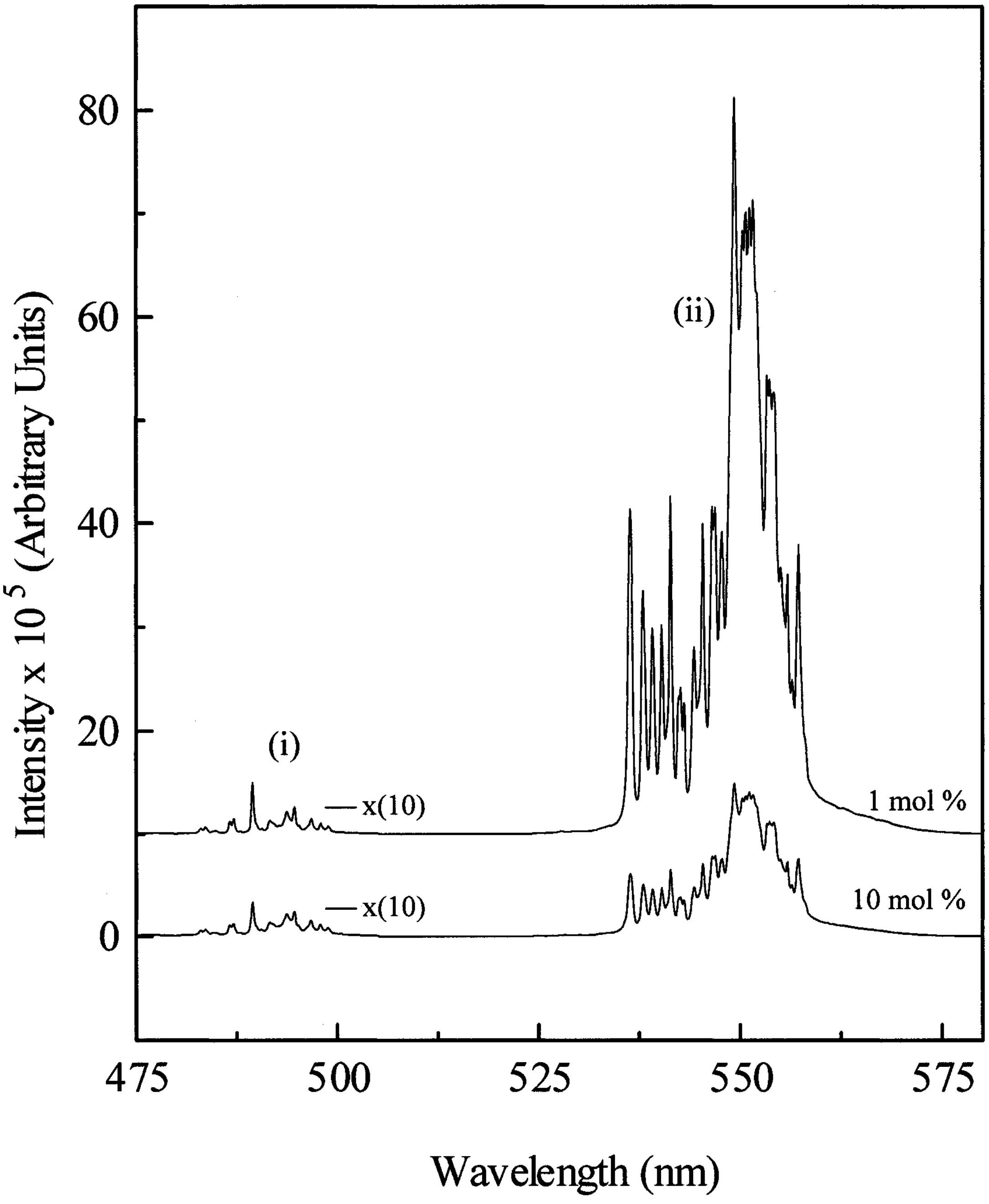

Figure 2.3. Upconverted emission of bulk Ho^{3+} doped Y_2O_3 at room temperature upon 646 nm excitation, showing (i) $^5F_3 \rightarrow {}^5I_8$ and (ii) $(^5F_4, {}^5S_2) \rightarrow {}^5I_8$.

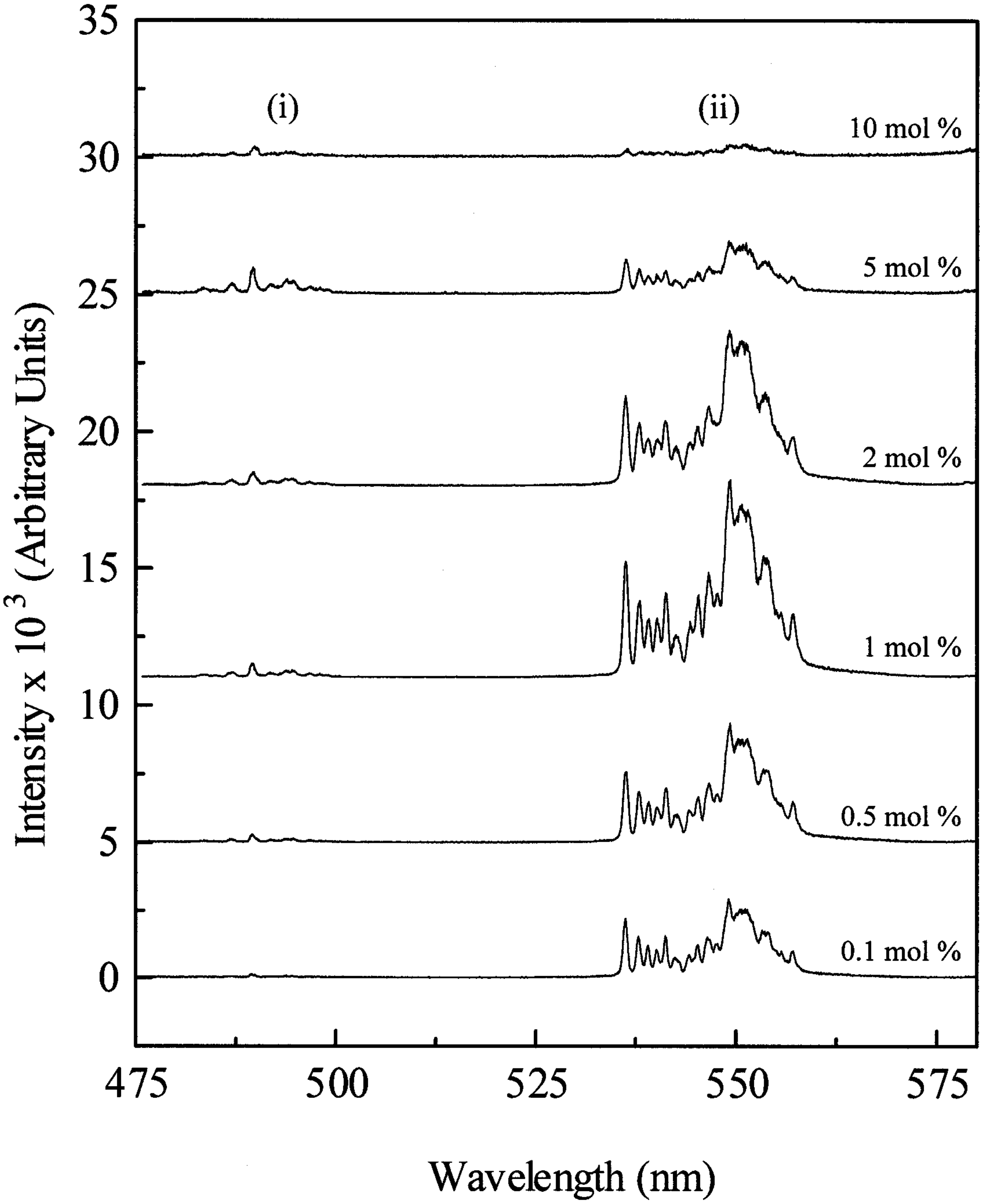

Figure 2.4. Upconverted emission of Ho^{3+} doped Y_2O_3 nanocrystals at room temperature upon 646 nm excitation, showing (i) $^5F_3 \rightarrow {}^5I_8$ and (ii) $(^5F_4, {}^5S_2) \rightarrow {}^5I_8$.

increasing dopant concentration as the distance between the holmium atoms would decrease, thus favouring energy transfer. A photon avalanche upconversion process is also ruled out as no power threshold for the upconversion luminescence is observed. Based on these observations we propose that the upconversion most probably results from an excited state absorption (ESA) process.

The $^5I_5$, $^5I_6$ and $^5I_7$ multiplets are typically long lived with appropriate energy gaps to upper emitting levels. For 646 nm excitation excited state absorption from $^5I_7$ is most likely to occur because there is appropriate resonance $^5I_7 \rightarrow {}^5F_3$. The mechanism by which the ($^5F_4$, $^5S_2$) and $^5F_5$ levels are populated is assigned as follows (Figure 2.7.). The laser light brings the Ho^{3+} ion into the $^5F_5$ level, which then non-radiatively decays to the $^5I_7$ level. An excited state absorption process brings the ion to the $^5F_3$ level. The ion then emits through the $^5F_3 \rightarrow {}^5I_8$ transition or can non-radiatively decay to the lower lying levels and the ($^5F_4$, $^5S_2$) $\rightarrow {}^5I_8$ transition occurs.

The upconversion process was noted to be far less efficient in the nanocrystal samples. This decrease in luminescence is attributed to an increase of multiphonon relaxations of excited levels because of the presence of carbonate and hydroxide ions on the surface of the nanocrystals. The populations of the intermediate levels from which a part of the excited ions can be re-excited to the upper emitting levels by excited state absorption (ESA) are substantially impacted by the non-radiative decay rate that increases as the lattice phonon energy becomes higher.[137] The highest available phonon energy not only affects quantum efficiencies of the emitting levels such as $^5F_3$ and $^5S_2$ levels but also impacts the upconversion efficiencies, which are primarily determined by populations of intermediate levels such as the $^5I_6$ and $^5I_7$. The excitation populations of

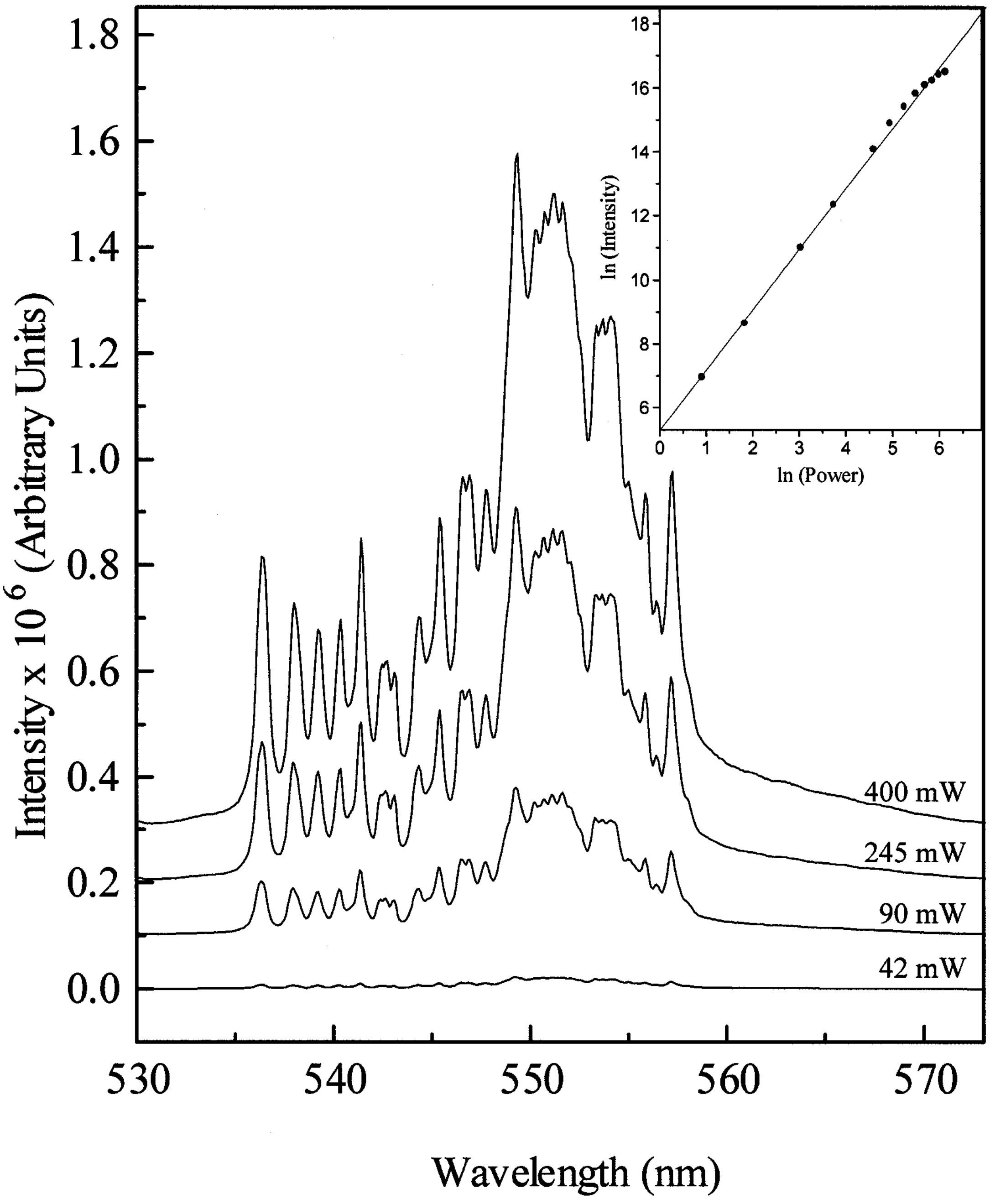

Figure 2.5. Power study of the ($^5F_4$, $^5S_2$) → $^5I_8$ transition in 10 mol% bulk Y_2O_3:Ho^{3+} at room temperature upon 646 nm excitation. Inset: Power dependence of the upconversion luminescence intensity observed with 646 nm excitation.

intermediate levels and the quantum efficiencies of emitting levels of Ho^{3+} in a host crystal with a higher phonon energy are undoubtedly lower than those in a crystal with a lower phonon energy.

2.4.5. Upconversion upon excitation into the $^5I_4$ manifold

Upon excitation with 754 nm radiation from a Titanium Sapphire laser that excites the $^5I_4$ level, anti-Stokes emission corresponding to the $^5F_3 \rightarrow {}^5I_8$; $(^5F_4, {}^5S_2) \rightarrow {}^5I_8$; and $^5F_5 \rightarrow {}^5I_8$ transitions were observed in the bulk samples. The luminescence spectra are shown in Figure 2.6. Though strong luminescence was observed from the bulk samples no upconversion was noted in the nanocrystal samples. As mentioned previously, behaviour of this type is attributed to an increase of multiphonon relaxations of excited levels because of the presence of carbonate and hydroxide ions on the surface of the nanoparticles.

The $(^5F_4, {}^5S_2) \rightarrow {}^5I_8$ transition demonstrated a quadratic dependence on the power of the pump beam indicating that two photons were involved in the excitation process. Again an excited state absorption (ESA) process is thought to be the dominant mechanism for the same reasons mentioned previously for upconversion using 646 nm radiation: the decay times of the $(^5F_4, {}^5S_2) \rightarrow {}^5I_8$ upconversion transition are identical to those obtained with 457.9 nm excitation, no power threshold for the upconversion emission was noted and the upconversion luminescence decreases with increasing Ho^{3+} concentration.

Another possible reason mentioned previously for justifying an ESA process, no change in the relative intensity of the blue and green luminescence between the direct emission and upconversion spectra, does not apply in this case but can easily be

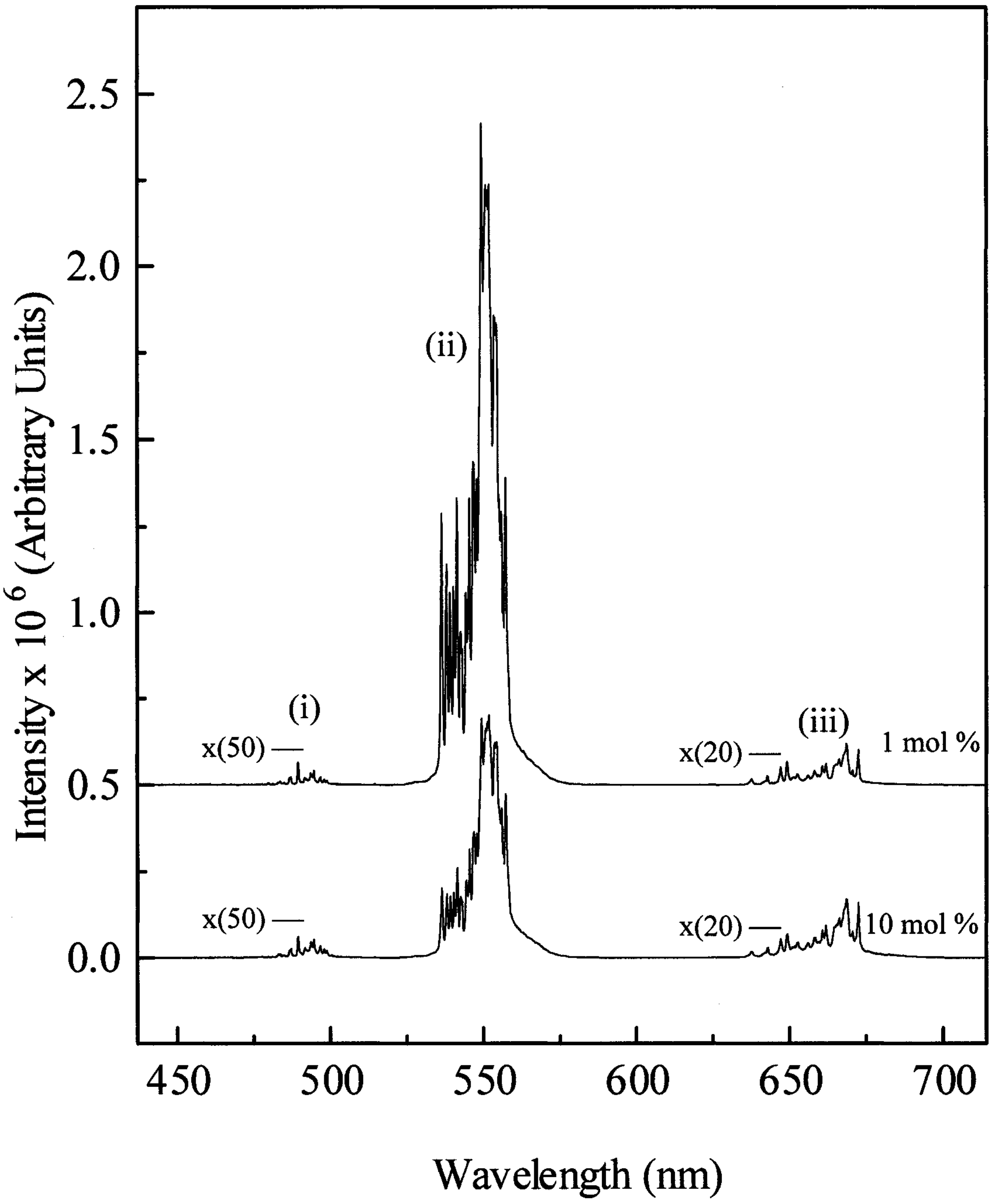

Figure 2.6. Upconverted emission of bulk Ho^{3+} doped Y_2O_3 at room temperature upon 754 nm excitation, showing (i) $^5F_3 \rightarrow {}^5I_8$, (ii) $({}^5F_4, {}^5S_2) \rightarrow {}^5I_8$ and (iii) $^5F_5 \rightarrow {}^5I_8$.

explained. The relative intensity of the blue emission transition compared to the green one is severely reduced upon 754 nm excitation. The reason for this behaviour is that there are two distinct ESA processes occurring concurrently that originate from the $^5I_6$ and $^5I_7$ levels and could populate the $^5G_6$, $^3K_8$ and ($^5F_4$, $^5S_2$) levels respectively. It is well known that the $^5I_7$ level possesses a longer lifetime and a larger radiative character than the $^5I_6$ level, thus excited state absorption from $^5I_7$ rather than the $^5I_6$ level is most likely to occur. Therefore the proposed mechanism is the following (Figure 2.7.). The laser light brings the Ho^{3+} ion into the $^5I_4$ level, which then non-radiatively decays to the $^5I_7$ level. An excited state absorption process brings the ion to the ($^5F_4$, $^5S_2$) levels. The ion then emits through the ($^5F_4$, $^5S_2$) $\rightarrow$ $^5I_8$ transition or can non-radiatively decay to the lower lying levels and the $^5F_5 \rightarrow {}^5I_8$ transition occurs. This mechanism is further aided by an increase in the population of the $^5I_7$ level via the cross-relaxation mechanism mentioned previously. The increase in the population of the $^5I_7$ level leads to the efficient population of the ($^5F_4$, $^5S_2$) levels through the ESA process and to the intense green emission. A second ESA process originating from the $^5I_6$ level is also possible. For the 754 nm excitation wavelength used in this study there is another possible resonant excited state absorption: $^5I_6 \rightarrow {}^3K_8, {}^5G_6$. It is most likely this ESA process along with non-radiative relaxation which is responsible for the weak blue emission from the $^5F_3$ level noted in Figure 2.5.

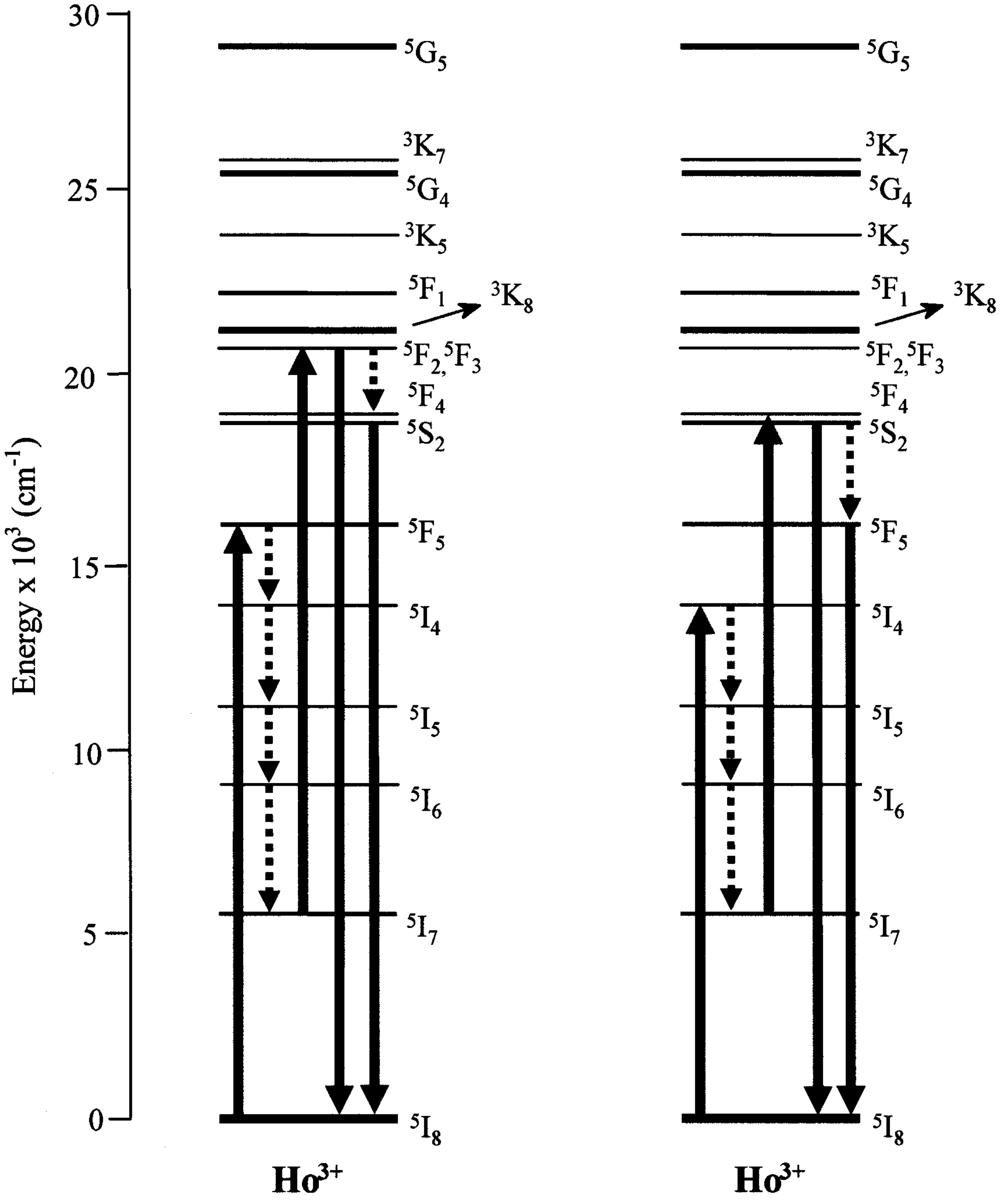

Figure 2.7. Two excitation mechanisms for Ho^{3+} upconversion in Y_2O_3: (left) 646 nm excitation resulting in excited state absorption via the $^5I_7$ level (right) 754 nm excitation resulting in excited state absorption via the $^5I_7$ level.

2.5. CONLUSIONS

Emission spectra and lifetimes of the excited states of the nanocrystal samples differ significantly from those of the bulk. The upconverted intensity at both excitation wavelengths was found to decrease with increasing holmium concentration, which suggests a ESA type mechanism. Upconversion processes are far less efficient, or nonexistent, in the nanocrystalline samples due to the presence of carbonate ions and water on the surface. The bulk material shows enhanced green emission ($^5F_4$, $^5S_2 \rightarrow {}^5I_8$) over its nanocrystal counterpart in both the emission and upconversion spectra.

2.6. AUTHOR'S NOTES AND SIGNIFICANCE OF THIS PAPER

This work on Ho^{3+} doped nanocrystalline Y_2O_3 was the first article published in the literature on the spectroscopic and upconversion properties of Ho^{3+} doped oxide nanocrystals. It also was the first recorded instance of Ho^{3+} upconversion in a nanocrystalline oxide material. This study has shown that the luminescence and upconversion of the holmium ions is severely reduced in Y_2O_3 nanocrystals compared to bulk samples. My studies have determined that, while upconversion occurs in bulk samples, it is severely reduced or nonexistent in the nanocrystal samples. This behaviour is attributed to adsorbed atmospheric carbon dioxide and/or water on the surface of the nanocrystals. This publication was a landmark in nanocrystalline research as it paved the way for future studies on Ho^{3+} doped nanocrystalline materials.

The following chapter presents our work on the spectroscopy, fluorescence liftimes and Judd-Ofelt parameters of Eu^{3+} doped nanocrystalline Lu_2O_3. Though Lu_2O_3 is a different host than the one utilized in the previous study, it is isostrutural to Y_2O_3 as both possess a cubic crystal structure with the same space group and symmetry. At the time of this study, initial research in our lab on other lanthanide doped Lu_2O_3 nanocrystalline samples indicated that this host might allow for high upconversion efficiencies than Y_2O_3. Thus we though it imperative to examine in detail the effect the nanocrystalline host has on the spectroscopy of the lanthanide ions. The europium ion was chosen as the dopant ion as it is a useful optical probe for ion-host interactions due to its relatively simple excitation and emission spectrum in the visible portion of the spectrum.

Chapter 3

Variation of Fluorescence Lifetimes and Judd-Ofelt Parameters between Eu^{3+} Doped Bulk and Nanocrystalline Cubic Lu_2O_3

Published as:

J. C. Boyer, F. Vetrone, J. A. Capobianco, A. Speghini and M. Bettinelli

Journal of Phyical Chemistry B **2004**, *108*, 20137-20143.

3.1. ABSTRACT

The luminescent properties of 1mol % Eu^{3+}-doped cubic Lu_2O_3 nanocrystals prepared by a combustion synthesis route were investigated. The visible emission spectrum of the europium doped Lu_2O_3 nanocrystals indicate that the structural environment surrounding the dopant Eu^{3+} ion is distorted when compared to a bulk sample with a micrometer particle size. From the resulting emission spectra, the Ω_2 and Ω_4 Judd-Ofelt intensity parameters were calculated. The lifetimes of the $^5D_0$ excited state for both the C_2 and C_{3i} sites were found to be nearly double that found for a similarly doped sample with larger particle size (bulk sample). This behaviour is attributed to a change in the refractive index of the nanocrystalline material that in turn modifies the oscillator strength of the $4f \leftrightarrow 4f$ transitions.

3.2. INTRODUCTION

Over the past several years there has been an ongoing search for nanometer sized powdered phosphors with superior performance characteristics over their micrometer counterparts. This research has been stimulated by the fact that significant changes in the optical properties have been observed with decreasing particle size.[122] Currently, phosphors in the micrometer size range find applications in a wide variety of information display devices such as cathode-ray tubes (CRTs), field emission displays (FEDs), vacuum fluorescent displays (VFDs) and electroluminescent (EL) devices.[45] It is anticipated that the advent of nano-sized phosphors could lead not only to improved resolution in these devices but also to an increase in luminescent efficiency. Research in the realms of nanocrystalline phosphors ranges from bandgap semiconductors to lanthanide-doped insulators such as the common red phosphor Eu^{3+} doped Y_2O_3.

Nanocrystalline materials are usually defined as polycrystalline solids with particle diameters or grain sizes less than 100 nm.[7] Particle-size-dependent phenomena have been noted in several materials. The properties affected are: (i) emission lifetime; (ii) luminescence efficiency and (iii) concentration quenching. Recently, numerous studies have focused on the optical properties of nano-dimensioned $Y_2O_3:Eu^{3+}$. In particular, Tissue et al. have thoroughly investigated and reported results on Eu^{3+} doped monoclinic Y_2O_3 noting changes in the luminescent spectra and lifetime of the red $^5D_0 \rightarrow {}^7F_2$ transition with decreasing particle size.[7, 120-122]

Over the past few years, our research groups have examined the spectroscopic and upconversion properties of lanthanide doped nanocrystalline cubic Y_2O_3.[13, 47, 138] Recently we have turned our attention to rare-earth doped lutetium oxide (Lu_2O_3)

nanocrystals[16, 88, 139] since it has been observed that when comparing the emission properties of Y- and Lu-containing oxide and fluoride crystals, stronger luminescence is observed for the Lu- containing crystals.[140, 141] An explanation for this behaviour can be found in the results of Guillot-Noël et al.[142] The authors attributed the increase in oscillator strength in related crystals to an intensity-borrowing mechanism that mixes the 4*f* and 5*d* lanthanide orbitals via the lattice valence band levels. In YVO_4 for example, these valence band energy levels are due predominantly to the oxygen 2*p*.

Recent XPS measurements on $LuVO_4$ and various kinds of materials for scintillator applications such as $LuAlO_3$ and Lu_2SiO_5 have shown that the top of the valence band would be more characteristic of lutetium 4*f* levels.[143, 144] This means that the intensity-borrowing mechanism mentioned above could be further enhanced because of an increasing hybridization of the Eu^{3+} and Lu^{3+} 4*f* orbitals.[143] Thus lutetium could be a more favourable cation than yttrium for lanthanide dopant emission.

Nanocrystalline Lu_2O_3 doped with lanthanides has garnered much attention recently for use as X-ray scintillators and/or potential phosphors. Zych et al. have examined Eu^{3+} doped Lu_2O_3 synthesized by a combustion technique using urea as the fuel for these potential uses.[145-147] These materials are attractive for X-ray scintillators because of the high density of Lu_2O_3 and the high atomic number of Lu.[148] Furthermore, micrometer sized $Y_2O_3:Eu^{3+}$ phosphor, which is isostructural to Lu_2O_3, has been used since the 1970's as the red component in television projection tubes and fluorescent lighting devices.[119]

In this paper, we present a detailed examination of the luminescent properties of cubic nanocrystalline Lu_2O_3 doped with 1 mol% Eu^{3+} synthesised via a combustion synthesis technique utilising glycine as the fuel. These results are compared to a cubic bulk Lu_2O_3 doped with 1 mol% Eu^{3+} sample synthesised using a traditional ceramic technique with crystallite sizes in the micron range.

3.3. EXPERIMENTAL

3.3.1. Samples preparation

Nanosized Lu_2O_3 crystals of composition $Lu_{1.98}Eu_{0.02}O_3$ were prepared using a solution combustion synthesis procedure.[40, 42] The synthesis reaction is:

$$6\ M(NO_3)_3 + 10\ NH_2CH_2COOH + 18\ O_2 \rightarrow 3\ M_2O_3 + 5\ N_2 + 18\ NO_2 + 20\ CO_2 + 25\ H_2O$$

where M = Lu, Eu. A glycine-to-metal nitrate molar ratio of 1.2:1 was employed to prepare the precursor solution resulting in a flame temperature of approximately 1200 °C. After the combustion, the powders were fired for 1 hour at 500 °C in order to decompose the residual nitrate ions. A thorough structural analysis of the material obtained showed that the average crystallite size is 50 nm[139] and therefore larger than the size of the yttria nanocrystals obtained using the same conditions (about 10-20 nm).[43]

For comparison purposes, a bulk sample of the same composition as the nanocrystalline one was prepared by intimately mixing Eu_2O_3 (Aldrich, 99.99 %) and Lu_2O_3 (Aldrich, 99.99+ %), pressing the powders into pellets under a load of 10^3 kg and firing them in air at 1500 °C for 48 hours. At this temperature, the optimum homogeneity was obtained.

All lutetia samples were kept in air without any further precautions.

3.3.2. Emission spectroscopy

Luminescence spectra were measured by exciting at 257.25 nm using a Coherent Model 440 Ultraviolet Generator which frequency doubled the 514.5 nm line of a Coherent Sabre Innova, 20 W argon laser. Site selective spectroscopy was performed using 580.5 nm or 582.5 nm radiation from a Spectra-Physics 375 tuneable dye-laser operating with Rhodamine 6G (Exciton) pumped by the 514 nm line of the argon laser.

The visible emissions were then collected and dispersed using a Jarrell-Ash 1-meter Czerny Turner double monochromator. The signals were monitored with a thermoelectrically cooled Hamamatsu R943-02 photomultiplier tube. A preamplifier, model SR440 Stanford Research Systems, processed the photomultiplier signals and a gated photon counter model SR400 Stanford Research Systems data acquisition system was used as an interface between the computer and the spectroscopic hardware. The signal was recorded under computer control using the Stanford SR465 software data acquisition/analyzer system.

All low temperature spectra were obtained using a Janis Research ST-VP-4 continuous flow cryostat with the temperature being monitored by a LakeShore model 330 controller.

3.3.3. Decay times measurements

Luminescence decay times were measured at each of the excitation wavelengths by modulating the excitation laser beam with a Stanford Research Systems optical chopper (Model SR540). The photon counter was triggered by a photodiode synchronized by the laser pulse. They were recorded using the same detection equipment and gated photon counter mentioned above.

3.4. RESULTS AND DISCUSSION

3.4.1. Luminescence spectroscopy

The sesquioxide Lu_2O_3 is isostructural to Y_2O_3 and crystallizes in a cubic bixbyite structure with space group Ia3.[149] In this lattice, two distinct sites are available for rare earth ions, one with point-group symmetry C_2 and the other with point group symmetry C_{3i}, which occur in a 3:1 ratio respectively. It was reported recently by some of us that the Eu^{3+} ions occupy both these sites in a statistical way for the nanocrystalline sample similar to what is observed for bulk crystals.[150] The presence of Eu^{3+} ions in both sites is reflected in the luminescent and spectral properties of the material. A phonon assisted energy transfer mechanism that occurs between the Eu^{3+} ions residing in the two sites has been studied by Buijs et al.[151]

The observed optical transitions within the $4f^n$ configuration are mainly attributed to electric dipole transitions, which are forced by the odd parity components of the crystalline electric field. For C_{3i} symmetry only magnetic dipole transitions should be observed. For the $^5D_0 \rightarrow {}^7F_1$ transition of the Eu^{3+} ion in the cubic bixbyite structure, five emission peaks should be present: two peaks that are attributed to Eu^{3+} ions residing in C_{3i} sites and three peaks for Eu^{3+} in C_2 sites. These peaks have been assigned on the basis of their different emission decay times.[152] Of the two possible radiative decay mechanisms, forced electric dipole and magnetic dipole, only the latter will occur for Eu^{3+} ions in C_{3i} sites thus resulting in a longer decay time.

After excitation into the Eu^{3+}-O^{2-} charge transfer band with 257.25 nm radiation at room temperature, emission can be observed in the orange-red region of the spectrum resulting from the $^5D_0 \rightarrow {}^7F_0$, $^7F_1$, $^7F_2$ transitions. The UV radiation is absorbed by the charge transfer band of the Eu^{3+} ion. The ion then non-radiatively decays to lower $4f^n$ levels with the majority of the luminescence occurring from the $^5D_0$ state of the Eu^{3+} ion. The room temperature luminescence spectra of bulk and nanocrystalline Lu_2O_3:Eu 1 mol% are shown in Figure 3.1. Assignment of the individual peaks to their corresponding transitions was performed based on data obtained previously for $Lu_2O_3:Eu^{3+}$,[153, 154] published data on the isostructural material $Y_2O_3:Eu^{3+}$,[131] luminescence decay times of the individual peaks, time-resolved spectroscopy and site-selective spectroscopy (see below). Table 3.1. lists the room temperature and 78 K transition energies found for the Eu^{3+} ion located in the C_2 and C_{3i} sites of the Lu_2O_3 bulk and nanocrystalline materials.

Table 3.1. Observed transition energies from the emission spectra of bulk and nanocrystalline $Lu_2O_3:Eu^{3+}$ 1 mol% at RT and 78 K.

Transition	**Transition Energy (cm^{-1})**			
	Bulk Sample		***Nanocrystalline Sample***	
	RT	**78 K**	**RT**	**78 K**
$^5D_0 \rightarrow {}^7F_0$	17224	17217	17226	17215
$^5D_0 \rightarrow {}^7F_1$	17166*, 17032, 16864*, 16850, 16652	17171*, 17025, 16866*, 16848, 16659	17170*, 17032, 16871*, 16850, 16652	17169*, 17024, 16868*, 16846, 16655
$^5D_0 \rightarrow {}^7F_2$	16358, 16319, 15818	16358, 16314, 16256, 15814	16356, 16318, 16270, 15818	16356, 16315, 16254, 15811

* Denotes emission from Eu^{3+} ion residing in C_{3i} site

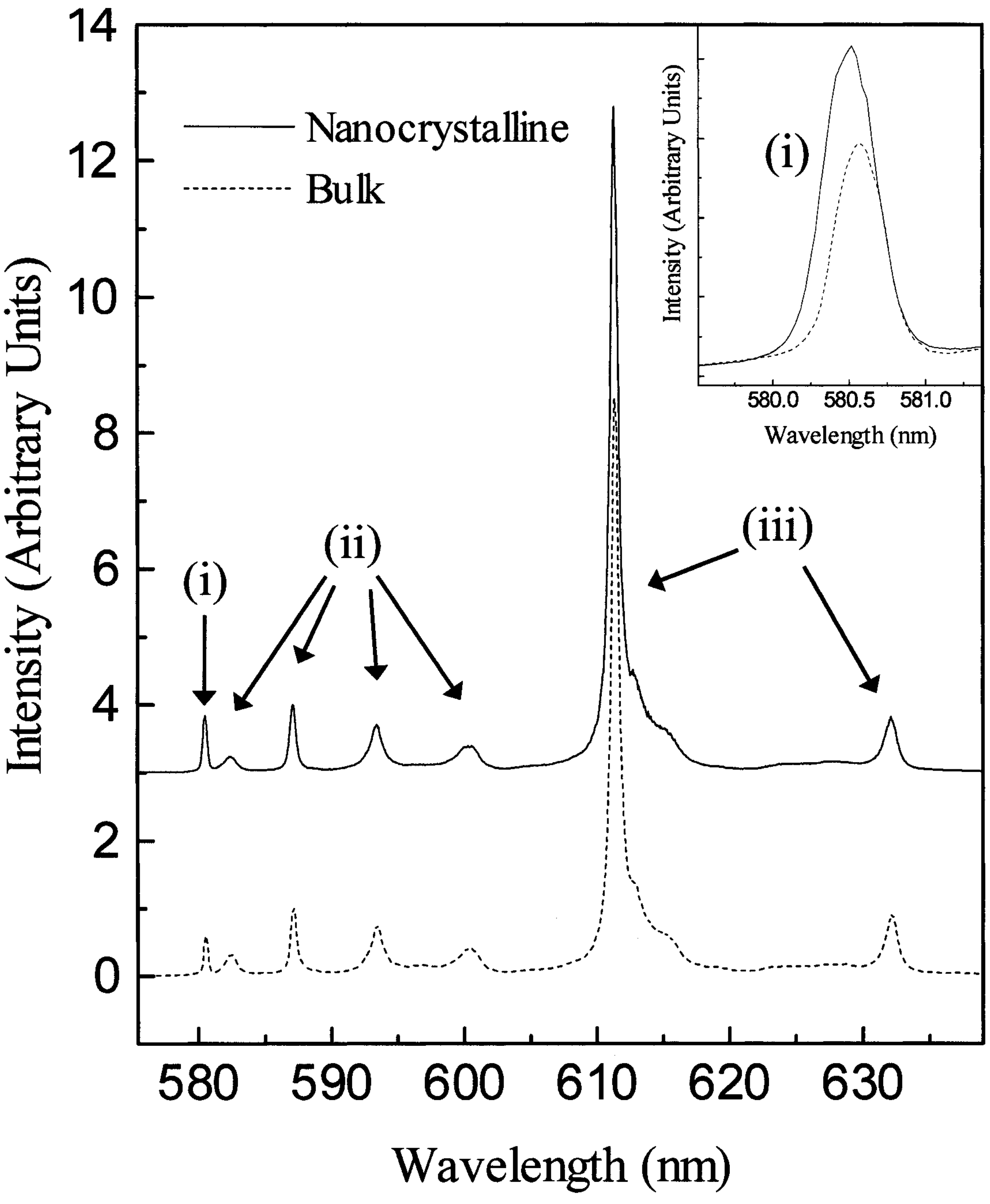

Figure 3.1. Room temperature orange-red luminescence of bulk and nanocrystalline $Lu_2O_3:Eu^{3+}$ 1 mol% upon excitation at 257.25 nm. (i) $^5D_0 \rightarrow {}^7F_0$ (ii) $^5D_0 \rightarrow {}^7F_1$ (iii) $^5D_0 \rightarrow {}^7F_2$ (C_{3i} emissions are noted by *.)

These transitions energies for both samples differ from those reported by Zych et al. in several other studies.[145-147] In the papers published by Zych et al, the energies reported for the $^5D_0 \rightarrow {}^7F_J$ transitions vary among the numerous publications. The authors offer no explanation for these differences. The differences noted between our transition energies and those reported by Zych may arise from the fact our crystallite sizes are approximately three to four times larger, probably due to slight differences in the preparation methods. Difference in the crystallite sizes may induce changes in the crystal field experienced by the Eu^{3+} ion as a larger percentage of the dopant ions would reside on or towards the surface of the nanocrystals resulting in small line shifts between the two samples.

The emission spectra also reveal changes in the relative intensities and linewidths of the $^5D_0 \rightarrow {}^7F_0$, $^7F_1$, $^7F_2$ transitions between the bulk and nanocrystalline samples. The inset of Figure 3.1. clearly shows that the unsplit $^5D_0 \rightarrow {}^7F_0$ line, attributed to Eu^{3+} ions in the C_2 site, in the nanocrystalline sample is significantly broader than in the bulk; indicating a higher disorder of the Eu^{3+} crystalline environment. It is also observed in the nanocrystalline sample that the relative intensity of the $^5D_0 \rightarrow {}^7F_0$ and the hypersensitive $^5D_0 \rightarrow {}^7F_2$ peaks compared to the $^5D_0 \rightarrow {}^7F_1$ peaks are higher than for the bulk. The ratio of the integrate intensities of the $^5D_0 \rightarrow {}^7F_2$ and $^5D_0 \rightarrow {}^7F_1$ transitions under UV excitation:

$$R = \frac{I({}^5\mathrm{D}_0 \rightarrow {}^7\mathrm{F}_2)}{I({}^5\mathrm{D}_0 \rightarrow {}^7\mathrm{F}_1)} \qquad (3.1.)$$

can be considered indicative of the asymmetry of the coordination polyhedron of the Eu^{3+} ion.[155] The values of the asymmetry ratio R are 3.8 and 4.4 for the bulk and nanocrystalline samples respectively. These values are slightly smaller than those observed previously in bulk and nanocrystalline $Y_{1.98}Eu_{0.02}O_3$ prepared by wet chemical synthesis.[100] In the case of $Lu_{1.98}Eu_{0.02}O_3$, the R value is again markedly higher for the nanocrystalline sample, suggesting a more distorted local environment for the Eu^{3+} ion than the corresponding bulk sample as the intensity of the $^5D_0 \rightarrow {}^7F_2$ transition strongly depends on the asymmetry of the Eu^{3+} site.[156] This again confirms that a larger portion of the Eu^{3+} ions reside near or at the surface of the nanocrystals due to their higher surface/volume ratio when compared to the bulk material.

The luminescence spectra of the nanocrystalline and bulk samples in the 570-610 nm region upon 257.25 nm excitation at 78 K are shown in Figure 3.2. When comparing the low temperature spectra of both samples to their corresponding RT spectra several changes are observed. Most obvious is the reduction in the emission linewidths as one reaches 78 K due to a reduction in phonon-electron coupling. Also noticeable are a small wavelength shift in several of the emission peaks with decreasing temperature along with a change in the relative intensities of the 587 nm and 582.5 nm peaks. To illustrate these changes, the luminescence of the nanocrystalline $Lu_2O_3:Eu^{3+}$ 1 mol% at RT and 78 K under UV excitation is shown in Figure 3.3.

Several theoretical and experimental studies[157, 158] have examined how changes in electron-phonon coupling with temperature affect peak positions and widths. The majority of these studies have ignored changes in the crystal structure with temperature since these were assumed to be insignificant in the systems studied. Recently it has been found that changes in the peak positions with decreasing temperature in cubic Eu_2O_3 can be attributed not only to differences in the electron-phonon coupling strength at low

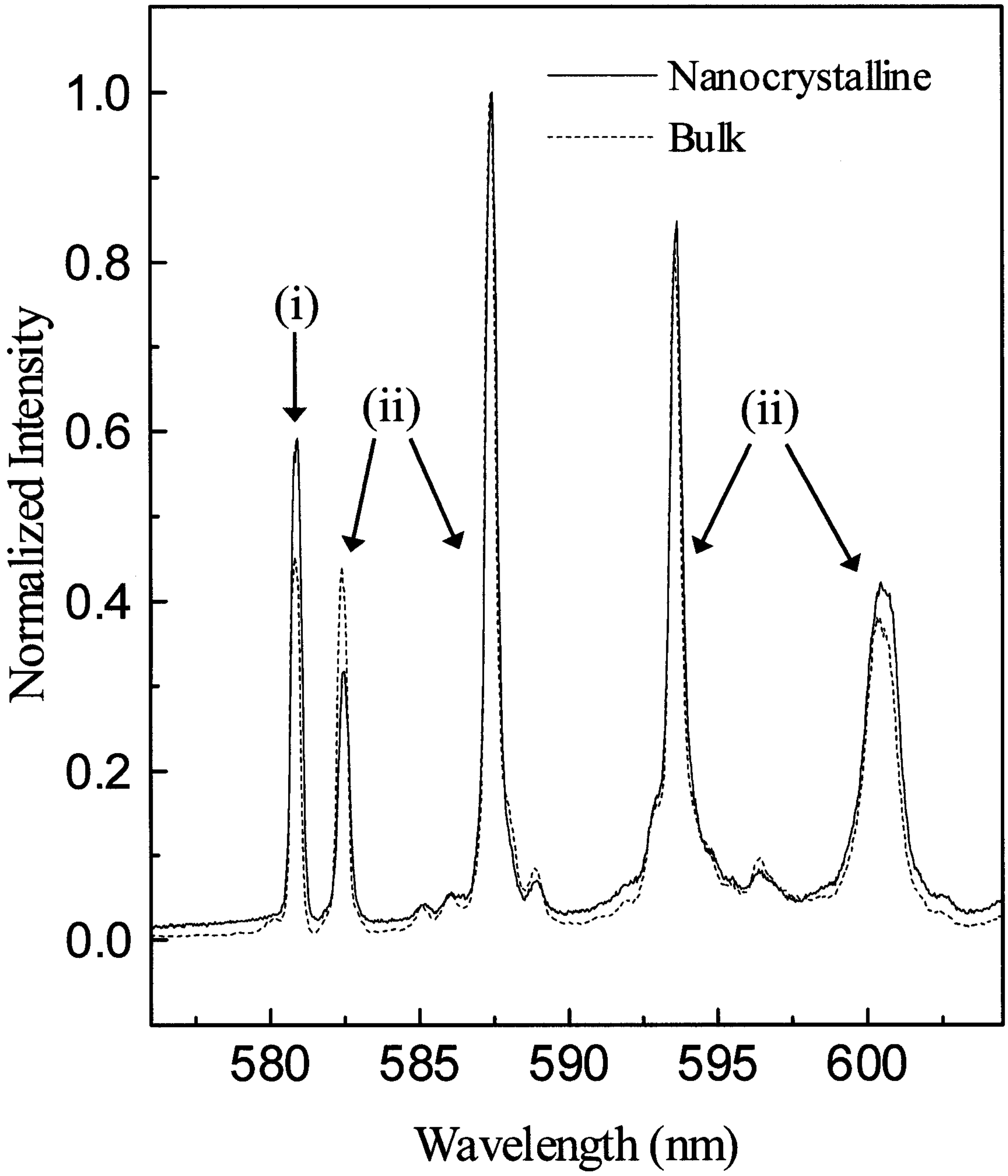

Figure 3.2. Detailed structure of $^5D_0 \rightarrow {}^7F_0, {}^7F_1$ luminescence of bulk and nanocrystalline $Lu_2O_3:Eu^{3+}$ 1 mol% at 78 K (λ_{exc} = 257.25 nm). (i) $^5D_0 \rightarrow {}^7F_0$ (ii) $^5D_0 \rightarrow {}^7F_1$.

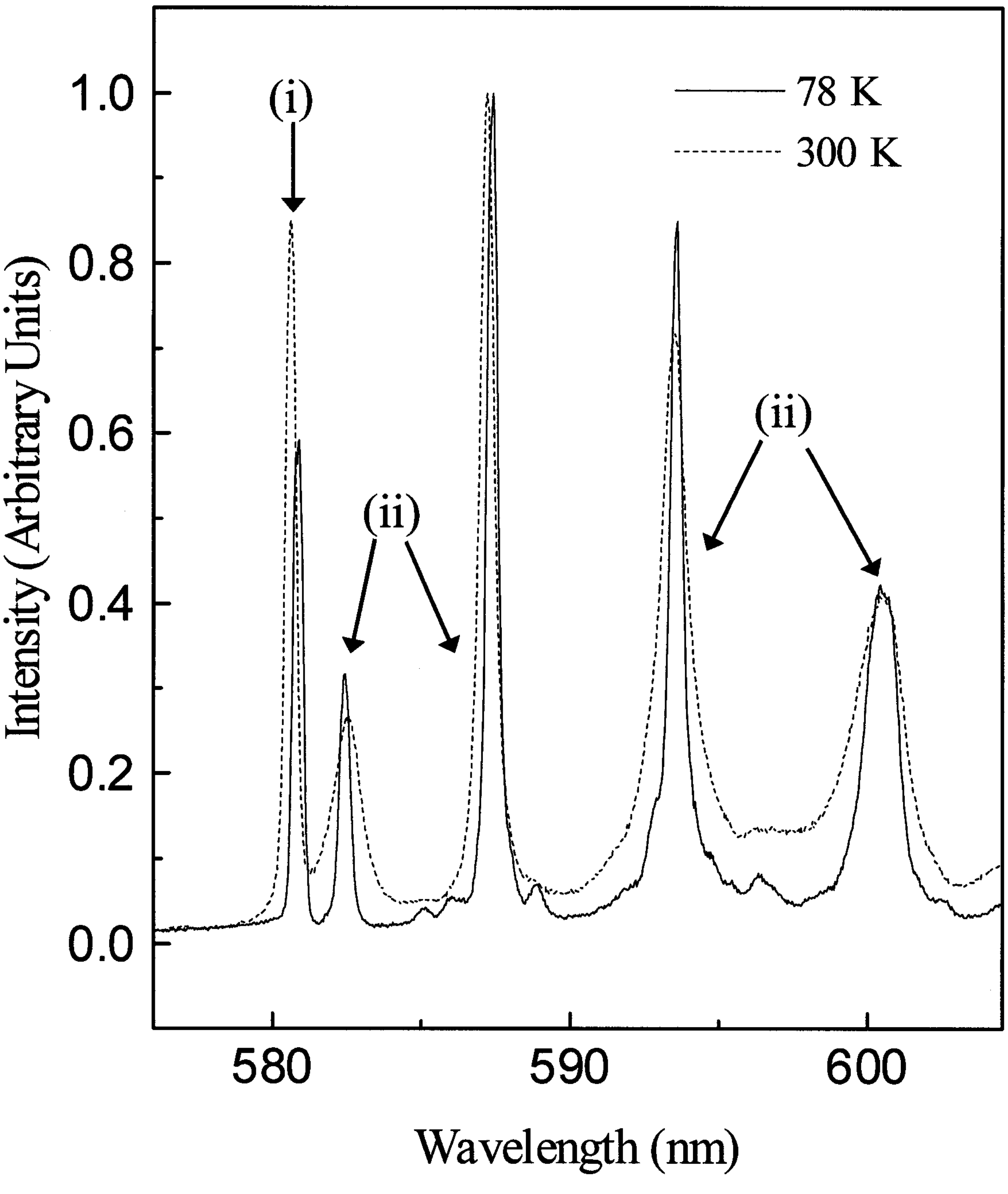

Figure 3.3. Detailed structure of $^5D_0 \rightarrow {}^7F_0, {}^7F_1$ luminescence of nanocrystalline $Lu_2O_3:Eu^{3+}$ 1 mol% at RT and 78 K (λ_{exc} = 257.25 nm). (i) $^5D_0 \rightarrow {}^7F_0$ (ii) $^5D_0 \rightarrow {}^7F_1$.

temperature but also to changes that occur in the crystal structure due to thermal effects.[159] Thus it is safe to assume that the observed Eu^{3+} transition energy changes in the isostructural Lu_2O_3 with temperature are due to changes in both the electron-phonon coupling and crystal structure.

It is also noticeable in Figures 3.1.-3.3. that the 580 nm ($^5D_0 \rightarrow {}^7F_0$) shifts to different extents with temperature changes when comparing the nanocrystalline to bulk samples. It is observed that the line shift is more pronounced in the case of the nanocrystalline sample. As mentioned above the temperature shift of the luminescence is ascribed to a temperature-derived contribution (linked to the electron-phonon coupling) and a volume-derived contribution (linked to the thermal expansion, leading to a change in the equilibrium atomic positions, and therefore in the crystal field).[159] In order to distinguish between these two contributions, one should perform spectroscopic measurements as a function of the pressure and temperature. It is possible that the presence of varying amounts of these contributions between the two types of samples can explain the difference in the degree of line shift with temperature. At this time though, a precise explanation is clearly outside the scope of the paper.

3.4.2. Site-Selective Spectroscopy

Besides examining the luminescence decay times of the Eu^{3+} ions in differing sites, it is possible to elucidate bands which originate from the two different sites by comparing the luminescence spectra under excitation into each separate excitation band. Under excitation into a Eu^{3+} (C_{3i}) transition only C_{3i} lines should appear in the luminescence spectra if one neglects the effects of energy transfer between the two sites. The reverse should also hold true for excitation into Eu^{3+} (C_2) transition. This type of site selective spectroscopy is also a powerful tool for examining the energy transfer mechanism that occurs between the Eu^{3+} ions in the two sites.

Upon excitation at room temperature into the $^7F_0 \rightarrow {}^5D_0$ (C_2) transition, peaks are visible in the orange-red emission spectra of both samples that originate from Eu^{3+} ions in C_2 and C_{3i} sites as seen in Figure 3.4. Emission is observed from the corresponding $^5D_0 \rightarrow {}^7F_1$, $^7F_2$ transitions for the C_2 site. A weak emission line at 582.4 nm [$^5D_0$ (C_{3i}) $\rightarrow {}^7F_1$ (C_{3i})] confirms the presence of a weak energy transfer from $^5D_0$ (C_2) to the $^5D_0$ (C_{3i}) level over the energy gap separating the two states. Nevertheless the majority of the exciting energy is still being released as C_2 type emissions. Likewise, room temperature emission is seen originating from both the C_2 and C_{3i} sites under C_{3i} excitation at 582.4 nm. Emission is observed from the corresponding $^5D_0 \rightarrow {}^7F_1$, $^7F_2$ transitions for the C_2 site along with the presence of a C_{3i} transition at 592.9 nm and a vibronic transition of C_{3i} character at 597 nm. Thus at room temperature there is effective energy transfer from the Eu^{3+} ions in C_{3i} to C_2 sites and also a less efficient energy transfer from C_2 to C_{3i} sites similar to what was observed by Zych for the same material.[153] It is clear though from comparing the spectra obtained under C_{3i} excitation to those obtained under non-selective UV excitation that a higher percentage of the exciting energy is being released as C_{3i} type emissions in the selective excitation case even with the presence of the energy transfer mechanism. This experimental data also indicates that the energy transfer between the C_{3i} and C_2 sites must occur at the $^5D_0$ level even for non-selective UV excitation.

The orange-red emission spectra of the 1 mol% doped bulk and nanocrystalline samples under $^7F_0 \rightarrow {}^5D_0$ (C_2) excitation at 78 K is shown in Figure 3.5. It is evident

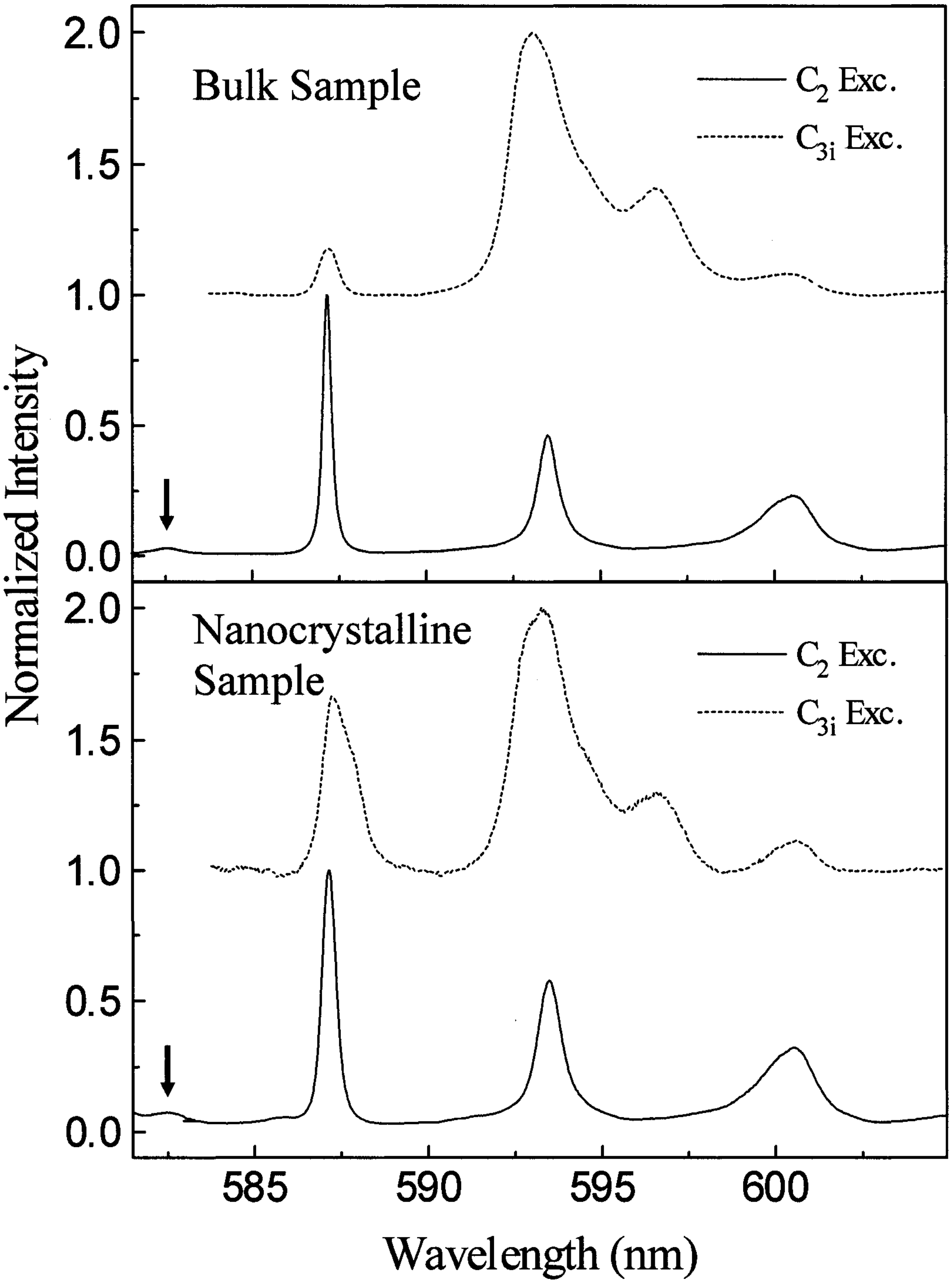

Figure 3.4. Emission spectra $^5D_0 \rightarrow {}^7F_1$ for selective excitation into the $^5D_0$ level (C_2 Exc. – 580.5 nm, C_{3i} Exc. 582.5 nm) of bulk and nanocrystalline $Lu_2O_3:Eu^{3+}$ 1 mol% at RT. Note the presence of weak C_{3i} peak at 582.5 nm in both spectra obtained under C_2 excitation (marked with arrow).

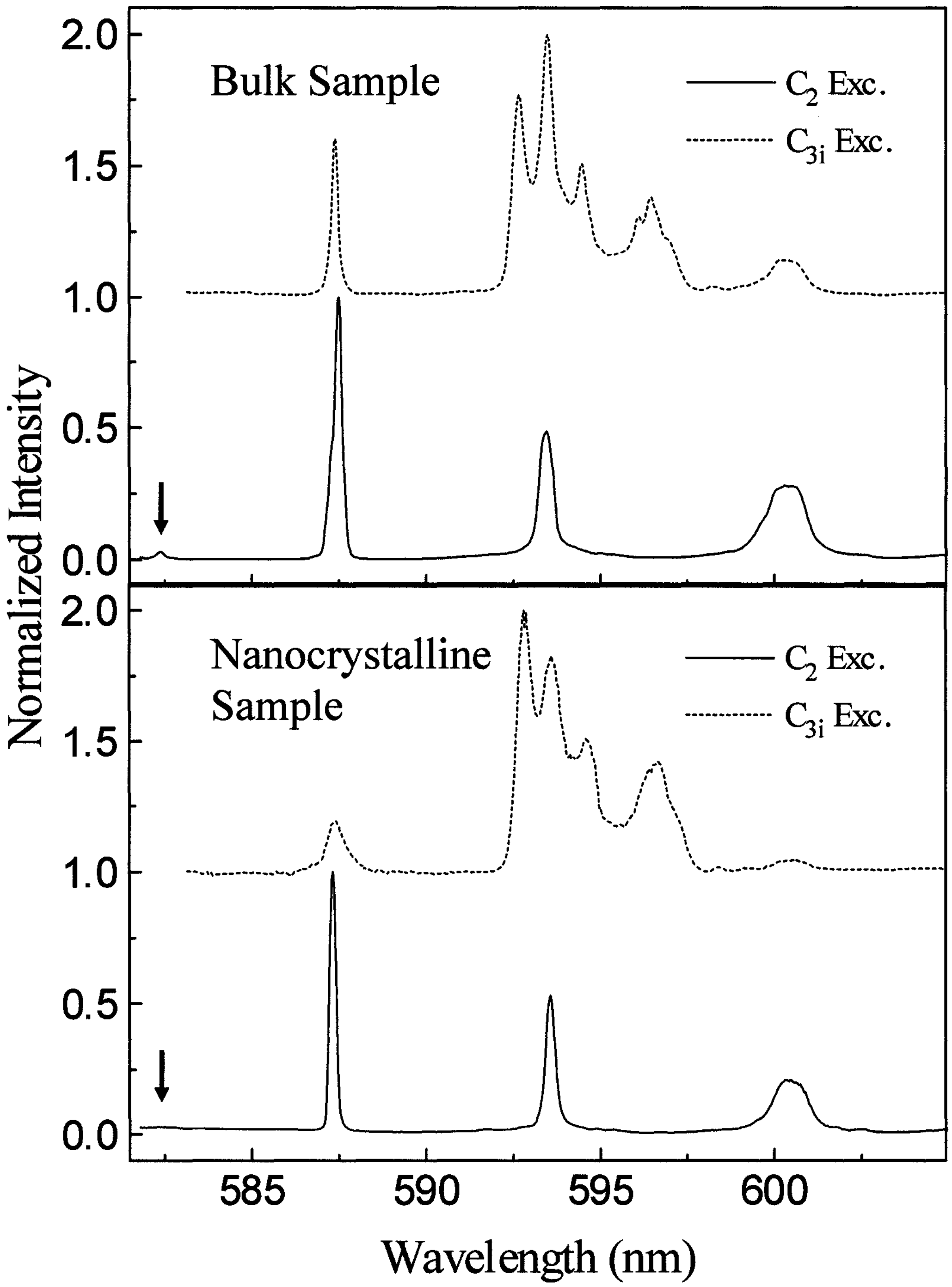

Figure 3.5. Emission spectra $^5D_0 \rightarrow {}^7F_1$ for selective excitation into the $^5D_0$ level (C_2 Exc. – 580.5 nm, C_{3i} Exc. 582.5 nm) of bulk and nanocrystalline Lu_2O_3:Eu^{3+} 1 mol% at 78K. Note the presence of weak C_{3i} peak at 582.5 nm in both spectra obtained under C_2 excitation (marked with arrow).

from the spectra by the absence of C_{3i} emissions that the C_2 to C_{3i} energy transfer process is to a great extent reduced at this temperature as it is a thermally activated process.[147] The spectra now consist only of C_2 type emission lines from the corresponding $^5D_0 \rightarrow {}^7F_1$, $^7F_2$ transitions. The reverse is not true though for $^7F_0 \rightarrow {}^5D_1$ (C_{3i}) excitation at 78 K shown in the same figures. Here C_2 type emission is still observed from the $^5D_0 \rightarrow {}^7F_1$, $^7F_2$ transitions in both the bulk and nanocrystalline samples indicating the C_{3i} to C_2 energy transfer process is effective even at 78 K.

3.4.3. Luminescence Decay Times

Table 3.2. reports the luminescence decay times of the $^5D_0 \rightarrow {}^7F_1$ and $^5D_0 \rightarrow {}^7F_2$ transitions under various excitation wavelengths. All decay curves exhibited single-exponential behaviour unless otherwise stated, similar to what has been reported in the past for these transitions in bulk and nanocrystalline Lu_2O_3 with identical doping levels.[145, 153] On examining the values of the luminescence decay times of the nanocrystalline and bulk samples under UV excitation one notices a lengthening of the decay time in the nanocrystalline sample, for both the room temperature and 78 K measurements. This behaviour has been explained by Meltzer et al.[11] on the basis of changes in the refractive index of the surrounding medium of the Eu^{3+} ion as one goes to the nanometer size range.

The radiative lifetime of electric dipole transitions of an ion embedded in a medium may be expressed by the formula[160]

$$\tau_R \sim \frac{1}{f(\mathrm{ED})} \frac{\lambda_0^2}{\left[\frac{1}{3}\left(n^2+2\right)\right]^2 n} \qquad (3.2.)$$

where f(ED) is the oscillator strength for the electric dipole transition, λ_0 is the wavelength in vacuum and n is the refractive index of the medium. An analogous formula can be found for magnetic dipole transitions[160]

$$\tau_R \sim \frac{1}{f(\mathrm{MD})}\frac{\lambda_0^2}{n^3} \tag{3.3.}$$

where f(MD) is the oscillator strength for the magnetic dipole transition, λ_0 is the wavelength in vacuum and n is the refractive index of the medium. It was observed in monoclinic $Y_2O_3:Eu^{3+}$ that the radiative lifetime of an electronic transition of an ion embedded in a medium is correlated with an effective refractive index n_{eff}, which is a function of the refractive index of yttria and the fraction of space occupied by the nanoparticles surrounded by the media with refractive index n_{med}.[11] The effective refractive index is given by

$$n_{\mathrm{eff}}(x) = x \cdot n_{\mathrm{Lu_2O_3}} + (1 - x) \cdot n_{\mathrm{med}} \tag{3.4.}$$

where x is the “filling factor” showing what fraction of space is occupied by the nanoparticles. One may replace n by n_{eff} when the average size of the particles in questions much smaller than the wavelength of light, as is the case for the nanocrystalline lutetia under investigation.

We have performed similar experiments on the nanocrystalline Eu^{3+} doped Lu_2O_3 and have found comparable results. In Figure 3.6. the lifetime at room temperature of the $^5D_0$ state of Eu^{3+} for both the C_2 and C_{3i} sites are plotted versus the refractive index of the media (n_{med}) in which the nanoparticles are dispersed. The experimental data for both the C_2 and C_{3i} sites have been used for fitting with Eq. (3.2.) and Eq. (3.3.) respectively, using x as an adjustable parameter. In both the C_2 and C_{3i} sites, it was found that a filling

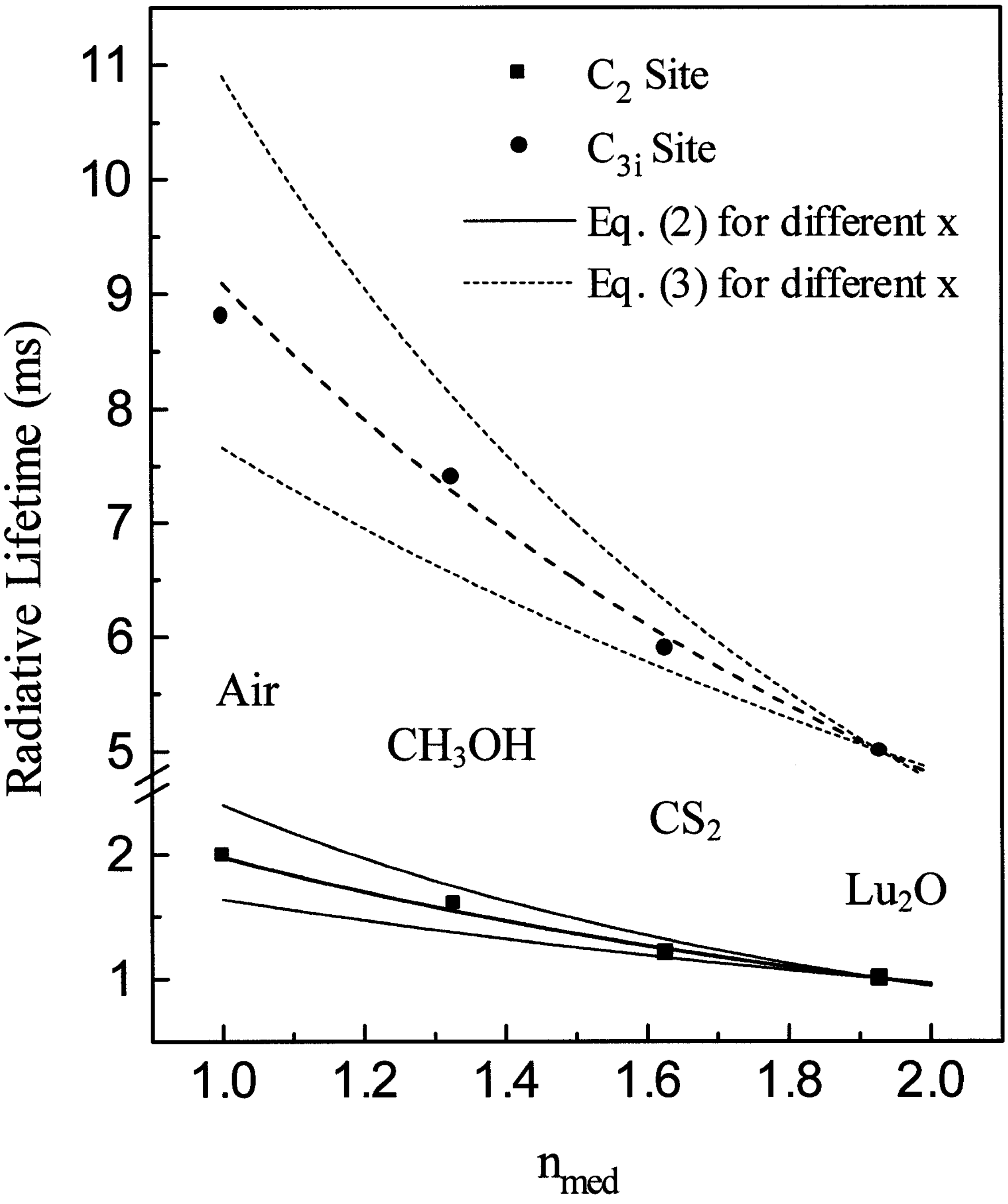

Figure 3.6. Dependence of the $^5D_0$ lifetime for the Eu^{3+} C_2 and C_{3i} sites on the index of refraction of the media n_{med} at T = 298 K.

factor of 0.625 gave a reasonable fit (see Figure 3.6.). Results using $x = 0.525$ and 0.725 are shown by the other curves. Thus as the refractive index of lutetia[161] is 1.93, a lengthening of the decay times of the electronic levels of Eu^{3+} for the nanoparticles in air is expected, in agreement with the present results.

This is the first time that this procedure has been performed for the Eu^{3+} C_{3i} decay. The fact that the same filling factor was determined for both the C_2 and C_{3i} decays is a good indication that this fitting procedure is a valid one. To validate the results further, a corresponding bulk sample was ground with a mortar and pestle and placed immersed in the various solvents utilized. No changes in the bulk C_2 or C_{3i} decay time were observed under these conditions.

At 78 K, the lifetime of the $^5D_0$ (C_2) level under UV excitation was observed to increases from 1.0 ms to 1.1 ms for the bulk sample. A similar increase from 2.0 ms to 2.3 ms was also found in the nanocrystalline sample. A more striking increase was observed in the lifetime of the $^5D_0$ (C_{3i}) level at 78 K; where the lifetimes of both samples were approximately double of what was observed at room temperature (Table 3.2.). We propose that the lengthening of the lifetime of these levels are primarily due to the reduction of both the C_2 to C_{3i} and C_{3i} to C_2 energy transfer mechanisms between Eu^{3+} ions at low temperature. Since the major pathway for non-radiative relaxation for Eu^{3+} in Y_2O_3 is energy transfer among the Eu^{3+} ions to a quenching center, if the energy transfer process is less efficient at low temperatures then these non-radiative processes will be reduced and the lifetime of the level will increase. In the case of the $^5D_0$ (C_{3i}) level at RT the lifetime is shortened by energy-transfer to Eu^{3+} ions residing in C_2 sites which possess significantly shorter lifetime. At 78 K the probability for the downward energy-transfer from the C_{3i} to C_2 site is decreased; reducing this pathway for relaxation and resulting in the significant increase of the $^5D_0$ (C_{3i}) lifetime.

Table 3.2. $^5D_0$ luminescence decay times for bulk and nanocrystalline $Lu_2O_3:Eu^{3+}$ 1 mol% at RT and 78 K (λ_{exc} = 257.25 nm).

Sample	Temperature (K)	Emission Wavelength (nm)	Emitting Level and Site Symmetry	Decay Time (ms)
Bulk	RT	611	$^5D_0$ (C_2)	1.0
Bulk	RT	582.4	$^5D_0$ (C_{3i})	4.4
Bulk	78	611	$^5D_0$ (C_2)	1.1
Bulk	78	582.4	$^5D_0$ (C_{3i})	6.0
Nano	RT	611	$^5D_0$ (C_2)	2.0
Nano	RT	582.4	$^5D_0$ (C_{3i})	8.7
Nano	78	611	$^5D_0$ (C_2)	2.3
Nano	78	582.4	$^5D_0$ (C_{3i})	17

3.4.4. Judd-Ofelt Parameters

To gain more insight into the possible structural changes surrounding the Eu^{3+} ion between the two samples, the experimental intensity parameters Ω_2 and Ω_4 were calculated from the emission spectra using a technique developed by Porcher [162] and subsequently used by others.[163] This technique takes advantage of the fact that the intensities of the $^5D_0 \rightarrow {}^7F_2$, $^5D_0 \rightarrow {}^7F_4$ and $^5D_0 \rightarrow {}^7F_6$ transitions are solely dependent on the Ω_2, Ω_4 and Ω_6 parameters respectively. Also, the $^5D_0 \rightarrow {}^7F_1$ transition possesses solely magnetic dipole character while the other $^5D_0 \rightarrow {}^7F_J$ transitions are purely electric dipole.

It is possible to express the spontaneous emission intensity for an $i \rightarrow k$ transition as[164]

$$I(i,k) = \hbar\omega_{ik}\, A(i,k)N(i) \qquad (3.5.)$$

where $\hbar\omega_{ik}$ is the transition energy, $N(i)$ is the population of the emitting state and $A(i,k)$ is the spontaneous emission probability for the $i \rightarrow k$ transition. In the case of the $^5D_0 \rightarrow {}^7F_J$ emission transitions of the Eu^{3+} ion, the value of $A(^5D_0, {}^7F_J)$ can be determined from the equation[165]

$$A(^5D_0, {}^5F_J) = \frac{4e^2\omega^3}{3\hbar c^3}\chi\sum_{\lambda}\Omega_\lambda \left\langle {}^7\mathrm{F}_J \middle\| U^{(\lambda)} \middle\| {}^5\mathrm{D}_0 \right\rangle^2 \qquad (3.6.)$$

where $\chi = n_0(n_0^2 + 2)^2 / 9$ is the Lorentz local field correction and n_0 is the index of refraction of the host. For the nanocrystalline sample, we replace n_0 with the n_{eff} refractive index determined in the previous section. The reduced matrix elements were taken from Carnall et al.[57]

The calculated values of the Judd-Ofelt parameters are given in Table 3.3. for both the nanocrystalline and bulk samples. The Ω_λ parameters for the lanthanide ion are noticeably higher for the nanocrystalline sample than in the bulk. This behaviour could be due to the fact that for the nanocrystalline host a higher fraction of the Eu^{3+} ions is on the surface of the particles with respect to the bulk one and therefore the average crystal field experienced by the ions in the nanoparticles is different with respect to that for the bulk sample. Moreover, it has been shown that adsorbed CO_2 and water are present as contaminants at the surface of the Lu_2O_3 nanoparticles[16] and therefore they could contribute to vary the crystal field experienced by the Eu^{3+} ion. In particular, changes in the Ω_2 value can be related to changes in the structural environment around the rare earth ion due to the hypersensitivity of the $^5D_0 \rightarrow {}^7F_2$ transition. The larger Ω_2 parameter in the nanocrystalline sample is a good indication that the symmetry of the Eu^{3+} sites is distorted compared to the bulk sample due to the samples small size.

Table 3.3. Ω_λ, Judd-Ofelt intensity parameters for the nanocrystalline and bulk $Lu_2O_3:Eu^{3+}$ 1 mol%. R_{02}: ratio between the emission intensities of the $^5D_0 \rightarrow {}^7F_0$ and $^5D_0 \rightarrow {}^7F_2$ transitions.

Sample	**Ω_2 (10^{-20} cm^2)**	**Ω_4 (10^{-20} cm^2)**	**R_{02}**
Bulk	6.14	1.71	0.019
Nanocrystalline	9.07	2.60	0.025

Another useful value to examine is the ratio of the emission intensities of the $^5D_0 \rightarrow {}^7F_0$ to $^5D_0 \rightarrow {}^7F_2$ transitions R_{02}. This parameter can give information about the J-mixing effect related with the $^5D_0 \rightarrow {}^7F_0$ transition.[163] As with the Ω_k values, the R_{02} ratio was found to be higher for the nanocrystalline sample reflecting a larger J-mixing. This indicates that in the nanocrystalline sample the structure environment around the Eu^{3+} ions is of higher complexity compared to the bulk.

3.5. CONCLUSIONS

Emission spectra and lifetimes of the excited states of the nanocrystal samples were found to differ significantly from those of the bulk. Judd-Ofelt intensity parameters calculated from the emission spectra of the samples indicate that the Eu^{3+} sites in the nanocrystalline sample are more disordered compared to the bulk sample. A higher R_{02} ratio confirms that the Eu^{3+} environment in the nanocrystalline sample is more complex than in the bulk. The longer lifetimes for the $^5D_0$ excited state were successfully attributed to a modification in the refractive index for the nanocrystalline material. By fitting the decay curves for both the C_2 and C_{3i} sites, it was found that the nanocrystals have a filling factor of 0.625.

3.6. AUTHOR'S NOTES AND SIGNIFICANCE OF THIS PAPER

This publication on Eu^{3+} doped Lu_2O_3 is a groundbreaking publication in the field of nanocrystal research. In this work, we applied several techniques from the literature that allowed for the determination of Judd-Ofelt intensity parameters for the Eu^{3+} transitions in this material. Intensity parameters are normally calculated for transparent glasses and crystals via the absorption spectra of the materials. Since the materials in question were polycrystalline, we utilized the relative emission intensities of the various Eu^{3+} transitions to arrive at the intensity parameters. This was the first instance in the literature of the utilization of this technique on a Eu^{3+} doped nanocrystalline material.

The subsequent chapter examines the spectroscopy and upconversion studies of Ho^{3+} doped $Gd_3Ga_5O_{12}$ (GGG) nanocrystals. Though we were able to observe upconversion in lanthanide doped sesquoxide materials the efficiencies of these materials were significantly decreased by adsorbed CO_3^{2-} and OH^- ions. We decided to move on to GGG as a host material as it demonstrated considerably less surface contamination due to the afformentioned ions derived from atmospheric molecules. This resulted in a substantial increase in the observed upconversion efficiencies in the Ho^{3+} doped materials. In fact, this was the first report in the literature of efficient Ho^{3+} upconversion in a discrete oxide-based nanopowder.

Chapter 4

Investigation of the Upconversion Processes in Nanocrystalline $Gd_3Ga_5O_{12}:Ho^{3+}$

Published as:

J. C. Boyer, F. Vetrone, J. A. Capobianco, A. Speghini, M. Zambelli and M. Bettinelli

Journal of Luminescence **2004**, *106*, 263-268.

4.1. ABSTRACT

Intense upconversion luminescence is reported for the first time in a Ho^{3+} doped nanocrystalline material. Anti-Stokes blue and green luminescence was noted in nanocrystalline $Gd_3Ga_5O_{12}$:Ho^{3+} after excitation into the $^5F_5$ level with 647 nm radiation. Excitation at 756 nm into the $^5I_4$ level resulted in green and red anti-Stokes emission. In both cases, an excited state adsorption (ESA) mechanism is thought responsible for the observed upconversion luminescence. The temporal dependence of the upconverted luminescence for the two excitation wavelengths revealed that the $^5I_7$ level was the intermediate level in both two-photon processes.

4.2. INTRODUCTION

The past decade has seen a proliferation in the number of papers published on lanthanide doped nanocrystalline phosphors due to their different luminescence properties and excited state kinetics when compared to micrometer counterparts.[121, 122] These unique properties have generated interest in these materials for possible use in Plasma Display Panels (PDPs), Field Emission Displays (FEDs) and Cathode Ray Tubes (CRTs).[45] While numerous studies[85, 86] have focused on these applications, examining the luminescence generated by exciting with UV light or electrons, very few have examined the upconversion phenomenon in nanocrystalline materials. Upconversion is the generation of visible or UV light from lower energy radiation, usually NIR or IR, through the use of transition metal, lanthanide or actinide ions doped into a solid state host. Much of the interest in upconverting materials is due to their potential applications as IR sensitive phosphors or in upconversion lasers.[71]

The $Gd_3Ga_5O_{12}$ (GGG) crystal belongs to the cubic crystalline system with space group *Ia*3*d*.[91, 166] The Gd^{3+} ions occupy 24(c) dodecahedral (distorted cube) sites in the lattice, while the Ga^{3+} ions are located in the 16(a) and 24(d) sites which represent octahedral and tetrahedral coordination. The O^{2-} ions occupy the 96(h) sites with each one being a member of two dodecahedra, one octahedron and one tetrahedron. The garnet structure can be viewed as interconnected dodecahedra, octahedra and tetrahedra with shared atoms at the corners of the polyhedra. The doping lanthanide ions enter into the Gd^{3+} sites which possess D_2 symmetry.

The luminescent properties and intensity parameters of single crystal $Gd_3Ga_5O_{12}:Ho^{3+}$ have been examined in detail previously.[167] Recently, the upconversion of NIR to visible light,[168] and the energy transfer[169] involved in this process, have been investigated in $Gd_3Ga_5O_{12}:Ho^{3+}$ co-doped with Yb^{3+}. The effect of Tm^{3+} on both the upconversion processes and as a sensitizer for the 2 μm laser emission in $Gd_3Ga_5O_{12}:Ho^{3+}$ garnet co-doped with Yb^{3+} has also been examined in great detail.[93-98] To date, no investigation of the luminescent or upconversion properties of $Gd_3Ga_5O_{12}:Ho^{3+}$ in nanocrystalline form has been performed. In this letter we examine two upconversion processes, one under 647 nm excitation and another with 756 nm excitation, in $Gd_3Ga_5O_{12}$ nanocrystals doped with 1 mol% Ho^{3+}.

4.3. EXPERIMENTAL

The $Gd_3Ga_5O_{12}$ nanocrystals doped with 1 mol% Ho^{3+} were prepared using a solution combustion (propellant) synthesis procedure. This process involves the exothermic reaction between metal nitrates (oxidiser) and an organic fuel, such as urea, glycine or carbohydrazide. An aqueous solution containing appropriate quantities of carbohydrazide $(NH_2NH)_2CO$ (Aldrich, 98%), $Gd(NO_3)_3{\cdot}6H_2O$ (Aldrich, 99.99%), $Ga(NO_3)_3{\cdot}H_2O$ (Aldrich, 99.999%) and $Ho(NO_3)_3{\cdot}6H_2O$ (Aldrich, 99.9%) was prepared. A carbohydrazide-to-metal nitrate molar ratio of 2.5 was employed. The precursor solution was heated with a Bunsen flame and after the evaporation of the solvent, the auto combustion process occurs with the evolution of brown fumes resulting in the formation of a very porous and voluminous mass of powder. The proposed stoichiometric synthesis reaction is:

$$3(1-x)Gd(NO_3)_3 + 5Ga(NO_3)_3 + 3xHo(NO_3)_3 + 3(NH_2NH)_2CO \rightarrow$$

$$(Gd_{1-x}Ho_x)_3Ga_5O_{12} + 24NO_2 + 6N_2 + 3CO_2 + 9H_2O$$

The resultant powder of the combustion reaction was fired for 2 hours at 700 °C in order to decompose any residual carbohydrazide and nitrate ions. All nanocrystalline samples were kept in air without any further precautions.

Stokes emission spectra were measured by exciting at 457.9 nm using a Coherent Sabre Innova, 20 W argon laser. The anti-Stokes luminescence spectra were obtained by exciting either at 756 nm using a Spectra-Physics Model 3900 Titanium Sapphire laser or at 647 nm using a Spectra-Physics 375 dye-laser operating with DCM, both were pumped by the 514.5 nm line of the argon ion laser. The visible emissions were then collected and dispersed using a Jarrell-Ash 1-meter Czerny Turner double monochromator. The emissions were monitored with a thermoelectrically cooled Hamamatsu R943-02 photomultiplier tube. The photomultiplier signals were aquired using a preamplifier model SR440 Stanford Research Systems and a gated photon counter model SR400 Stanford Research Systems data acquisition system. The signal was recorded under computer control using Stanford SR465 data acquisition software. Luminescence decay curves were measured by modulating the excitation light with a chopper (SR540 Stanford Research Systems). They were recorded using the same gated photon counter mentioned above. The temporal dependence of the upconverted emission was obtained by modulating the excitation beam at 20 Hz with the chopper and recorded the photomultiplier tube output using a digital oscilloscope (Tektronix TDS 520A). All experiments were performed at room temperature (298 K).

4.4. RESULTS AND DISCUSSION

Wide angle powder X-ray diffraction has confirmed that the nanocrystalline $Gd_3Ga_5O_{12}$:Ho^{3+} sample under investigation contains $Gd_3Ga_5O_{12}$ and that no important contamination from other phases is present. The broadening of the diffraction peaks indicates that the particle sizes are in the 10 nm range. A detailed investigation of the structure and morphology of these materials is presently under way.[170]

The luminescence emission spectra of the sample excited at 457.9 nm is shown in Figure 4.1. Three emission bands arising from transitions within the *4f*-*4f* levels of the Ho^{3+} ion are observed in the visible portion of the spectrum. All observed emission bands demonstrated a linear power dependence indicating they all originate from Stokes emissions. A weak blue emission attributed to the $^5F_3 \rightarrow {}^5I_8$ transition was observed between 480-500 nm. An intense yellow-green emission between 530-570 nm was detected and assigned to the transition from the thermalized $^5F_4$ and $^5S_2$ states to the $^5I_8$ ground state. A red emission was observed between 635-670 nm originating from the $^5F_5 \rightarrow {}^5I_8$ transition. A NIR emission between 740-770 nm (not shown) corresponding to the $(^5F_5,{}^5S_2)\rightarrow{}^5I_7$ transition was also observed. The emission spectrum obtained for the nanocrystalline material is very similar to what has been reported for single crystal $Gd_3Ga_5O_{12}$ doped with Ho^{3+} and Yb^{3+},[168] indicating that the crystal field acting on the ions is not significantly affected by the nanocrystals' small size.

Figure 4.1. shows the upconversion (anti-Stokes) luminescence of the $Gd_3Ga_5O_{12}$: Ho^{3+} nanocrystals after excitation into the $^5F_5$ level with 647 nm radiation. Anti-Stokes emission was observed corresponding to the blue $^5F_3 \rightarrow {}^5I_8$ and the green $(^5F_4, {}^5S_2) \rightarrow {}^5I_8$ transitions. As in the Stokes emission spectrum obtain under 457.9 nm excitation, the

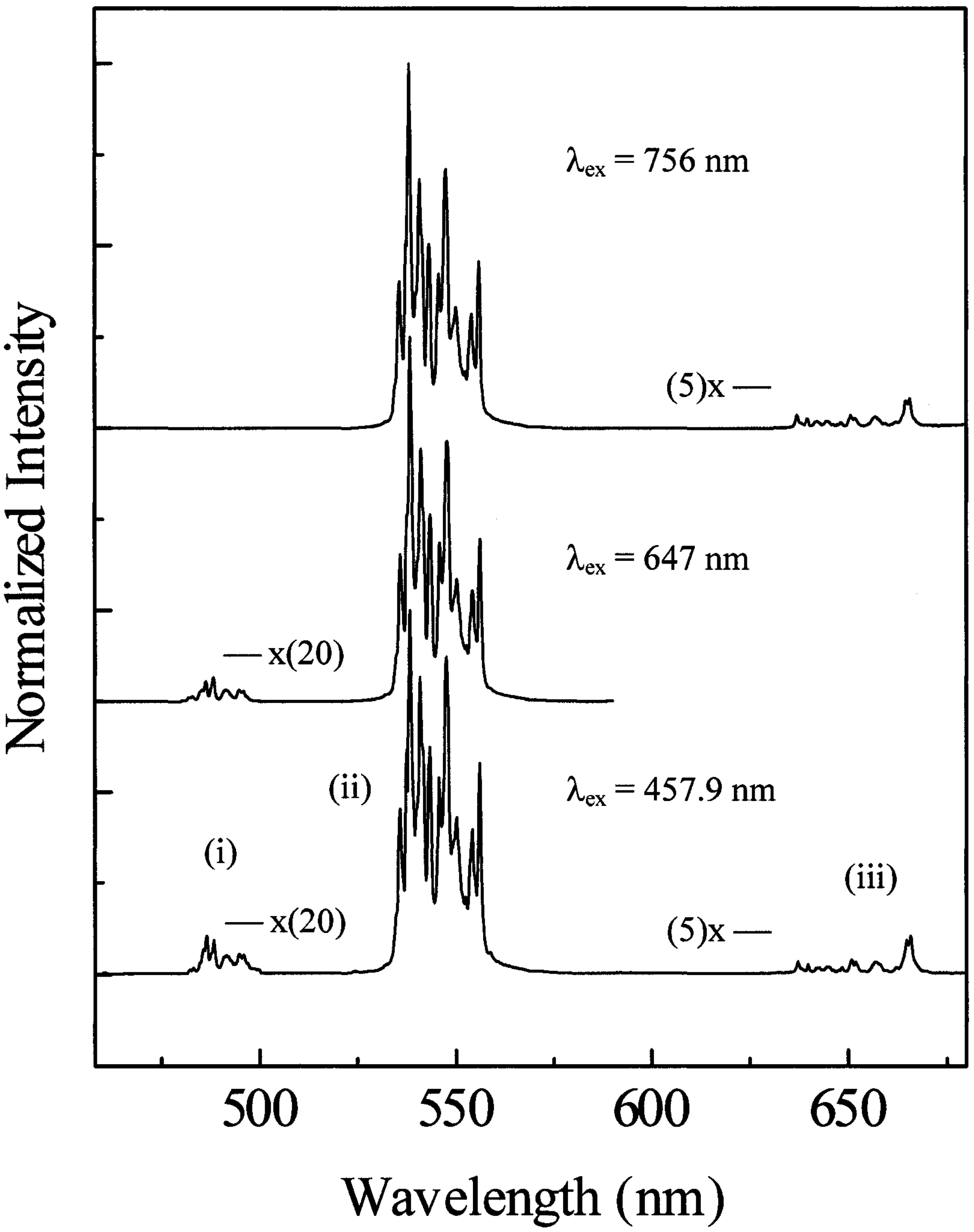

Figure 4.1. Room temperature upconverted luminescence of nanocrystalline $Gd_3Ga_5O_{12}$: Ho^{3+} upon excitation at 647 nm or 756 nm. Room temperature emission spectrum under λex = 457.9 nm is also shown for comparative purposes. (i) $^5F_3 \rightarrow {}^5I_8$ (ii) $(^5F_4, {}^5S_2) \rightarrow {}^5I_8$ (iii) $^5F_5 \rightarrow {}^5I_8$.

green ($^5F_4$, $^5S_2$) → $^5I_8$ emission was found to be dominant over all other emissions. The upconversion luminescence intensity I_0 is related to the pump intensity I_i via the formula $I_0 \alpha I_i^n$, where n is the number of pump photons required to populate the emitting state.[136] In order to determine the number of photons responsible for the upconversion mechanism, the intensity of the green ($^5F_4$, $^5S_2$) → $^5I_8$ luminescence was measured as a function of the 647 nm excitation intensity (Figure 4.2.). A straight line fit of the resulting plot of ln(I_i) versus ln(I_0) resulted in a slope of 1.8 indicating a two-photon upconversion process is present.

The ratio of the blue to green emission was found to approximately 1:400 in both the Stokes and anti-Stokes emission spectra. The luminescence decay curve of the ($^5F_4$, $^5S_2$) → $^5I_8$ transition by exciting at 647 nm was measured and fitted with a single exponential function. The decay time of the ($^5F_4$, $^5S_2$) → $^5I_8$ transition was found to be 49 μs, which is identical to that obtained under 457.9 nm excitation. For this reason, there is no definite indication that an energy transfer upconversion process (ETU) is dominant.[171] A photon avalanche upconversion mechanism is discounted as no inflection in the graph of ln(I_i) versus ln(I_0) was observed. Based on these observations, it is reasonable to assume that an excited state absorption (ESA) upconversion process is predominantly responsible for the anti-Stokes emission.

Excited state absorption (ESA) processes from lower lying energy levels in Ho^{3+} doped crystals and glasses has been proposed by many authors.[98, 172] Two likely excited state absorptions occur from the $^5I_6$ and $^5I_7$ levels. To determine which was responsible for the upconversion luminescence we examined the temporal evolution of the green luminescence. We observed a risetime value of 5.1 ms which is closer to the lifetime of

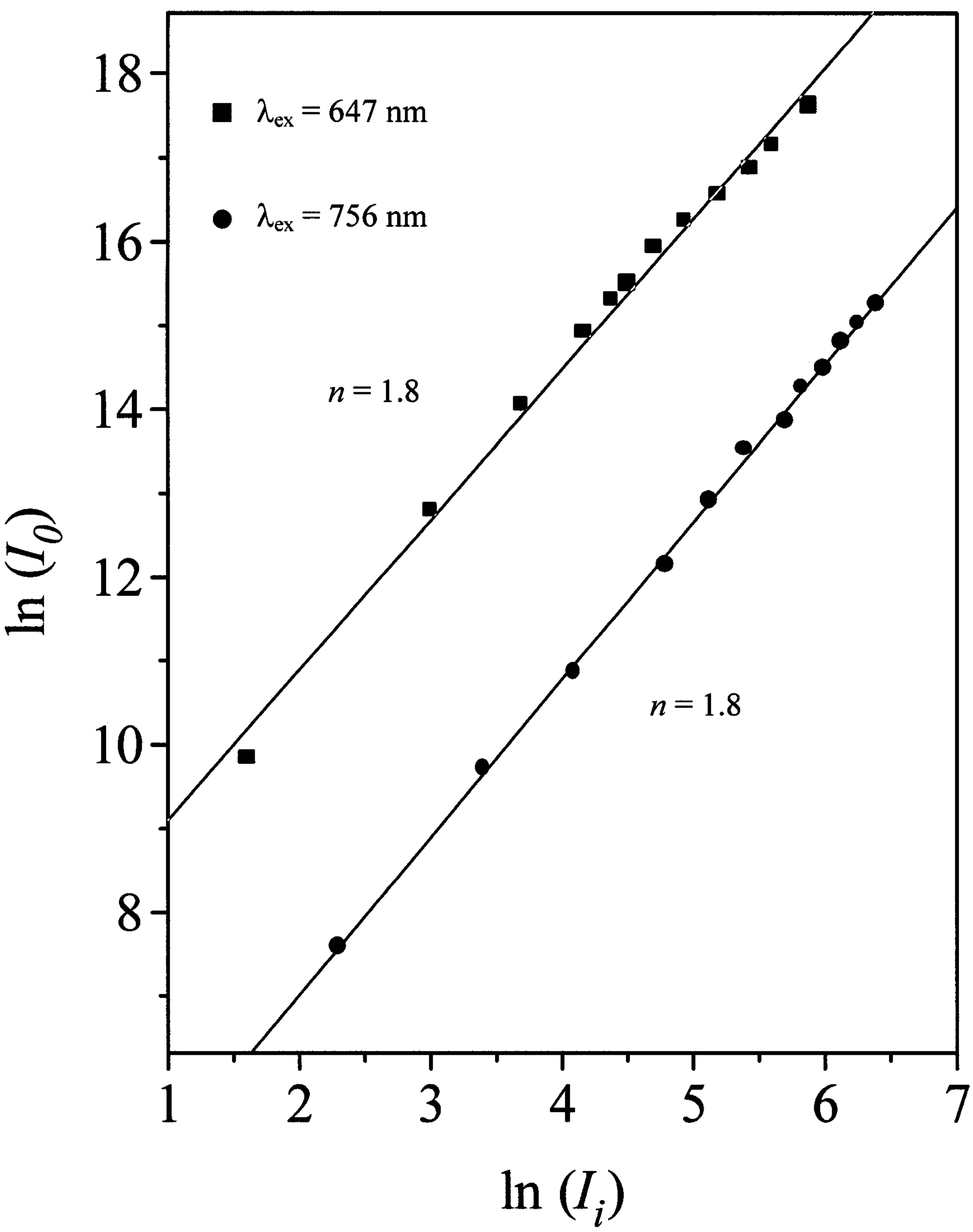

Figure 4.2. Room temperature power dependence of the upconverted ($^5F_4$, $^5S_2$) → $^5I_8$ luminescence intensity for the nanocrystalline $Gd_3Ga_5O_{12}$: Ho^{3+} observed with 647 nm and 756 nm excitation.

10 ms for the $^5I_7$ level rather than the $^5I_6$ lifetime of 550 μs found in the single crystal $Gd_3Ga_5O_{12}$: Ho^{3+}.[98] Based on these results we propose that the primary mechanism by which the $^5F_3$ and ($^5F_4$, $^5S_2$) levels are populated (Figure 4.3.) is as follows. The 647 nm laser light initially populates the $^5F_5$ level of the Ho^{3+} ion, which then non-radiatively decays down to the $^5I_7$ level. A second absorbed 647 nm photon through an ESA process ($^5I_7 \rightarrow {}^5F_3$) brings the ion to the $^5F_3$ level. The ion then emits through the $^5F_3 \rightarrow {}^5I_8$ transition or can non-radiatively decay to the lower lying levels and the ($^5F_4$, $^5S_2$) $\rightarrow$ $^5I_8$ transition occurs. Since the $^5I_7$ level, which is responsible for feeding the $^5F_4$ and $^5S_2$ levels in the upconversion process, is long lived[98] the identity of the decay time of the emission from ($^5F_4$, $^5S_2$), following 457.9 and 647 nm excitation, confirms that an ETU mechanism is not important in the upconversion process.

The anti-Stokes green emission was found to be very powerful with luminescence being visible with the naked eye with only a few milliwatts of excitation power. This is in stark comparison to a previous study on Ho^{3+} doped nanocrystalline Y_2O_3 prepared via a similar propellant synthesis where the same upconversion process was noted to be far less efficient.[13] The lower upconverted emission intensity for the Y_2O_3:Ho^{3+} nanocrystalline sample was attributed to an increase of multiphonon relaxations of excited levels caused by the presence of carbonate and hydroxide ions on the surface of the nanocrystals. The presence of carbonate (~1500 cm^{-1}) and hydroxide (~3350 cm^{-1}) phonons can easily depopulate via multiphonon relaxation the $^5I_7$ intermediate level involved in the excited state absorption (ESA) upconversion mechanism, thereby reducing its efficiency. In contrast, the MIR spectrum of $Gd_3Ga_5O_{12}$ nanocrystals synthesised via the combustion reaction described, exhibited a considerable reduction

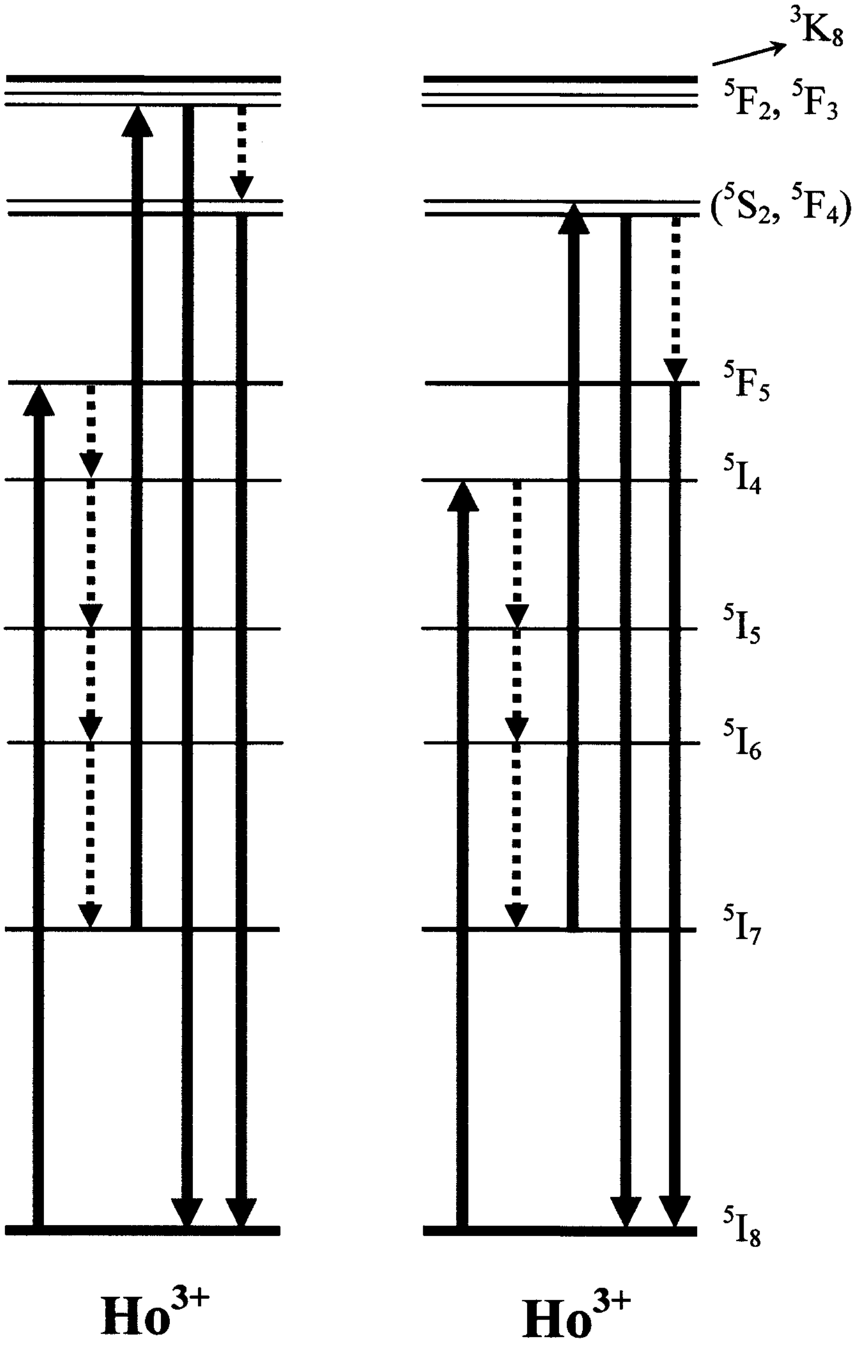

Figure 4.3. Principal ESA upconversion mechanisms for 647 nm excitation (left) and 756 nm excitation (right) in nanocrystalline $Gd_3Ga_5O_{12}$: Ho^{3+}.

in the intensity of the bands attributed to the carbonate and hydroxide ions compared to those of the Y_2O_3 nanocrystals.[173] Therefore, the lower concentration of adsorbed contaminant species on the surface of the $Gd_3Ga_5O_{12}:Ho^{3+}$ nanocrystals will lead to higher luminescence and upconversion efficiencies compared to nanocrystalline Y_2O_3: Ho^{3+}.

Upon excitation of the $Gd_3Ga_5O_{12}:Ho^{3+}$ nanocrystals with 756 nm radiation into the $^5I_4$ level, anti-Stokes emissions corresponding to the ($^5F_4$, $^5S_2$) → $^5I_8$ and $^5F_5$ → $^5I_8$ transitions were observed (Figure 4.1.). As seen in Figure 4.2., the ($^5F_4$, $^5S_2$) → $^5I_8$ luminescence was found to exhibit a nearly quadratic dependence ($n = 1.8$) on the laser power indicating that two photons were involved in the upconversion mechanism. Again, no changes in the relative intensities of the emission peaks were observed between the upconverted and Stokes emission spectra.

An excited state absorption (ESA) upconversion mechanism was again thought responsible for the upconversion luminescence. The decay time of the ($^5F_4$, $^5S_2$) state under 756 nm excitation was found to be 49 μs; similar to what was observed under excitation at 457.9 nm. Similar to the case of excitation into the $^5F_5$ level ($\lambda_{exc} = 647$ nm), the temporal evolution of the green luminescence indicated a rise time of 5.1 ms identified as the lifetime of the $^5I_7$ level, as described above. Based on these observations we propose the following upconversion mechanism by which the ($^5F_4$, $^5S_2$) and $^5F_5$ levels are populated (Figure 4.3.). The first 756 nm photon populates the $^5I_4$ level of the Ho^{3+} ion through a ground state absorption (GSA), which then non-radiatively decays to the $^5I_7$ level. A second laser photon through an excited state absorption (ESA) process then populates the ($^5F_4$, $^5S_2$) levels. Green emission then occurs corresponding to the ($^5F_4$, $^5S_2$)

$\rightarrow {}^5I_8$ transition or alternatively the ion can non-radiatively decay to the lower lying energy levels and the red emission ${}^5F_5 \rightarrow {}^5I_8$ transition is observed.

4.5. CONLUSIONS

The luminescence and upconversion processes in nanocrystalline $Gd_3Ga_5O_{12}$: Ho^{3+} were investigated and discussed. Anti-Stokes emissions obtained after excitation into the $^5F_5$ level were attributed to an excited state absorption (ESA) mechanism occurring via the $^5I_7$ level. Excitation into the $^5I_4$ level with 756 nm radiation resulted in visible upconversion emission through another excited state absorption (ESA) mechanism. Temporal studies have demonstrated that the $^5I_7$ level is the intermediate state from which the excited state absorption (ESA) takes place.

4.6. AUTHOR'S NOTES AND SIGNIFICANCE OF THIS PAPER

This work on Ho^{3+} doped nanocrystalline $Gd_3Ga_5O_{12}$ was the first article published in the literature to report intense Ho^{3+} upconversion luminescence in a discrete nanocystalline powder. To increase the upconversion efficiencies to a greater extent, the GGG:Ho^{3+} sample was co-doped with Yb^{3+}. The disadvantage of upconversion systems based solely on one lanthanide ion is that the majority of the lanthanide ions possess low absorption cross sections in the NIR range were most commercially available diode lasers are available. Co-doping with Yb^{3+} overcomes this problem as it has the highest absorption cross section of any of the lanthanide ions in the NIR region. It is also capable of transferring the excitation energy to several of the other lanthanide ions, including Ho^{3+}, thus acting as an effective excitation channel through which the upconversion processes can occur. The following paper deals with the results of this study.

Chapter 5

Yb^{3+} Ion as a Sensitizer for the Upconversion Luminescence in Nanocrystalline $Gd_3Ga_5O_{12}$:Ho^{3+}

Published as:

J. C. Boyer, F. Vetrone, J. A. Capobianco, A. Speghini, and M. Bettinelli

Chemical Physics Letters **2004**, *390*, 403-407.

5.1. ABSTRACT

The effect of Yb^{3+} co-doping on the upconversion luminescence in nanocrystalline $Gd_3Ga_5O_{12}$:Ho^{3+} was examined. Strong and efficient NIR to green anti-Stokes luminescence was noted in nanocrystalline $Gd_3Ga_5O_{12}$:Ho^{3+}, Yb^{3+} after excitation into the $^2F_{5/2}$ level of Yb^{3+} with 978 nm radiation. Weaker blue, red and NIR anti-Stokes luminescence was also observed upon 978 nm excitation. An enhancement of the red $^5F_5 \rightarrow {}^5I_8$ luminescence was observed in the anti-Stokes spectrum compared to the Stokes emission spectrum. This enhancement was attributed to two distinct Energy Transfer Upconversion (ETU) mechanisms which preferentially populate the ($^5F_4$, $^5S_2$) and $^5F_5$ levels.

5.2. INTRODUCTION

An increasing amount of attention in the literature has been given recently to upconverting nanoparticles due to their fascinating potential. Upconversion is the generation of visible or UV light from lower energy radiation, usually NIR or IR, through the use of transition metal, lanthanide or actinide ions doped into a solid state host. Much of the interest in upconverting nanocrystalline materials is due to their prospective applications as biological fluorescence labels or as IR sensitive phosphors. Our group has recently examined the upconversion processes in nanocrystalline $Gd_3Ga_5O_{12}$ doped either with Er^{3+} or Ho^{3+}.[81, 173]

The Yb^{3+}-Ho^{3+} ion pair in solid-state hosts has attracted considerable interest as a possible green laser system which can be pumped with commercial laser diodes in the 980 nm range thereby taking advantage of the Yb^{3+} to Ho^{3+} energy transfer (ET).[174-176] Co-doping with Yb^{3+} overcomes the problem of the low absorption cross section of the Ho^{3+} ion in the NIR range where most commercially available diode lasers are available.[176] Thus, co-doping with Yb^{3+} offers an effective excitation channel through which the upconversion processes can occur.

The upconversion of NIR to visible light has been examined recently in single crystal $Gd_3Ga_5O_{12}$:Ho^{3+} co-doped with Yb^{3+}, pumping with a 978 nm IR diode laser.[168] The effect of Yb^{3+} and Tm^{3+} as a sensitizers for the 2 μm infrared emission in $Gd_3Ga_5O_{12}$:Ho^{3+}, along with the energy transfer process involved, has also been investigated in great detail.[93-97, 169] These studies have also looked at the upconversion processes under IR excitation in this material, but as a source of loss for the 2 μm Ho^{3+} emission. Here we present a detailed examination of the upconversion processes in nanocrystalline $Gd_3Ga_5O_{12}$:Ho^{3+}, Yb^{3+} under NIR excitation in which we will elucidate the energy transfer upconversion mechanisms responsible for the anti-Stokes emission.

5.3. EXPERIMENTAL

The $Gd_3Ga_5O_{12}$ nanocrystals doped with 1 mol% Ho^{3+} and 1 mol% Yb^{3+} were prepared using a solution combustion (propellant) synthesis procedure. This process involves the exothermic reaction between metal nitrates (oxidizer) and carbohydrazide. An aqueous solution containing appropriate quantities of carbohydrazide $(NH_2NH)_2CO$ (Aldrich, 98%), $Gd(NO_3)_3{\cdot}6H_2O$ (Aldrich, 99.99%), $Ga(NO_3)_3{\cdot}H_2O$ (Aldrich, 99.999%), $Ho(NO_3)_3{\cdot}6H_2O$ (Aldrich, 99.9%) and $Yb(NO_3)_3{\cdot}6H_2O$ (Aldrich, 99.9%) was prepared. A carbohydrazide-to-metal nitrate molar ratio of 2.5 was employed. Upon heating, the auto combustion process occurs with the evolution of brown fumes resulting in the formation of a very porous and voluminous mass of powder. The proposed stoichiometric synthesis reaction is:

$$3M(NO_3)_3 + 5Ga(NO_3)_3 + 3(NH_2NH)_2CO \rightarrow M_3Ga_5O_{12} + 24NO_2 + 6N_2 + 3CO_2 + 9H_2O$$

where M = Gd, Ho and Yb. The resultant powder from the combustion reaction was fired for 72 hours at 800 °C in order to decompose any residual carbohydrazide and nitrate ions. All nanocrystalline samples were kept in air without any further precaution.

Stokes emission spectra were measured by exciting at 457.9 nm using a Coherent Sabre Innova, 20 W argon laser. The anti-Stokes luminescence spectra were obtained by exciting at 978 nm using a Spectra-Physics Model 3900 Titanium Sapphire laser pumped by the 514.5 nm line of the argon ion laser. The visible emissions were then collected and dispersed using a Jarrell-Ash 1-meter Czerny Turner double monochromator. The emissions were monitored with a thermoelectrically cooled Hamamatsu R943-02 photomultiplier tube. The photomultiplier signals were amplified using a Stanford Research Systems model SR440 preamplifier. The amplified signals were acquired using a Stanford Research Systems model SR400 gated photon counter data acquisition system. The signal was recorded under computer control using Stanford SR465 data acquisition software. The near-infrared (NIR) emission spectra and decay times were recorded using a Jarrell-Ash ¾ meter Czerny-Turner single monochromator in second order. The signal was detected by a Northcoast EO-817P liquid nitrogen-cooled germanium detector connected to a computer-controlled Stanford Research Systems model SR510 lock-in amplifier.

Fluorescence lifetimes were measured by modulating the excitation beam using a Stanford Research Systems SR540 optical chopper. They were recorded using a Tektronix TDS 520A digital oscilloscope. The temporal dependence of the upconverted emission was obtained by modulating the excitation beam at 20 Hz with an optical chopper and recording the photomultiplier tube output using the digital oscilloscope. All spectroscopic measurements were carried out at room temperature.

A continuous flow cryostat (Janis Research ST-VP-4) was used to acquire the low temperature spectra and a Lakeshore model 330 controller was used to monitor the temperature.

5.4. RESULTS AND DISCUSSION

Wide angle powder X-ray diffraction revealed that the nanocrystalline samples under investigation have a particle size in the 15-30 nm range. A detailed investigation of the structure and morphology of these materials is presently under way.[170]

The room temperature Stokes luminescence spectrum of the $Gd_3Ga_5O_{12}$: Ho^{3+}, Yb^{3+} sample when excited into the $^3K_8$ level with 457.9 nm radiation is shown in Figure 5.1. Four emission bands are observed in the visible and NIR portion of the electromagnetic spectrum. According to the energy diagram for Ho^{3+}, the observed Stokes emissions are assigned to transitions within the 4*f*-4*f* levels of the Ho^{3+} ion as follows. The weak blue emission from 480 to 500 nm is assigned to the $^5F_3 \rightarrow {}^5I_8$ transition. The intense greed band around 550 nm is attributed to the $(^5F_4, {}^5S_2) \rightarrow {}^5I_8$ transition. The red emission in the region of 650 nm and the NIR emission centered at 750 nm were assigned to the $^5F_5 \rightarrow {}^5I_8$ and $(^5F_4, {}^5S_2) \rightarrow {}^5I_7$ transitions respectively. The peak positions of the Ho^{3+} ion transitions in both nanocrystalline samples are similar to what has been reported in the literature previously for single crystal $Gd_3Ga_5O_{12}$.[167, 168]

Figure 5.1. also shows the upconversion (anti-Stokes) luminescence of the $Gd_3Ga_5O_{12}$: Ho^{3+}, Yb^{3+} nanocrystals after excitation into the $^2F_{5/2}$ level of Yb^{3+} with 978 nm radiation. Similar to excitation at 457.9 nm, four emission bands were again observed in the visible and NIR portions of the spectrum. Emission was again observed from the $^5F_3 \rightarrow {}^5I_8$, $(^5F_4, {}^5S_2) \rightarrow {}^5I_8$, $^5F_5 \rightarrow {}^5I_8$ and $(^5F_4, {}^5S_2) \rightarrow {}^5I_7$ transitions. No emissions located higher in energy relative to the $^5F_3 \rightarrow {}^5I_8$ transition were observed.

The ratio of the green to red emission was found to be approximately 15:1 in the case of the anti-Stokes emission spectra. This is a significant change when compared to

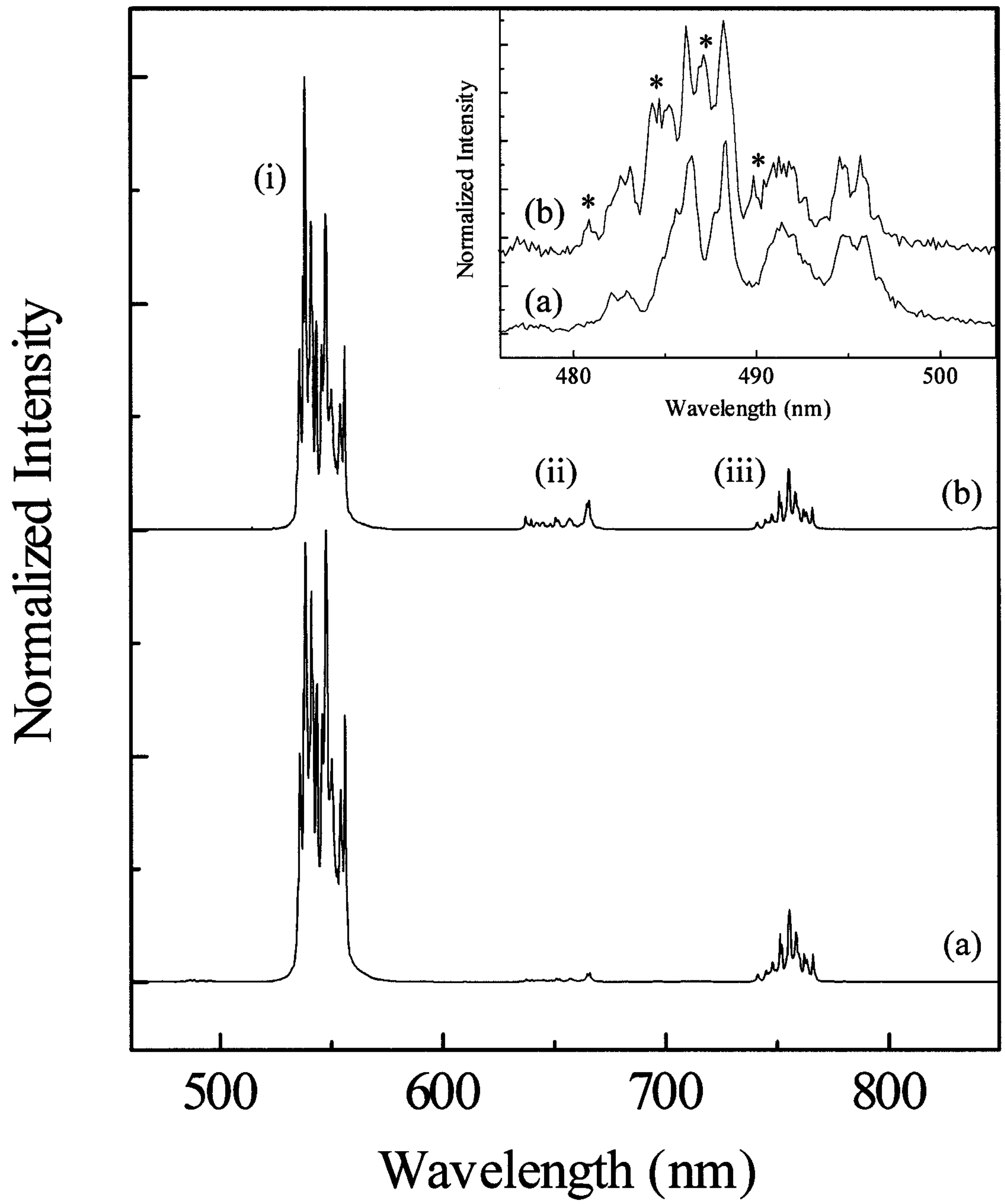

Figure 5.1. Room temperature (a) emission spectrum under λ_{ex} = 457.9 nm shown for comparative purposes. (b) anti-Stokes luminescence of nanocrystalline Gd3Ga5O12: Ho^{3+}, Yb^{3+} upon excitation at 978 nm. (i) ($^5F_4$, $^5S_2$) → $^5I_8$ (ii) $^5F_5$ → $^5I_8$ (iii) ($^5F_4$, $^5S_2$) → $^5I_7$ Inset: Weak blue $^5F_3$ → $^5I_8$ luminescence observed under (a) 457.9 nm and (b) 978 nm excitation. Extra peak character under 978 nm excitation is noted by *.

the spectrum obtained under 457.9 nm excitation where the ratio of the two emissions was 60:1. This is an indication that two separate upconversion mechanisms are responsible for populating the ($^5F_4$, $^5S_2$) and $^5F_5$ levels respectively.

To gain insight into the kinetics of the luminescence we examined the decay times for the ($^5F_4$, $^5S_2$) → $^5I_8$ and $^5F_5$ → $^5I_8$ transitions for both excitation wavelengths (Table 5.1.). The decay curve obtained for 457.9 nm excitation showed a slight deviation from single exponential behaviour. As such, we determined the emission decay constant, τ_m, using the following equation for the effective decay time:[177]

$$\tau_m = \frac{\int_0^\infty tI(t)dt}{\int_0^\infty I(t)dt} \tag{5.1.}$$

where $I(t)$ is the intensity at time t. An effective decay time of 43 μs was observed under 457.9 nm excitation, which represented a slight change over the 46 μs effective decay time determined for the same level in a singly doped Ho^{3+} 1 mol% sample [81]. This decrease in decay time can be related to a well documented energy transfer between the Ho^{3+} and Yb^{3+} ions.[175] However, the relatively small decrease shows that this Ho^{3+} to Yb^{3+} energy transfer is inefficient at current doping levels. Under 978 nm excitation, the decay curves of the ($^5F_4$, $^5S_2$) → $^5I_8$ and $^5F_5$ → $^5I_8$ transitions exhibit strong non-exponential behaviour and an increased effective decay time of 343 μs and 817 μs respectively compared to that obtained under 457.9 nm excitation. Both of these behaviours are considered to be a clear indication of energy transfer upconversion.[171]

Table 5.1. Decay times obtained from an effective decay fit of the room temperature decay curves for the ($^5F_4$, $^5S_2$) → $^5I_8$ and $^5F_5$ → $^5I_8$ transitions for 457.9 nm and 978 nm excitations.

Transition	**Decay Time (μs)**	
	λ_{ex} = 457.9 nm	**λ_{ex} = 978 nm**
($^5F_4$, $^5S_2$) → $^5I_8$	43 μs	343 μs
$^5F_5$ → $^5I_8$	104 μs	817 μs

The general formula relating the intensity of the upconversion luminescence I to the pump power P can be written as:

$$I \alpha P^n \qquad (5.2.)$$

where n is the number of pump photons required to excite the emitting state.[178] In order to determine the number of photons responsible for the upconversion mechanism, the intensities of the blue, green and red upconversion emissions were recorded as a function of the 978 nm excitation intensity (Figure 5.2.). The blue and green emissions intensities demonstrated quadratic power dependencies indicating two photon upconversion mechanisms. The $^5F_5$ → $^5I_8$ upconversion emission exhibited a power dependence close to 1.5, indicating a "saturated" two photon mechanism. Since upconversion is a nonlinear process, it cannot maintain its nonlinear behaviour up to infinite excitation energy as a consequence of the conservation of energy. As such, the dependence of upconversion luminescence intensity on pump power is expected to level off to a linear behaviour with increasing excitation, and a "saturation" of the luminescence intensity is observed for higher pump powers. This difference again confirms that the $^5F_5$ level is populated predominately through an alternate mechanism to the upper $^5F_3$ and ($^5F_4$,

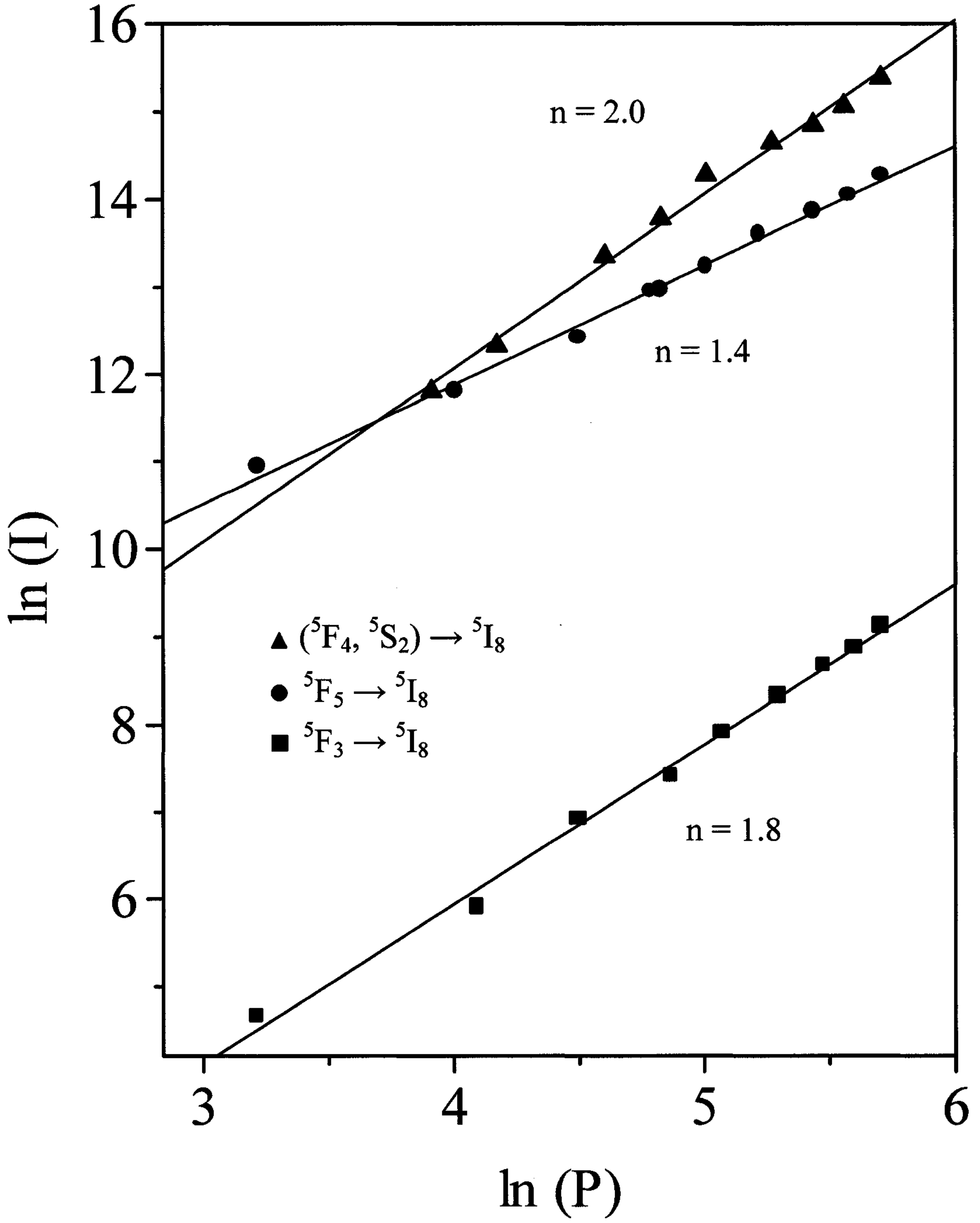

Figure 5.2. Room temperature power dependence of the upconverted blue $^5F_3 \rightarrow {}^5I_8$, green ($^5F_4$, $^5S_2$) → $^5I_8$ and red $^5F_5 \rightarrow {}^5I_8$ luminescence intensity for nanocrystalline $Gd_3Ga_5O_{12}$: Ho^{3+}, Yb^{3+} upon 978 nm excitation.

$^5S_2$) states. All three plots exhibited no inflection points thereby ruling out photon avalanche upconversion.

To gain an understanding of the upconversion mechanisms we examined both the temporal evolutions of the green and red emissions along with the decay times of the IR emissions of both the Yb^{3+} and Ho^{3+} ions (Figure 5.3.). Two distinct rises in the temporal evolutions for the green and red upconversion emissions were observed again indicating that two distinct mechanisms are responsible for these emission transitions.

The rise of the green emission (Figure 5.3.) was determined to be approximately 1.1 ms, which is the same as the experimentally determined decay time of the $^2F_{5/2}$ level of the Yb^{3+} ion. Thus, the $^2F_{5/2}$ decay time is determined to be the limiting step in the proposed upconversion mechanism populating the ($^5F_4$, $^5S_2$) levels (Figure 5.4.). The initial 978 nm photon will populate the $^2F_{5/2}$ level of the Yb^{3+} ion, which will then transfer its energy to a nearby Ho^{3+} ion thus populating the $^5I_6$ level. The difference in energy between the two states will be dissipated via the lattice. The ion is then promoted to the ($^5F_4$, $^5S_2$) levels either through another energy transfer from an Yb^{3+} ion in the $^2F_{5/2}$ state or an excited state absorption via the absorption of a 978 nm pump photon. The Ho^{3+} ion can then emit through the green ($^5F_4$, $^5S_2$) → $^5I_8$ transition. Alternatively, the ion can non-radiatively decay to the lower lying levels and the $^5F_5 \rightarrow {}^5I_8$ transition occurs.

A rise of 4.1 ms was observed for the temporal evolution of the red $^5F_5 \rightarrow {}^5I_8$ upconversion emission. This is in approximate agreement with the experimentally observed lifetime of the $^5I_7$ level in this host.[98] Therefore, the mechanism responsible for the population of the $^5F_5$ state must involve the $^5I_7$ level as an intermediate state (Figure 5.4.). Similar to the mechanism that populates the ($^5F_4$, $^5S_2$) levels, the first step in the

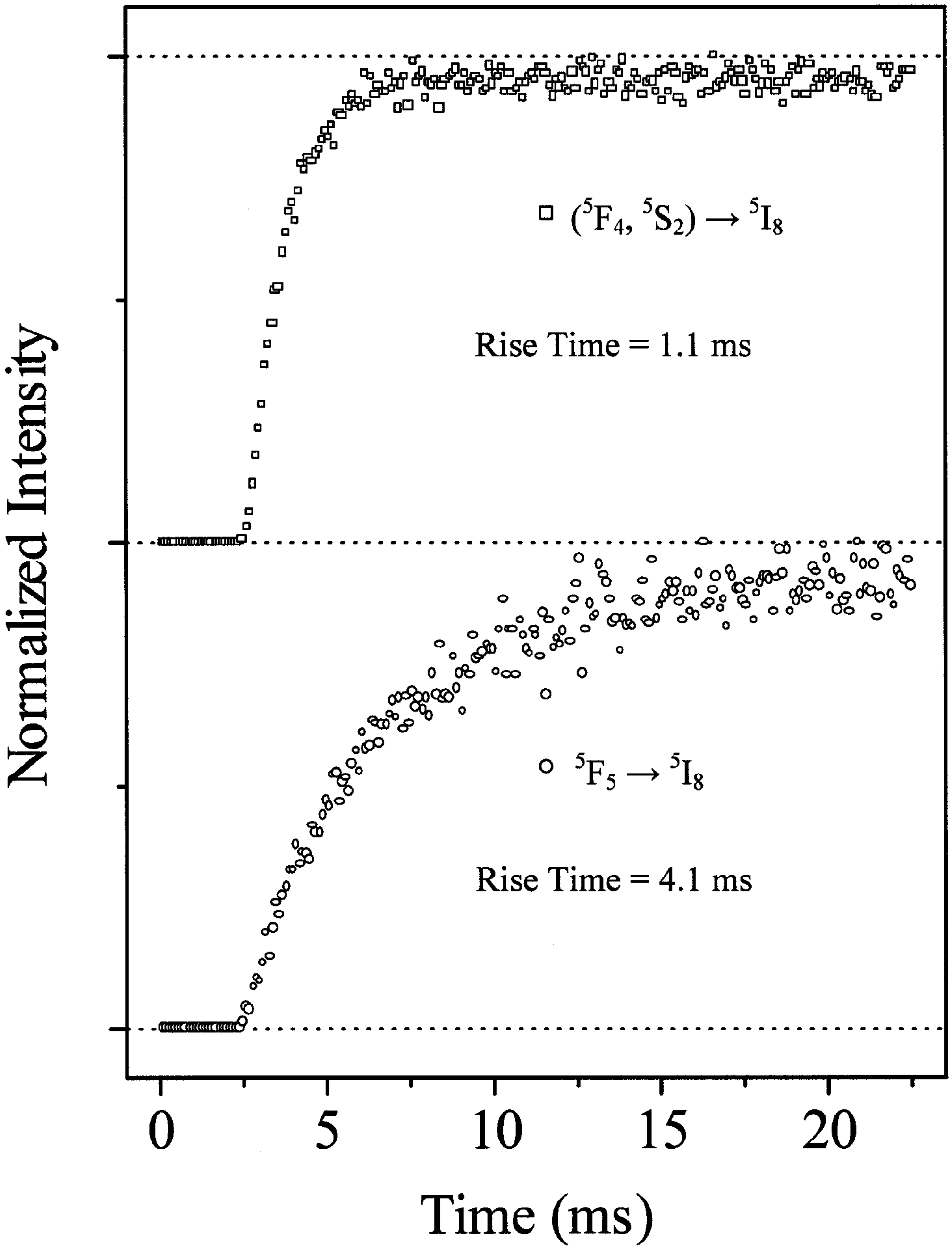

Figure 5.3. Temporal evolution of the green ($^5F_4$, $^5S_2$) → $^5I_8$ and red $^5F_5$ → $^5I_8$ upconverted luminescence in nanocrystalline $Gd_3Ga_5O_{12}$: Ho^{3+}, Yb^{3+} under 978 nm excitation.

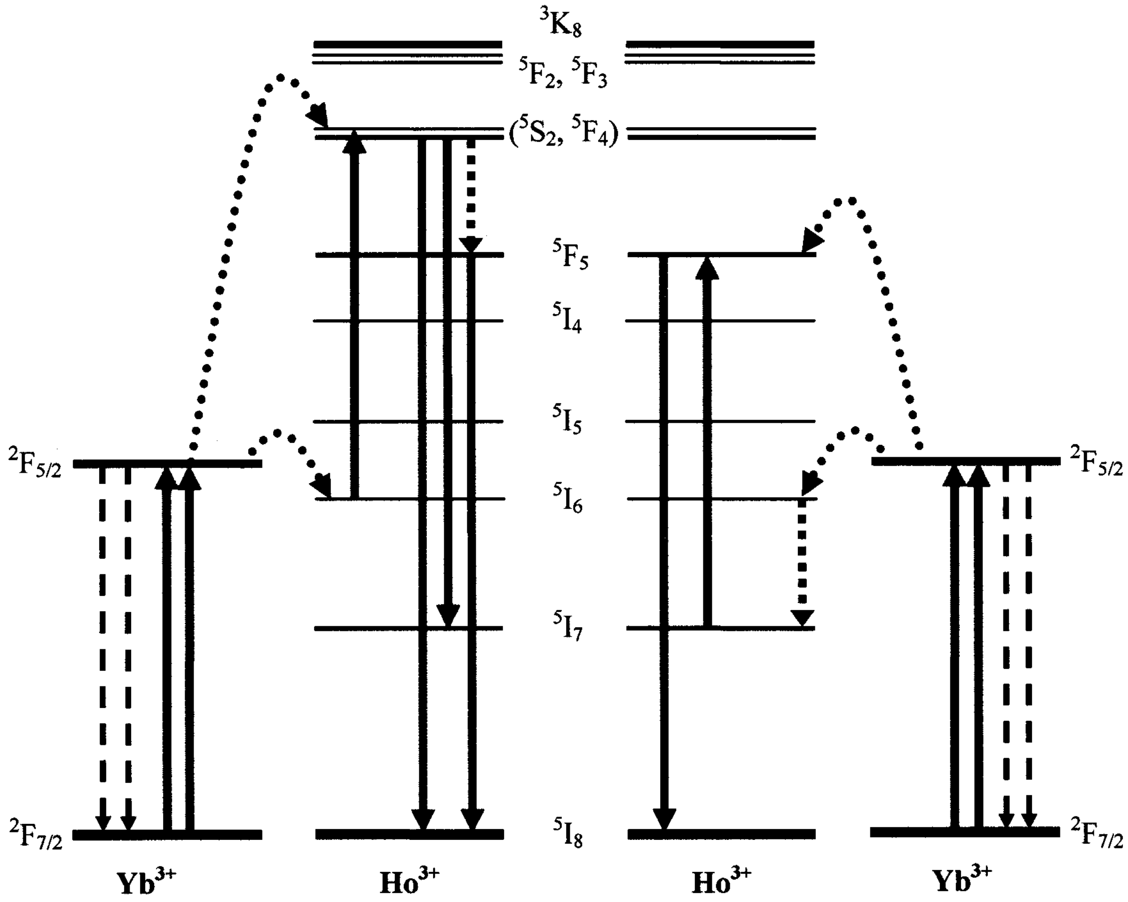

Figure 5.4. Principal upconversion mechanisms for the anti-Stokes green ($^5F_4$, $^5S_2$) → $^5I_8$ (left) and red $^5F_5$ → $^5I_8$ (right) luminescence in nanocrystalline $Gd_3Ga_5O_{12}$: Ho^{3+}, Yb^{3+} under 978 nm excitation.

mechanism involves population of the $^2F_{5/2}$ level of an Yb^{3+} ion via absorption of a 978 nm pump photon. An energy transfer process then occurs between the Yb^{3+} ion and a Ho^{3+} ion thus populating the $^5I_6$ state of the Ho^{3+} ion. The ion then decays non-radiatively to the $^5I_7$ level, where a subsequent energy transfer from an Yb^{3+} ion or an excited state absorption takes the Ho^{3+} ion up to the $^5F_5$ state. The red emission then occurs via the $^5F_5 \rightarrow {}^5I_8$ transition.

A weak blue emission was also observed under 978 nm excitation. This blue emission demonstrated a quadratic dependence on the 978 nm excitation power and is approximately twice the energy of the excitation wavelength. Thus, there are two possible mechanisms that could be responsible for the blue emission. Since the Ho^{3+} ion has no resonant absorption at 978 nm, the initial absorption must occur via the Yb^{3+} ion. An energy transfer could then occur between an Yb^{3+} ion in the $^2F_{5/2}$ state and the $^5I_5$ state of a Ho^{3+} ion with the difference in energy being made up by lattice vibrations. An ESA or a second ET from an Yb^{3+} ion could then populate the $^5F_3$ state of the Ho^{3+} ion resulting in the blue emission. An alternate mechanism could involve two Yb^{3+} ions in a cooperative upconversion mechanism that results in blue emission.[179, 180] This blue emission could also populate the $^5F_3$ state. This alternate mechanism could offer an explanation for the extra peak character in the blue portion of the spectrum that is observed in the upconversion spectrum.

To aid in the determination of the mechanism, the temperature dependence of the upconversion emissions was studied between 78 K and RT. It was found that the ratio of the blue to green emission did not change significantly over the temperature range examined. This effectively rules out the first proposed mechanism, where a phonon-assisted energy transfer from the $^2F_{5/2}$ state of the Yb^{3+} ion populates the $^5I_5$ state of a Ho^{3+} ion. Thus, the cooperative upconversion mechanism proposed above must be responsible for the observed blue emission. Elucidation of the Yb^{3+} ion concentration dependence on this cooperative upconversion mechanism will be the basis of future studies.

5.5. CONLUSIONS

The effect of Yb^{3+} codoping on the upconversion process in nanocrystalline $Gd_3Ga_5O_{12}$: Ho^{3+} is examined. We observed strong and efficient NIR to green upconversion in a nano-material. Enhancement of the red $^5F_5 \rightarrow {}^5I_8$ emission is observed relative to the green $(^5F_4, {}^5S_2) \rightarrow {}^5I_8$ emission when the sample is irradiated with 978 nm radiation. The enhancement is attributed to two distinct energy transfer mechanism which independently populate the $(^5F_4, {}^5S_2)$ and $^5F_5$ states. Evaluation of the upconversion temporal evolutions and the decay times of the IR levels indicate the intermediate levels in the two upconversion mechanisms are the $^5I_6$ and $^5I_7$ levels respectively. Studies are currently underway to determine the concentration effect of the Yb^{3+} ion doping on the upconversion luminescence.

5.6. AUTHOR'S NOTES AND SIGNIFICANCE OF THIS PAPER

This publication deals with the upconversion of Ho^{3+}/Yb^{3+} co-doped nanocrystalline $Gd_3Ga_5O_{12}$. The results published in this article were an important milestone in the field of nanocrystal research. For the first time in the literature, intense upconversion luminescence was reported for a Ho^{3+} doped nanocrystalline sample. At the time we thought this sample showed real promise as a potential upconversion phosphor and as an upconverting biological label.

In next chapter we present the results of our first effort to obtain discrete and dispersable upconverting nanoparticles. Shortly after the publication of the previous article our lab recognized that for the realization of upconverting biolabels or bioassays, upconverting nanoparticles would have to be synthesized that were capable of being dispersed as colloidal solutions. Though several of the oxide and garnet nanocrystalline samples investigated by our lab up to this point had realatively high upconversion efficiencies, none of the samples could be dispersed as clear colloidal solutions. We developed a method for producing upconverting lanthanide-doped $NaYF_4$ nanocrystals via the thermal decomposition of trifluoroacetate precusors in a mixture of oleic acid and octadecene. This method produced highly luminescent nanoparticles through a simple one-pot technique with only one preparatory step. The Er^{3+}, Yb^{3+} and Tm^{3+}, Yb^{3+} doped cubic $NaYF_4$ nanocrystals were colloidally stable in nonpolar organic solvents and exhibit green/red and blue upconversion luminescence, respectively under 977 nm laser excitation with low power densities.

Chapter 6

Synthesis of Colloidal Upconverting $NaYF_4$ Nanocrystals Doped with Er^{3+}, Yb^{3+} and Tm^{3+}, Yb^{3+} via Thermal Decomposition of Lanthanide Trifluoroacetate Precursors

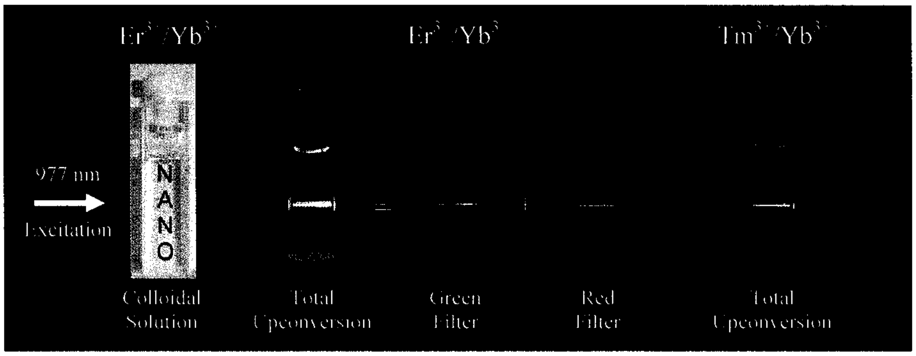

Published as:

J. C. Boyer, F. Vetrone, L. A. Cuccia, and J. A. Capobianco

Journal of the American Chemical Society **2006**, *128*, 7444-7445.

The synthesis and spectroscopy of upconverting nanocrystals (NCs) has recently garnered considerable attention due to their potential use as biolabels and in biological assays.[27-29, 103, 107] Upconverting phosphors have a number of properties that make them attractive for use in these tasks.[33, 114, 116, 181-183] Upconversion is the generation of higher energy light from lower energy radiation, usually near-infrared (NIR) or infrared (IR), through the use of transition metal, lanthanide or actinide ions doped into a solid state host. Organic dyes and semiconductor quantum dots that emit at higher energies via two-photon absorption processes requiring expensive high energy pulse lasers have also been investigated for use in these techniques.[184-186] Due to the relative high efficiency of the upconversion process in lanthanide doped materials inexpensive 980 nm NIR diode lasers may be employed as the excitation source. The realization of efficient NIR to visible upconverting NCs should unlock a realm of new possibilities in the field of biolabeling and bioassays.

The first step in achieving viable upconverting NCs is the selection of a material that is an efficient host for lanthanide ion upconversion. Gudel et al. have recently identified micrometer-sized Er^{3+}/Yb^{3+} or Tm^{3}/Yb^{3+} co-doped hexagonal $NaYF_4$ as the material with the highest upconversion efficiencies.[104, 105, 187] Several recent publications have reported upconversion from colloids of either cubic[27, 29] or hexagonal[103] $NaYF_4$ NCs, as well as hexagonal[28, 105] $NaGdF_4$ NCs. It is well known that metal trifluoroacetates thermally decompose to give the corresponding metal fluorides and various fluorinated and oxyfluorinated carbon species.[109, 111] The use of oleic acid together with the non-coordinating solvent octadecene for the synthesis of various types of NCs in also well documented.[101, 112, 113] Here we present a new synthetic route for cubic $NaYF_4$ NCs that exploits the combination of these two facts to provide highly luminescent nanoparticles through a simple one-pot technique with only one preparatory step.

The procedure for the synthesis of $NaYF_4$ NCs was adapted from a recently reported synthesis of LaF_3 nanoplates.[101] The lanthanide trifluoracetate precursors were prepared from the corresponding lanthanide oxides and trifluoracetic acid.[109] The corresponding amount of sodium trifluoroacetate was then added to the reaction vessel with octadecene and oleic acid. The resulting solution was heated to 100 °C under vacuum with stirring for 30 min to remove residual water and oxygen. The solution was then heated to 300 °C at a rate of 10 °C/min under Ar and kept at this temperature for 1 hr. Subsequently the mixture was allowed to cool to room temperature and the NCs were precipitated by the addition of hexane/acetone (v/v in 1:4) and isolated via centrifugation. The resulting pellet was then washed once with ethanol and further purified by dispersing in a minimum amount of chloroform and precipitated with excess ethanol. The resulting NCs were dried under vacuum for 24 hrs. The presence of the oleic acid ligand on the surface of the NCs was confirmed via the ^1H NMR of an undoped $NaYF_4$ sample (Figure 6.4. in supporting information). Due to the presence of the capping ligand, the NCs could be dispersed in nonpolar solvents and were colloidally stable in solution for a period of weeks with no visible agglomeration or settling.

Fig. 6.1. shows the characterization data for a $NaYF_4$: 2% Er^{3+}, 20% Yb^{3+} sample. The transmission electron microscopy (TEM) images (Fig. 6.1.A) show that the synthesized particles are roughly spherical. From the particle size distribution (Fig. 6.1.B), one can observe that the particles vary in size from 10 to 50 nm, with the majority

falling in the range between 15 to 30 nm. The powder X-ray diffraction (XRD) pattern (Fig. 6.1.C) of the sample shows well defined peaks indicating the high crystallinity of the synthesized material. The peak positions and intensities from the experimental XRD pattern match closely with the calculated pattern for cubic α-$NaYF_4$.[188] From the line broadening of the diffraction peaks, the crystallite size of the sample was determined to be approximately 25 nm using the Debye-Sherrer formula, which corresponds well to the average particle size determined from the TEM data.

Fig. 6.2.A-D shows photographs of a 1 wt.% solution of $NaYF_4$: 2% Er^{3+}, 20% Yb^{3+} NCs in dichloromethane demonstrating its transparency (Fig. 6.2.A) and the total visible upconversion luminescence under 977 nm excitation with a power density of 1.3 kW/cm^2 (Fig. 6.2.B). Fig. 6.2.C & D shows the same solution through appropriate green and red filters, respectively. Fig. 6.2.E demonstrates the upconversion luminescence of a 1 wt.% solution of $NaYF_4$: 2% Tm^{3+}, 20% Yb^{3+} in dichloromethane under the above excitation conditions.

The visible and NIR upconversion spectra of 1 wt.% solutions of $NaYF_4$: 2% Er^{3+}, 20% Yb^{3+} and $NaYF_4$: 2% Tm^{3+}, 20% Yb^{3+} NCs in dichloromethane under 977 nm excitation are shown in Fig. 6.3.A & B, respectively. The spectra correspond to what has been reported previously for Er^{3+} and Tm^{3+} upconversion in cubic $NaYF_4$ NCs.[27-29, 103, 107] In the Er^{3+} sample, green luminescence was observed from the $(^2H_{11/2}, ^4S_{3/2}) \rightarrow {}^4I_{15/2}$ and red from the $^4F_{9/2} \rightarrow {}^4I_{15/2}$ transitions, respectively. The power dependencies of the green and red luminescence (Fig. 6.5. in supporting information) were found to be approximately 2 indicating that two photons were involved in the upconversion mechanism. Four spectral bands were observed in the Tm^{3+} sample and were assigned to

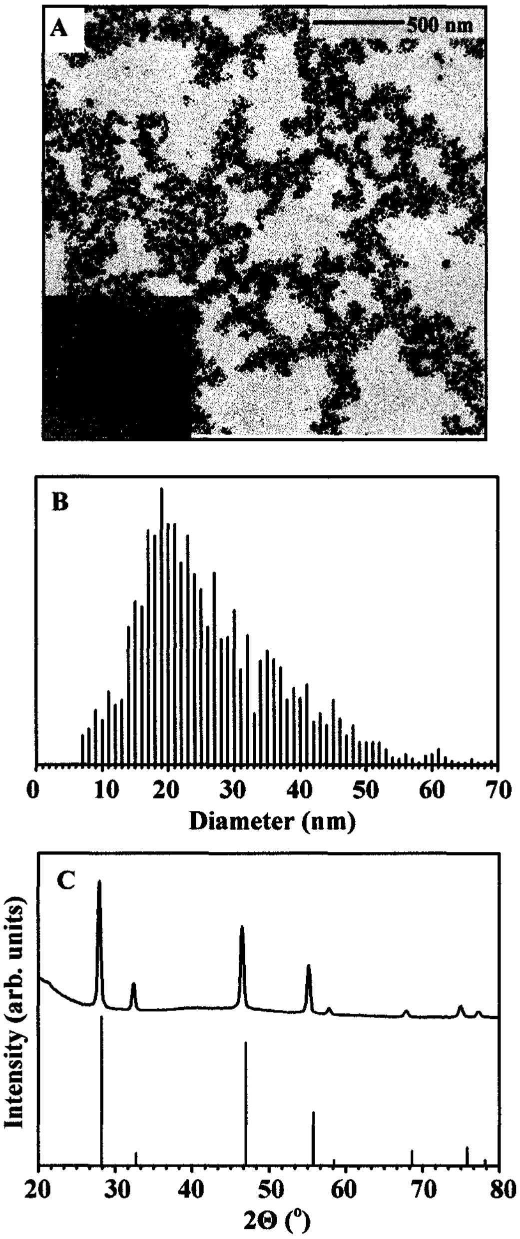

Figure 6.1. Characterization data for $NaYF_4$: Er^{3+} 2%, Yb^{3+} 20% nanocrystals. A) Transmission electron microscopy (TEM) image. Inset: High resolution TEM (HRTEM) image of a single nanocrystal. B) Histogram of the particle sizes obtained from TEM images of ~1400 nanocrystals. C) Experimental powder x-ray diffraction (XRD) pattern (upper) and the calculated line pattern for α-$NaYF_4$ (lower).

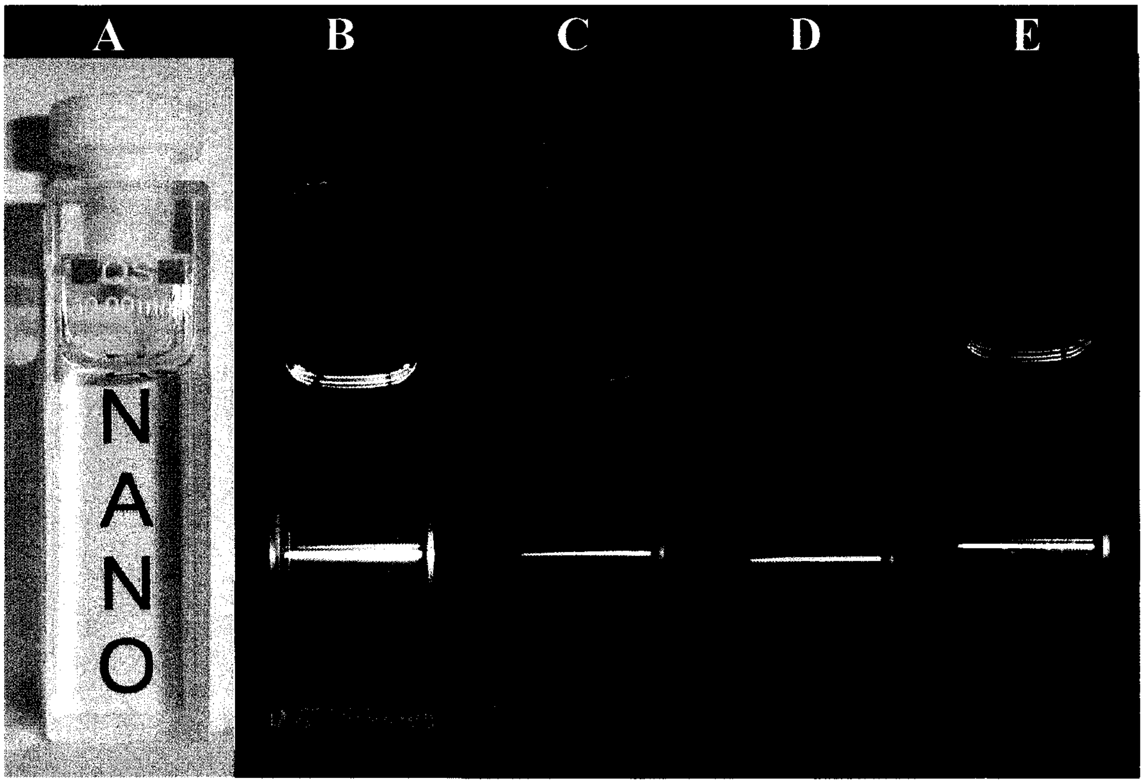

Figure 6.2. 1 wt.% colloidal solutions of nanocrystals in dichloromethane excited at 977 nm demonstrating upconversion luminescence. A) $NaYF_4$: Er^{3+} 2%, Yb^{3+} 20% solution showing its transparency. B) Total upconversion luminescence of $NaYF_4$: Er^{3+} 2%, Yb^{3+} 20% solution. C, D) $NaYF_4$: Er^{3+} 2%, Yb^{3+} 20% upconversion viewed through green and red filters, respectively. E) $NaYF_4$: Tm^{3+} 2%, Yb^{3+} 20% solution.

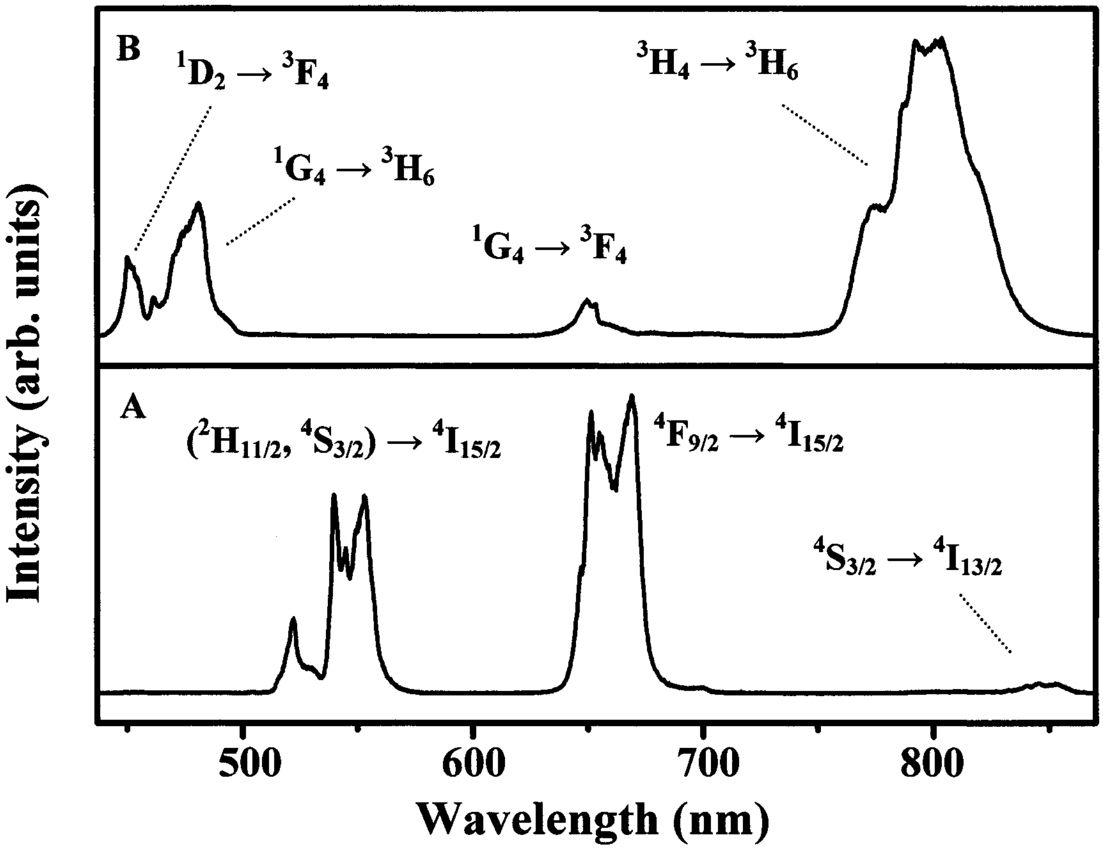

Figure 6.3. Luminescence emission spectra of 1 wt.% colloidal solutions of nanocrystals in dichloromethane excited at 977 nm. A) $NaYF_4$: Er^{3+} 2%, Yb^{3+} 20% and B) $NaYF_4$: Tm^{3+} 2%, Yb^{3+} 20%.

the $^1G_4 \rightarrow {}^3H_6$, $^1D_2 \rightarrow {}^3F_4$, $^1G_4 \rightarrow {}^3F_4$ and $^3H_4 \rightarrow {}^3H_6$ transitions. The mechanisms responsible for the upconversion luminescence are shown in the supporting information for the article (Fig. 6.6. in supporting information).

We have reported a novel and straightforward synthesis for upconverting lanthanide-doped NCs that requires few preparatory steps. The Er^{3+}, Yb^{3+} and Tm^{3+}, Yb^{3+} doped particles exhibit green/red and blue upconversion luminescence respectively under 977 nm laser excitation with low power densities. Further refinement of the synthesis is currently underway to obtain a narrower particle size distribution as well as core-shell NCs where a shell of undoped $NaYF_4$ is grown over the lanthanide-doped $NaYF_4$ core. Investigation of additional cappings ligands and post synthetic surface treatments are also ongoing to obtain water-dispersible NCs.

6.1. SUPPORTING INFORMATION

6.1.1. Synthesis of Ln^{3+} doped $NaYF_4$ nanocrystals

It should be noted beforehand that the decomposition of the metal trifluoroacetates produces various fluorinated and oxyfluorinated carbon species such as trifluoroacetic anhydride $(CF_3CO)_2O$, trifluoroacetyl fluoride CF_3CF_2COF, carbonyl difluoride COF_2 and tetrafluoroethylene C_2F_4. These species are considered toxic and as such the reaction should be carried out in a well ventilated hood. Care should also be exercised as not to inhale any of the evolved gases from the reaction.

All chemicals utilized in the synthesis of the nanocrystals were purchased from Aldrich. The lanthanide trifluoracetate precursors were prepared from the corresponding lanthanide and yttrium oxides and trifluoroacetic acid (99%). In the case of the $NaYF_4$: Er^{3+} 2 mol%, Yb^{3+} 20 mol% codoped sample, 9.6 mg (0.025 mmol) of Er_2O_3, 98.5 mg (0.25 mmol) of Yb_2O_3, and 220.2 mg (0.975 mmol) of Y_2O_3 were dissolved in 10 mL of 50% aqueous trifluoroacetic acid at 80 °C. The residual water and acid were then slowly evaporated to dryness at 50 °C. The 0.3400 g (2.5 mmol) of sodium trifluoroacetate (98%) was then added to the reaction vessel with 20 mL of octadecene (90%) and 20 mL of oleic acid (90%). The resulting solution was slowly heated to 100 °C under vacuum with magnetic stirring for 30 minutes to remove residual water and oxygen during which time the flask was purged periodically with dry argon gas. The resulting clear solution had a slight yellow color. The solution was then heated to 300 °C at a rate of 10 °C/min under dry argon and kept at this temperature for 1 hr. At approximately 250 °C, the evolution of small gas bubbles was observed from the solution indicating the decomposition of the metal trifluoroacetates. A burst of nucleation was observed between 280-300 °C which resulted in the solution becoming turbid. Subsequently, the mixture was allowed to cool to room temperature during which time the solution became clear and a yellow colloidal solution was obtained. The nanocrystals were precipitated by the addition of hexane/acetone (v/v in 1:4) and isolated via centrifugation at 3000 rpm corresponding to a relative centrifugal field (RCF) of approximately 1000. The resulting pellet was then washed once with ethanol and further purified by dispersing in a minimum amount of chloroform and precipitated with excess ethanol. The resulting nanocrystals were dried under vacuum for a minimum of 24 hrs. The resulting nanocrystals could be dispersed in nonpolar solvents (e.g. hexane, toluene, dichloromethane) by sonicating a suspension of the nanocrystals in a bath sonicator for 10-20 minutes. It was sometimes necessary to add one or two drops of oleic acid to the suspension to aid in the dispersion of the nanocrystals. To eliminate this addition of oleic acid, it was preferable to leave the nanocrystals in a 'muddy' state instead of the dry powder form.

It must be stated that the health and environmental effects of the synthesized $NaYF_4$ nanocrystals have yet to be determined fully. As a result, suitable precautions should be exercised when dealing with the powders and their colloidal solution. The use of appropriate eye and skin protection should always be employed when handling the materials.

6.1.2. NMR Measurements

The ^1H NMR spectrum of an undoped $NaYF_4$ sample dispersed in $CDCl_3$ was recorded using a Varian 300 MHz spectrometer. The spectrometer frequency was 300.03

MHz and 128 transients were recorded. The residual proton signals of the deuterated solvents were used as internal standards ($CDCl_3$ ^1H δ: 7.27 ppm).

6.1.3. Powder X-ray Diffraction Analysis

The powder diffraction patterns were collected at room temperature with the Kα (40 kV, 20 mA) radiation of Cu on a PW-1050 Philips diffractometer automated with the Difftech Sie-Ray system. Data accumulation and processing were carried out using the Difftech Sie-122 software. The scanning step size was 0.05° 2θ with a counting time of 10 s per step.

6.1.4. Transmission Electron Microscopy (TEM) Studies

TEM was performed on a $NaYF_4$: Er^{3+} 2%, Yb^{3+} 20% sample using a JEOL JEM-2000 FX microscope operating at 80 kV equipped with a charged-coupled device (CCD)-camera (Gatan). A small amount of the sample (~1 mg) was dispersed in 1 g of hexane to give an approximate 0.1 wt% solution. One drop of the resulting solution was evaporated on a formvar/carbon film supported on a 300 mesh copper grid (3 mm in diameter). High resolution TEM was performed on the same sample using a 200 KeV JEOL JEM-2100F microscope.

6.1.5. Visible and NIR Room Temperature Emission Spectroscopy (λ_{exc} = 977 nm)

The upconverted emission spectra were obtained using 977 nm radiation from a Spectra-Physics model 3900 Ti sapphire laser pumped by the 514.5 nm line of the Coherent Sabre Innova 20 W Argon Ion laser. For the upconversion studies, the samples were placed in 1 cm path-length quartz cuvettes (Hellma, QS). The visible emissions were collected from the samples at $\pi/2$ from the incident beam and then dispersed by a 1 m Jarrell-Ash Czerny-Turner double monochromator. Resolution of the monochromator was 0.2 nm with slit widths of 200 μm. The visible emissions from the sample exiting the monochromator were detected by a thermoelectrically cooled Hamamatsu R943-02 photomultiplier tube and the photomultiplied signals were processed by a Stanford Research Systems (SRS) model SR440 preamplifier. A Stanford Research Systems model SR 400 gated photon counter data acquisition system was used as an interface between the spectroscopic equipment and the computer running the SRS SR 465 data acquisition software.

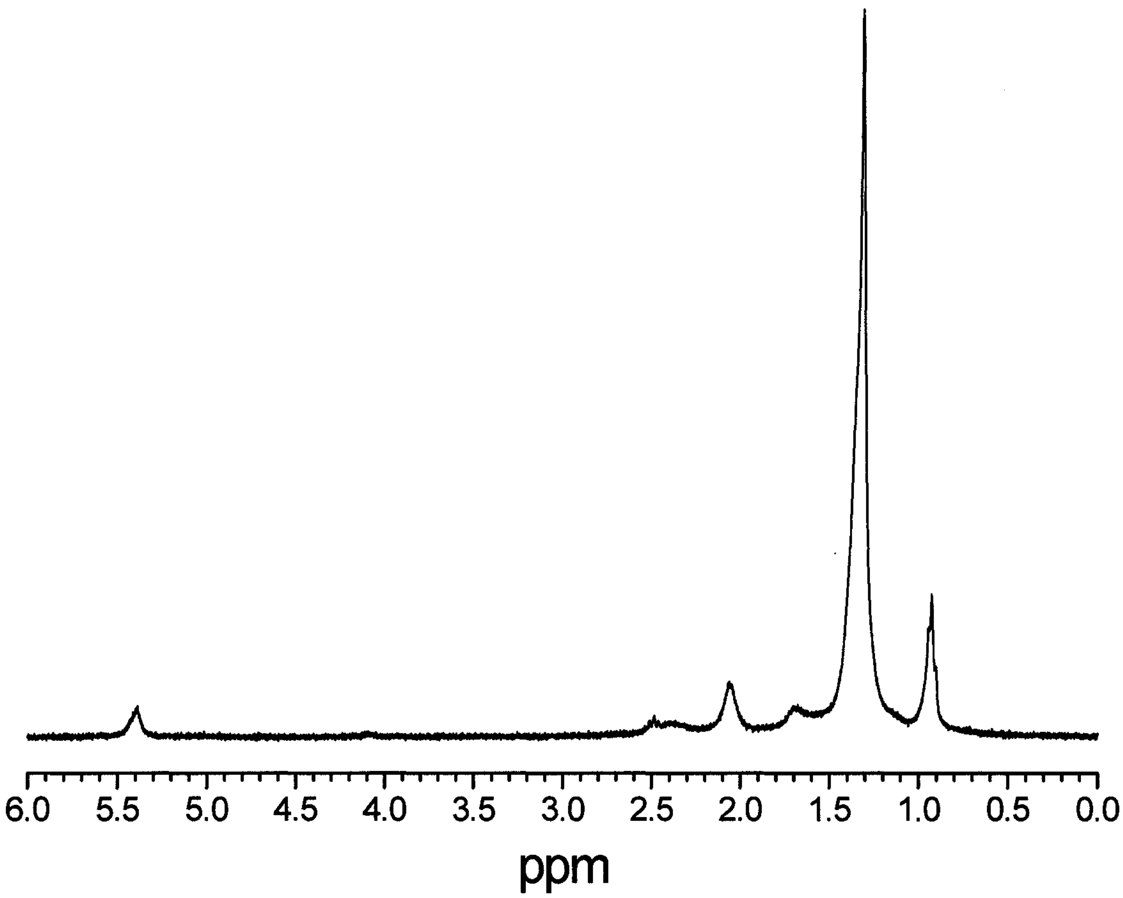

Figure 6.4. The ^{1}H NMR spectrum of an undoped $NaYF_4$ sample dispersed in $CDCl_3$ recorded on a Varian 300 MHz spectrometer. Chemical shifts are reported in parts-per-million δ: 5.3-5.45 (broad, -HC=CH-), 2.0-2.1 (broad, CH_3-$(CH_2)_6$-CH_2-CH=CH-CH_2-$(CH_2)_6$-COOH), 1.2-1.4 (broad, -$(CH_2)_6$-) and 0.85-1.00 (broad, -CH_3).

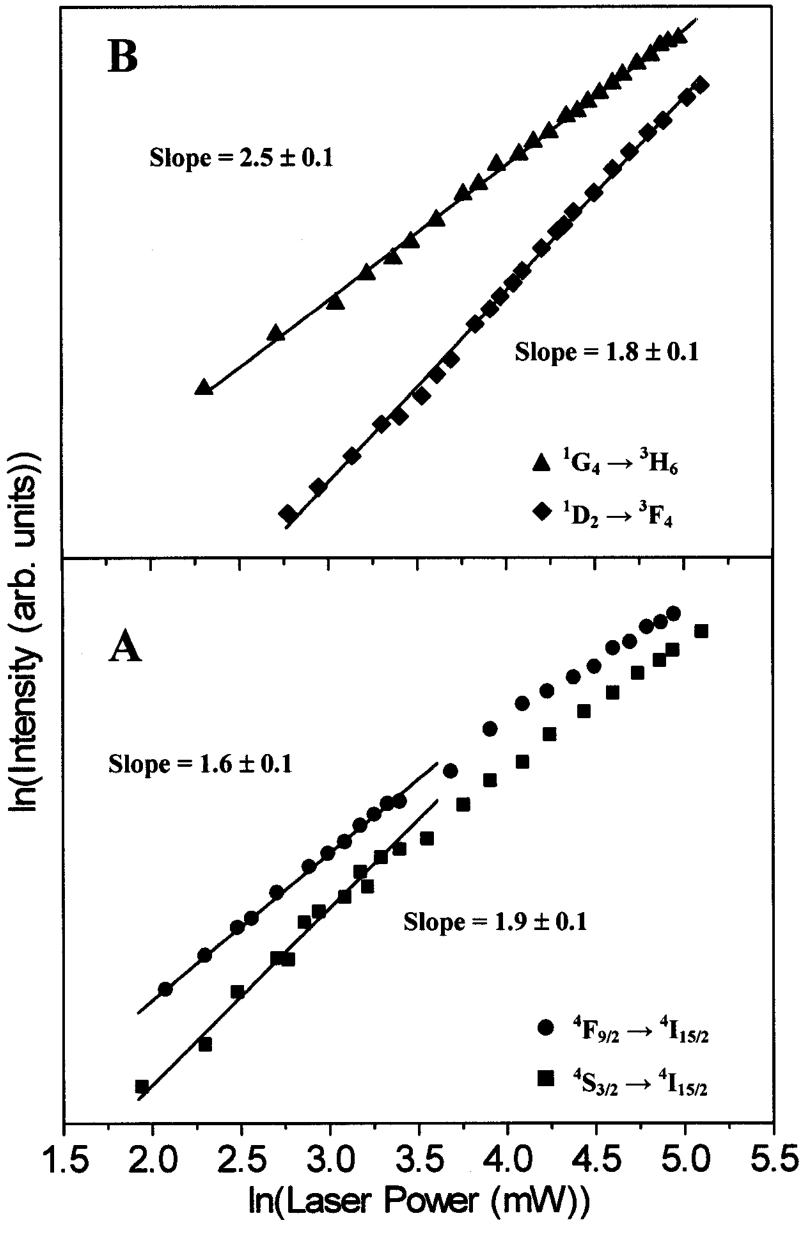

Figure 6.5. Power dependence of the upconverted emissions of 1 wt.% colloidal solutions of nanocrystals in dichloromethane excited at 977 nm. A) $NaYF_4$: Er^{3+} 2%, Yb^{3+} 20% and B) $NaYF_4$: Tm^{3+} 2%, Yb^{3+} 20%. In the case of the $NaYF_4$: Er^{3+} 2%, Yb^{3+} 20% sample, the straight lines are least-squares fit to the low power data points. At higher excitation densities the power dependence of the emissions are observed to level off due to saturation of the upconversion processes. For the $NaYF_4$: Tm^{3+} 2%, Yb^{3+} 20% sample, the least-squares fit to the data points give a value that is lower than the expected due to the saturation of the upconversion processes.

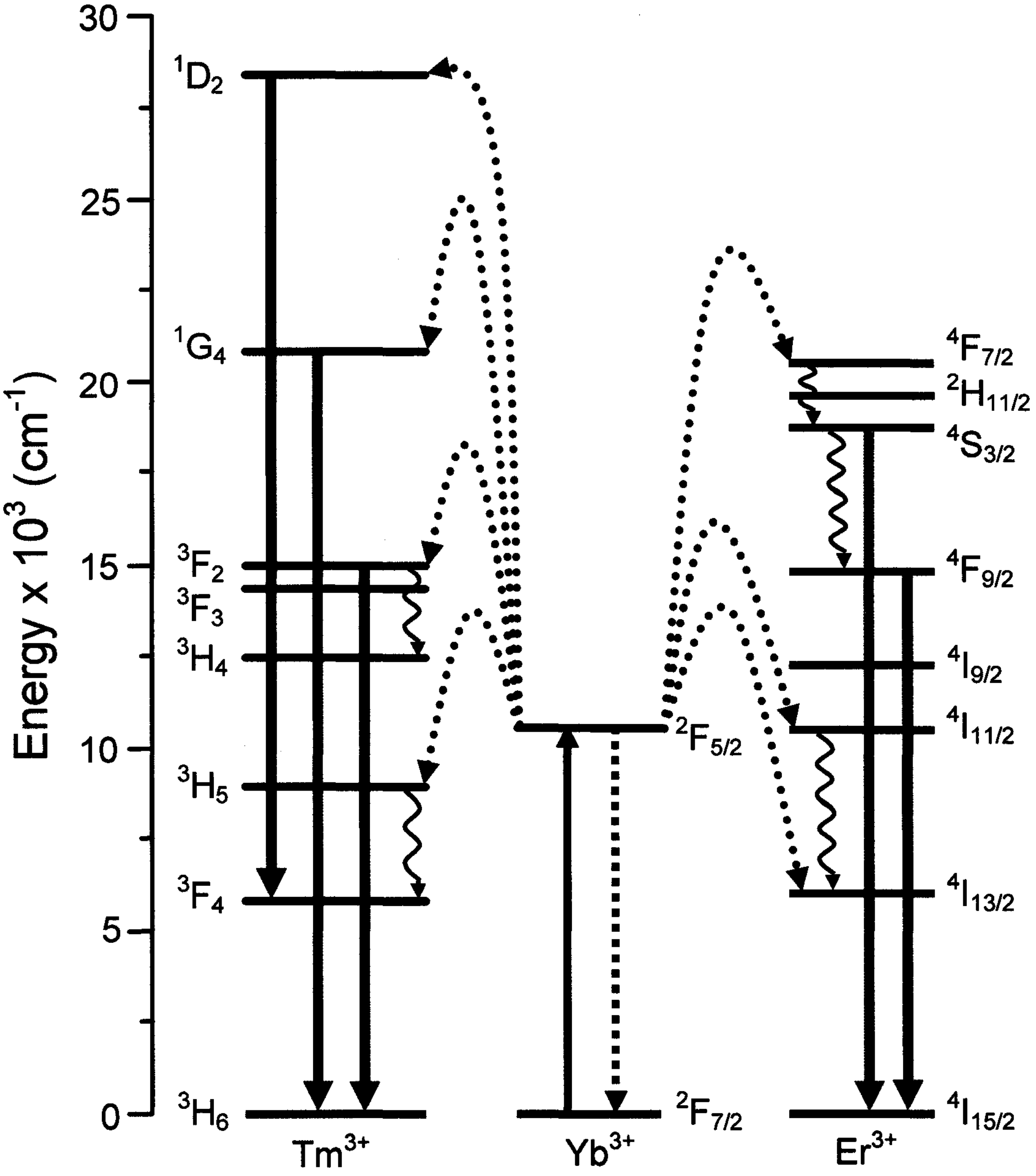

Figure 6.6. The energy level diagrams of the Er^{3+}, Tm^{3+} and Yb^{3+} dopant ions and upconversion mechanisms following excitation with 977 nm. The full, dotted, and curly arrows represent emission, energy transfer and multiphonon relaxation processes, respectively.

6.2. AUTHOR'S NOTES AND SIGNIFICANCE OF THIS PAPER

This publication details our initial efforts in synthesizing and characterizing colloidal upconverting $NaYF_4$ nanoparticles. The nanoparticles in this study were synthesized via the thermal decomposition of lanthanide trifluoroacetate precursors in a mixture of oleic acid and octadecene. The resulting nanoparticles can be dispersed in a variety of nonpolar organic solvents due to the presence of oleate ligands on their surfaces. The transparent colloidal solutions of there particles were shown to upconvert 977 nm laser radiation into visible light under moderate excitation densities. This was the first report of upconversion luminescence in the literature from $NaYF_4$ nanoparticles synthesized via this thermal decomposition method.

This synthesis has several advantages over previously published synthetic methods for producing $NaYF_4$ nanoparticles. Previous methods have utilized difficult to handle chemicals such as sodium metal and/or hydrofluoric acid. Another alternative method presented in the literature utilizes a high pressure reaction vessel to obtain the final nanoparticles while our method uses no complicated equipment of techniques. We also employed technical grade solvents and ligands in the synthesis thus reducing the cost and making commercialization possible.

Though this was a significant advancement in the synthesis of upconverting nanoparticles, refinement of the synthesis was still needed to obtain nanoparticles with a defined shape and a narrower particles size range. By introducing the lanthanide precursors slowly into the high temperature reaction mixture we were able to achive these goals. The follow work is the first in the literature to report synthesis of upconverting $NaYF_4$ nanocrystals with a truly monodisperse particle size and uniform shape.

Chapter 7

Synthesis of Colloidal Upconverting $NaYF_4$: Er^{3+}/Yb^{3+} and Tm^{3+}/Yb^{3+} Monodisperse Nanocrystals

Accepted as:

J. C. Boyer, L. A. Cuccia, and J. A. Capobianco

Nano Letters **2006**, *In Press*.

The synthesis and spectroscopy of upconverting nanocrystals (NCs) has garnered a tremendous amount of attention in the literature recently.[27, 29, 102, 103, 106, 107, 189-191] Upconversion is a process where low energy light, usually near-infrared (NIR) or infrared (IR), is converted to higher energies, ultraviolet (UV) or visible, *via* multiple absorptions or energy transfers.[71, 72] This phenomenon has been observed in transition metal, lanthanide and actinide ions, though the highest efficiencies are found in lanthanide doped materials. To date, the highest upconversion efficiencies observed have been in hexagonal phase $NaYF_4$ bulk materials doped with the Er^{3+}/Yb^{3+} or Tm^{3+}/Yb^{3+} ion couples synthesized *via* solid state methods.[105, 187] Colloids of upconverting $NaYF_4$ NCs, and the related material $NaGdF_4$, have also been synthesized through thermal decomposition, precipitation, and high pressure reactions.[27-29, 102, 103] The ability to suspend upconverting NCs as clear colloidal solutions has opened the door for their use in several new technologies, the most promising of which appears to be for use as labels in biological assays and imaging.

Upconverting $NaYF_4$ NCs doped with the Er^{3+}/Yb^{3+} have already been successfully applied to analyte and DNA detection.[106, 107] The use of upconverting nanophosphors for bioimaging has also been demonstrated.[192] The majority of current commercialized labels, such as organic dyes and quantum dots (QDs), utilize the Stokes luminescence of the fluorophore under UV, blue or green excitation in order to detect the analyte. This leads to the possibility of high background signals and difficulty in choosing an appropriate label as many biological species fluoresce under ultraviolet or visible radiation. The use of upconverting NCs, two-photon dyes or two-photon QDs removes many of these difficulties.[33, 114, 116, 117, 181, 182, 184-186] The drawback with the use of dyes or quantum dots is the need for expensive pulse lasers to meet the high power densities required to observe the two-photon effect.[184-186] One may also increase the sensitivity further by choosing a detection system with low response in the wavelength range of the IR excitation source.

We have previously synthesized upconverting cubic $NaYF_4$ NCs doped with the Er^{3+}/Yb^{3+} or Tm^{3+}/Yb^{3+} ion couples *via* the thermal decomposition of trifluoroacetate precursors in a high-boiling point organic sovent.[82] A similar approach was used in the literature to produce sodium rare-earth fluoride nanocrystals and LaF_3 nanoplates.[101, 102] These procedures take advantage of the fact that the metal trifluoroacetates thermally decompose to give the corresponding metal fluorides at relatively low temperatures (200-300 °C).[109-111, 193] In these methods the noncordinating solvent octadecene was used as the primary solvent due to its high boiling point (315 °C). Oleic acid was chosen as the coordinating ligand due to its successful use in the synthesis of various types of nanocrystals.[112, 113] In this paper we present a modification of the synthetic procedure that results in the synthesis of cubic $NaYF_4$ particles with a narrow particle size range and well defined shape. These particles are capable of being colloidally dispersed in various non-polar organic solvents (e.g. hexane, toluene, dichloromethane) and are able to emit visible light under 980 nm laser diode excitation via the upconversion process under relatively low excitation power densities. This method uses inexpensive technical grade chemicals which reduces the cost of the nanoparticle synthesis and a relatively low cost laser diode for excitation hence making them attractive for potential commercial applications.

The synthesis report here for $NaYF_4$ NCs is a modification of recently reported synthetic procedures for LaF_3 nanoplates and $NaYF_4$ NCs.[82, 101, 102] The lanthanide trifluoroacetate precursors for the synthesis were prepared from the corresponding lanthanide oxides and trifluoroacetic acid in a three-neck round bottom flask. The corresponding amount of sodium trifluoroacetate was then added to the lanthanide trifluoroacetates in the reaction vessel with 5 mL of octadecene and 10 mL of oleic acid. A second solution of of 15 mL of octadecene and 10 mL oleic acid was then prepared in a second three-neck round bottom flask. Both solutions were heated slowly to 125 °C under vacuum with stirring and kept at this temperature for 30 min to remove residual water and oxygen. The second solution was then heated to 310 °C under Argon and maintained at this temperature. The lanthanide trifluoroacetate solution at 125 °C was then transferred dropwise into the second solution over a period of 15 minutes using a stainless steel cannula at a flow rate of ca. 1 mL/min. During this time the second solution was maintained at 310 °C. After the addition was complete the temperature of the reaction mixture was lowered to 305 °C and kept at this temperature for 1 hr under dry argon. Subsequently the mixture was removed from the heating mantle and cooled to room temperature. The NCs were precipitated by the addition of excess ethanol and isolated via centrifugation. The resulting pellet was then washed twice by dispersing with ethanol and centrifugated. The resulting NCs were dried under air for 24 hrs. Due to the presence of the capping ligand, the NCs could be dispersed in nonpolar solvents and were colloidally stable in solution for a period of weeks with no visible agglomeration or settling. A more detailed description of the synthetic procedure and spectroscopy setup is given in the supporting information of the article.

Figure 7.1. shows the transmission electron microscopy (TEM) data for a $NaYF_4$: 2% Er^{3+}, 20% Yb^{3+} NC sample. From the low resolution micrographs, Figure 7.1.A and B, one can observe that the synthesized particles appear hexagonal in shape and are nearly monodisperse. From a detailed particle size analysis of 500 particles from several low resolution TEM micrographs (Figure 7.7. in supporting information), the average particle size was found to be 27.6 nm with a standard deviation of 1.6 nm. Further proof of the uniform particle size and shape of the particles reported herein is provided by their assembly into a regular two-dimensional hexagonal close packed arrangement on the TEM grid due to the presence of the oleic acid capping ligand on the surface of the particles.

From the high resolution TEM (HRTEM) image, Figure 7.1.C, the distance between the particles was found to be 2.8 ± 0.5 nm which is somewhat less than two times the length of a single oleate molecule (2.2 nm from semi-empirical calculation). This is a good indication that there is interdigitation of the alkyl chains from neighboring particles or that the oleic acid chains are not in a fully extended conformation. From the HRTEM image one can also clearly distinguish lattice fringes on the individual particles indicating that the particles are highly crystalline. The distances between the lattice fringes were measured to be 3.2 and 2.8 which correspond to the d-spacing for the (111) and (200) lattice planes, respectively, in the cubic $NaYF_4$ structure.[188, 194, 195] From this we can conclude that the particles have a polyhedron shape and are truncated octahedral bordered by the (111) and (002) lattice planes.[196] The hexagonal shape of the particles observed in the TEM images are 2D projections of the 3D truncated octahedral geometry. The selected area electron diffraction (SAED) pattern of the particles (Figure 7.1.D) can

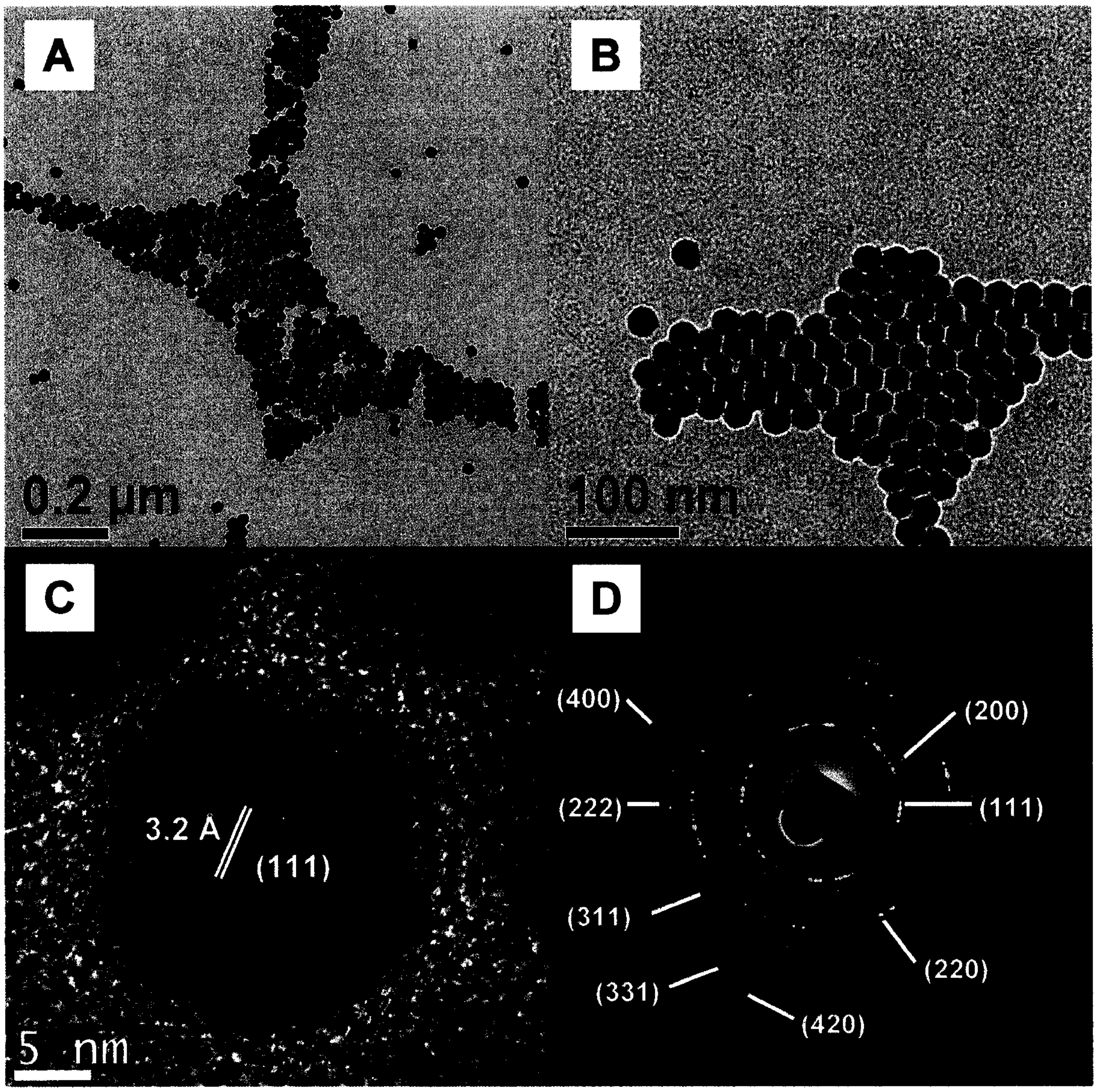

Figure 7.1. (A-B) Low resolution transmission electron micrographs of NaYF$_4$: 2% Er^{3+}, 20% Yb^{3+} sample showing uniformity of the particles. (C) High resolution micrographs of a single NaYF$_4$: 2% Er^{3+}, 20% Yb^{3+} particle showing lattice fringes. (D) Selected area electron diffraction pattern (SAED) of NaYF$_4$: 2% Er^{3+}, 20% Yb^{3+} particles.

be indexed to the (111), (200), (220), (311), (222), (400), and (331) planes of the standard cubic α-$NaYF_4$ structure (JCPDS: 6-0342) as seen in Table 7.1. As well, the particles were found to be single crystallites as the Fourier transformation on individual particles returned patterns corresponding to a single set of (111) and (200) planes.

In a previous study we found that the synthesis of α-$NaYF_4$ nanoparticles in octadecene and oleic acid resulted in irregularly shaped particles with a wide particle size range.[82] It is clear from the TEM data that the modifications made to the earlier synthetic procedure results in α-$NaYF_4$ nanoparticles with a defined shape and monodisperse size distribution. It can be assumed that the decomposition of the trifluoroacetate precursors and thus the crystallization of the $NaYF_4$ particles occur quite fast at the temperatures used in this synthesis (310 °C). By adding the precursors to the solution slowly one can control the rate of decomposition and formation of the particles. In essence, by performing the addition over a longer period of time one can separate the nucleation and growth phases of the nanocrystals resulting in a monodisperse particle size. This method also allows the oleic acid to complex to the surface of the growing particles more effectively due to the initial low concentration of precursor in the solution. The oleic acid ligands modulate the growth rate along the <111> and <200> directions of the cubic $NaYF_4$ nanocrystals resulting in the truncated octahedral shape.

The presence of the oleic acid ligand on the surface of the NCs was confirmed using ^1H NMR of an undoped $NaYF_4$ sample. The ^1H NMR of the undoped $NaYF_4$ sample dispersed in $CDCl_3$ is shown in Figure 7.8. in supporting information, along with the ^1H NMR of free oleic acid for reference. The ^1H NMR signals of the bound oleic acid molecules on the surface of the nanoparticles are broadened with respect to those of the free oleic acid. The broadening is due to an inhomogeneous distribution of the magnetic environments due to site variations on the nanoparticle surface as well as a decrease in the rotational freedom of the oleic acid ligands.[197-199]

Figure 7.2. shows the powder X-ray diffraction (XRD) patterns for the $NaYF_4$: 2% Er^{3+}, 20% Yb^{3+}; $NaYF_4$: 2% Tm^{3+}, 20% Yb^{3+} and $NaYF_4$ NCs, as well as the calculated line pattern for α-$NaYF_4$. It is evident from the intensity of the peaks in the patterns obtained that the materials in question are highly crystalline in nature. The peak positions of all three patterns correspond closely to the reported and calculated patterns for cubic α-$NaYF_4$.[188, 194, 195] The calculated *d* spacing values for all three samples and the corresponding *h k l* values are given in Table 7.1. These values obtained from the nanocrystalline samples closely match the standard pattern of α-$NaYF_4$ (JCPDS: 6-0342) and no peaks from other phases or impurities were observed. The lattice constants for the $NaYF_4$: 2% Er^{3+}, 20% Yb^{3+}; $NaYF_4$: 2% Tm^{3+},20% Yb^{3+} and $NaYF_4$ NCs were calculated to be 5.519 Å, 5.515 Å, 5.517 Å, respectively which correspond closely to previously reported lattice constants of 5.485 Å and 5.47 Å for nanocrystalline[27] and bulk α-$NaYF_4$.[188] The broad nature of the observed diffraction peaks are an indication of the small size of the NCs. From the line broadening of the (111) diffraction peak of the $NaYF_4$: 2% Er^{3+}, 20% Yb^{3+} sample an average crystallite size of 25 nm was calculated using the Debye-Sherrer formula. This value matches closely to the particle size determined from the TEM results.

Figure 7.3.A-D shows photographs of a 1 wt% solution of $NaYF_4$: 2% Er^{3+}, 20% Yb^{3+} NCs in toluene. The transparency of the resulting colloidal solution is clearly demonstrated in the first image, Figure 7.1.A. Figure 7.3.B shows the total upconversion

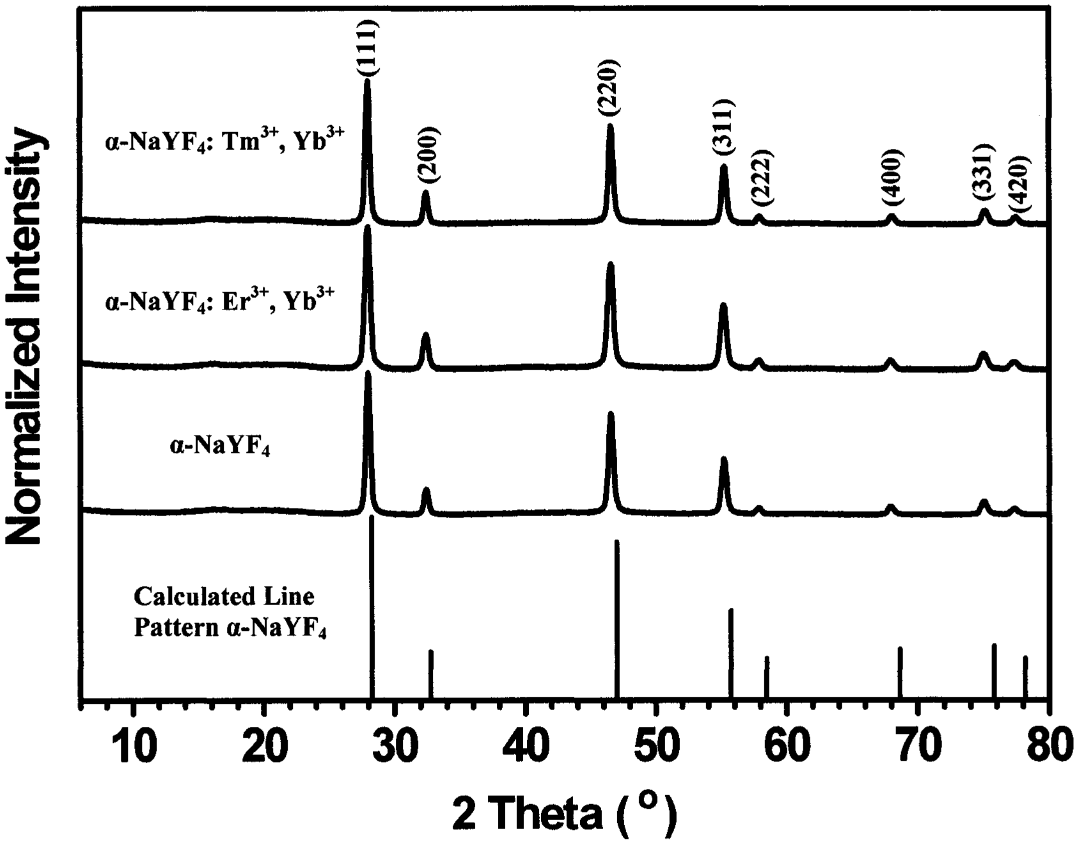

Figure 7.2. Experimental powder X-ray diffraction (XRD) patterns of α-$NaYF_4$, α-$NaYF_4$: 2% Er^{3+}, 20% Yb^{3+}, and α-$NaYF_4$: 2% Tm^{3+}, 20% Yb^{3+}nanocrystals. Calculated line pattern for α-$NaYF_4$ (bottom plot) is shown for reference.

luminescence of the same solution under 980 nm laser diode excitation into the $^2F_{7/2} \rightarrow {}^2F_{5/2}$ absorption of the Yb^{3+} ion with a power density of 100 W/cm^2. The total luminescence appears yellow-green in color due to a combination of green and red emissions from the Er^{3+} ion. This is apparent in Figure 7.3.C and D where the solution under the same excitation conditions is viewed through green and red filters, respectively, thus isolating the two separate emissions. Figure 7.3.E shows a 1 wt% solution of $NaYF_4$: 2% Tm^{3+}, 20% Yb^{3+} NCs in toluene under identical excitation conditions demonstrating a primarily blue luminescence in the visible region of the spectrum.

Table 7.1. *d*-spacing values for $NaYF_4$: 2% Er^{3+}, 20% Yb^{3+}; $NaYF_4$: 2% Tm^{3+}, 20% Yb^{3+}; and $NaYF_4$ determined via electron diffraction (ED) and X-ray diffraction (XRD).

	d-spacing values (Å)				
h k l	$NaYF_4$: 2% Er^{3+}, 20% Yb^{3+} (ED)	$NaYF_4$: 2% Er^{3+}, 20% Yb^{3+} (XRD)	$NaYF_4$: 2% Tm^{3+}, 20% Yb^{3+} (XRD)	$NaYF_4$ (XRD)	Standard Pattern (JCPDS: 6-0342)
1 1 1	3.15	3.19	3.19	3.19	3.14
2 0 0	2.72	2.76	2.76	2.76	2.73
2 2 0	1.92	1.95	1.95	1.95	1.93
3 1 1	1.64	1.66	1.66	1.66	1.64
2 2 2	1.57	1.59	1.59	1.59	1.57
4 0 0	1.36	1.38	1.38	1.38	1.36
3 3 1	1.26	1.27	1.27	1.26	1.25
4 2 0	1.22	1.23	1.23	1.23	1.22

The upconversion spectra both 1 wt% solutions of $NaYF_4$: 2% Er^{3+}, 20% Yb^{3+} and $NaYF_4$: 2% Tm^{3+}, 20% Yb^{3+} nanocrystals in toluene under 980 nm laser diode

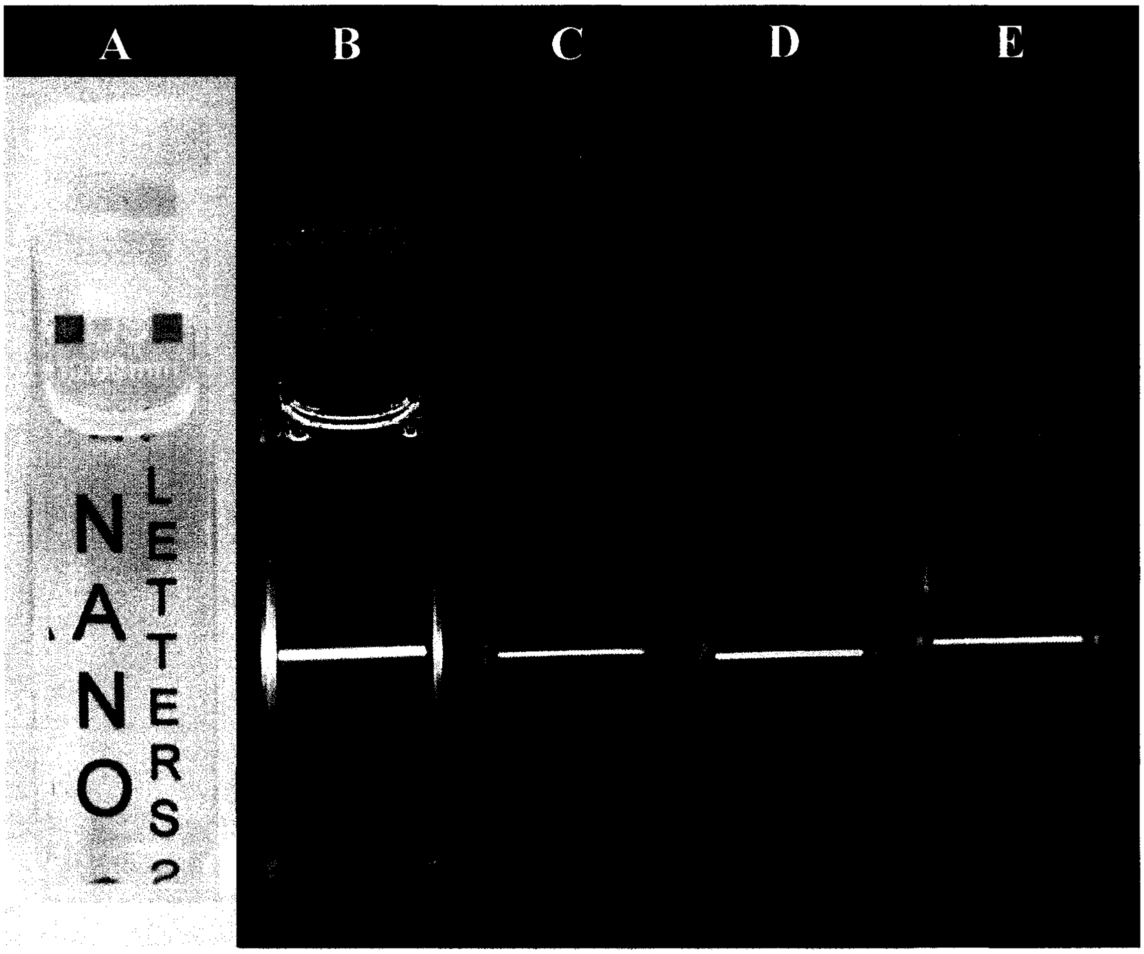

Figure 7.3. 1 wt.% colloidal solutions of nanocrystals in toluene excited with a 980 nm laser diode (power density = 100 W/cm^2) demonstrating upconversion luminescence. A) $NaYF_4$: 2% Er^{3+}, 20% Yb^{3+} solution showing its transparency. B) Total upconversion luminescence of $NaYF_4$: 2% Er^{3+}, 20% Yb^{3+} solution. C, D) $NaYF_4$: 2% Er^{3+}, 20% Yb^{3+} upconversion viewed through green and red filters, respectively. E) Total upconversion luminescence of $NaYF_4$: 2% Tm^{3+}, 20% Yb^{3+} solution.

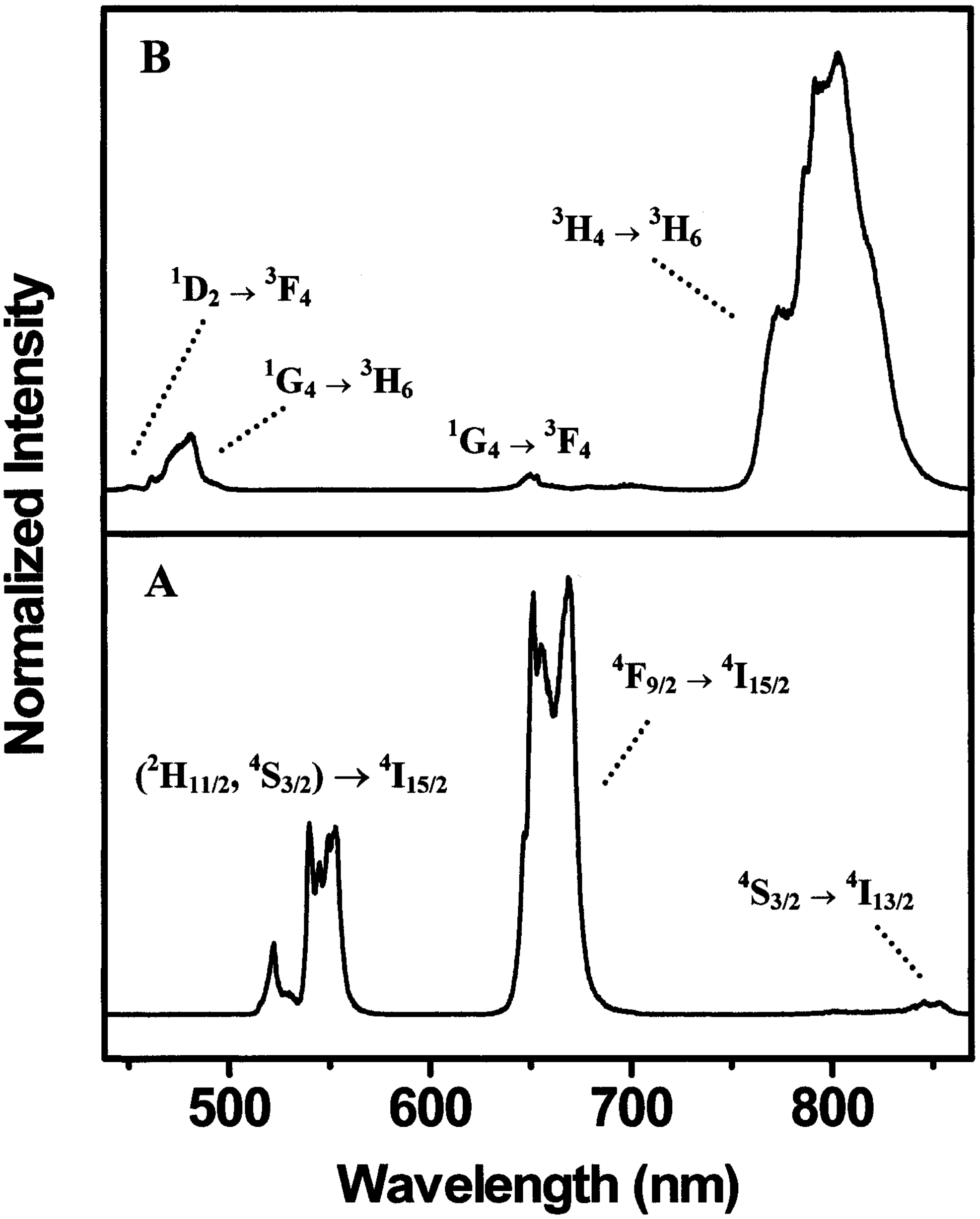

Figure 7.4. Luminescence emission spectra of 1 wt.% colloidal solutions of nanocrystals in toluene excited with a 980 nm laser diode. A) $NaYF_4$: 2% Er^{3+}, 20% Yb^{3+} and B) $NaYF_4$: 2% Tm^{3+}, 20% Yb^{3+}.

excitation (power density = 100 W/cm^2) are shown in Figure 7.4.A & B, respectively, and correspond to what has been reported previously for these materials.[27, 82] The emission bands can easily be assigned to transitions within the 4*f*-4*f* levels of the Er^{3+} and Tm^{3+} ions. The spectrum of the NaYF$_4$: 2% Er^{3+}, 20% Yb^{3+} sample (Figure 7.4.A) exhibits three distinct Er^{3+} emission bands. The green emissions between 510-530 nm and 530-570 nm were assigned to the $^2H_{11/2} \rightarrow {}^4I_{15/2}$ and $^4S_{3/2} \rightarrow {}^4I_{15/2}$ transitions, respectively. A dominant red emission was observed between 635-700 nm originating from the $^4F_{9/2} \rightarrow {}^4I_{15/2}$ transition as well as a weak NIR emission between 830-860 nm corresponding to the $^4S_{3/2} \rightarrow {}^4I_{13/2}$ transition. Four Tm^{3+} emission bands were observed in the NaYF$_4$: 2% Tm^{3+}, 20% Yb^{3+} sample (Figure 7.3.B) upon 980 nm laser diode excitation. The band observed in the blue region of the spectrum between 440-500 nm was assigned to the $^1D_2 \rightarrow {}^3F_4$ and $^1G_4 \rightarrow {}^3H_6$ transitions. A week red emission between 630-670 nm and an intense NIR emission between 750-850 nm were assigned to the $^1G_4 \rightarrow {}^3F_4$ and $^3H_4 \rightarrow {}^3H_6$ transitions, respectively.

In order to determine the number of photons responsible for the upconversion mechanism, the intensities of the upconversion emissions were recorded as a function of the 980 nm excitation intensity (Figure 7.5.). As seen in Figure 7.5.A, the green and red Er^{3+} upconversion emission intensities demonstrated quadratic power dependencies at low excitation densities indicating two photon upconversion mechanisms. For the Tm^{3+} doped sample (Figure 7.5.B), three and two photon power dependencies were observed for the $^1G_4 \rightarrow {}^3H_6$ and $^3H_4 \rightarrow {}^3H_6$ emissions at low excitation densities, respectively. The power dependencies of the Er^{3+} and Tm^{3+} upconversion emissions became linear at high excitation densities due to "saturation" of the upconversion processes.[200] Upconversion

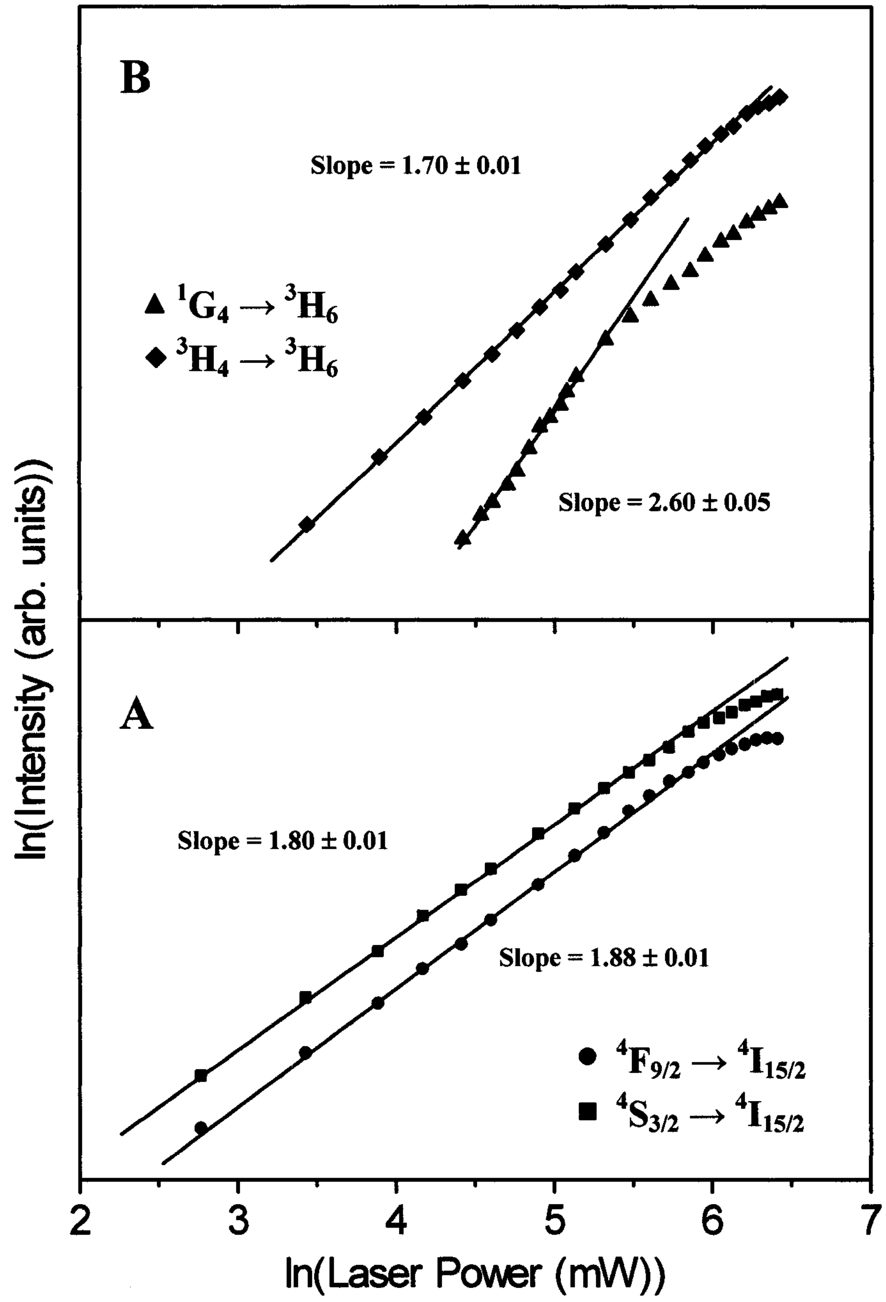

Figure 7.5. Power dependence of the upconverted emissions of 1 wt.% colloidal solutions of nanocrystals in toluene excited at 980 nm. A) $NaYF_4$: 2% Er^{3+}, 20% Yb^{3+} and B) $NaYF_4$: 2% Tm^{3+}, 20% Yb^{3+}. In the case of the $NaYF_4$: 2% Er^{3+}, 20% Yb^{3+} sample, the straight lines are least-squares fits to the low power data points.

is a nonlinear process; as such it will not maintain its nonlinear behavior up to infinite excitation energies as a consequence of the conservation of energy. Hence at high excitation densities, the power dependence of the upconversion luminescence intensity will become linear, and a "saturation" of the luminescence intensity is observed.

The upconversion excitation pathways for the Er^{3+}/Yb^{3+} and Tm^{3+}/Yb^{3+} ion couples in these materials are well known[201] and are shown in Figure 7.6. In the case of $NaYF_4$: 2% Er^{3+}, 20% Yb^{3+}, an initial energy transfer from an Yb^{3+} ion in the $^2F_{5/2}$ state to an Er^{3+} ion populates the $^4I_{11/2}$ level. A second 980 nm photon, or energy transfer from an Yb^{3+} ion, can then populate the $^4F_{7/2}$ level of the Er^{3+} ion. The Er^{3+} ion can then relax non-radiatively (without emission of photons) to the $^2H_{11/2}$ and $^4S_{3/2}$ levels and the green $^2H_{11/2} \rightarrow {}^4I_{15/2}$ and $^4S_{3/2} \rightarrow {}^4I_{15/2}$ emissions occur. Alternatively, the ion can further relax and populate the $^4F_{9/2}$ level leading to the red $^4F_{9/2} \rightarrow {}^4I_{15/2}$ emission. The $^4F_{9/2}$ level may also be populated from the $^4I_{13/2}$ level of the Er^{3+} ion by absorption of a 980 nm photon, or energy transfer from an Yb^{3+} ion, with the $^4I_{13/2}$ state being initially populated via the non-radiative $^4I_{11/2} \rightarrow {}^4I_{13/2}$ relaxation. For the $NaYF_4$: 2% Tm^{3+}, 20% Yb^{3+} sample, up to four subsequent energy transfers from Yb^{3+} ions populate the upper Tm^{3+} levels (Figure 7.6.) and the various emissions can occur.

In summary, we have prepared upconverting lanthanide-doped $NaYF_4$ nanocrystals (NCs) from the thermal decomposition reaction of trifluoroacetate precursors in a mixture of octadecene and oleic acid. The nanocrystals produced by this method are ~28 nm in diameter on average with an almost monodisperse particle size distribution. SAED and powder XRD indicate the nanocrystals are cubic α-$NaYF_4$. HRTEM show that the nanocrystals are highly crystalline and are composed of single

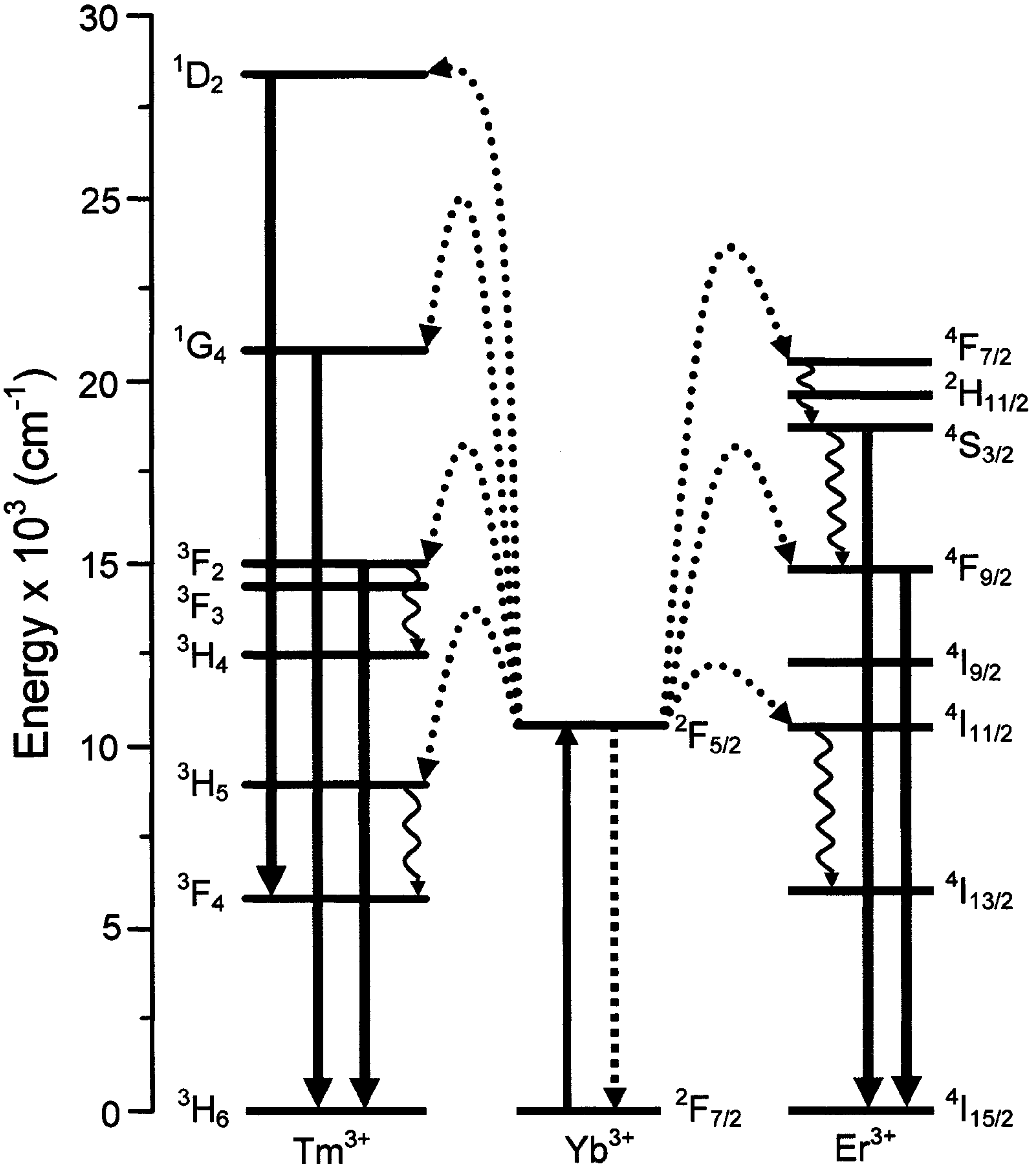

Figure 7.6. The energy level diagrams of the Er^{3+}, Tm^{3+} and Yb^{3+} dopant ions and upconversion mechanisms following 980 nm laser diode excitation. The full, dotted, and curly arrows represent emission, energy transfer and multiphonon relaxation processes, respectively.

crystallites. The Er^{3+}/Yb^{3+} and Tm^{3+}/Yb^{3+} doped nanocrystals are capable of upconverting NIR light from a 980 nm diode laser into red/green and blue light, respectively.

The synthetic method presented here is highly attractive as it uses techical grade solvents and ligands yet produces highly luminescent and uniform NCs. The synthesis does not require sophisticated equipment or complicated procedures and the resulting NCs are capable of being excited with a 980 nm laser diode thereby increasing their commercialization possibilities. Upconverting NCs have already been identified for potential use as biolabels and in biological assays. Further research is currently underway to modify the oleic acid-capped surface to obtain water-soluble particles required for these applications.

7.1. SUPPORTING INFORMATION

7.1.1. Synthesis of Ln^{3+} doped $NaYF_4$ nanocrystals

It should be noted beforehand that the decomposition of the metal trifluoroacetates produces various fluorinated and oxyfluorinated carbon species such as trifluoroacetic anhydride $(CF_3CO)_2O$, trifluoroacetyl fluoride CF_3CF_2COF, carbonyl difluoride COF_2 and tetrafluoroethylene C_2F_4. These species are considered toxic and as such the reaction should be carried out in a well ventilated hood. Care should also be exercised as not to inhale any of the evolved gases from the reaction.

All chemicals utilized in the synthesis of the nanocrystals were purchased from Aldrich. The lanthanide trifluoracetate precursors were prepared from the corresponding lanthanide and yttrium oxides and trifluoroacetic acid (99%). All oxides utilized were 99.99% purity or higher. In the case of the $NaYF_4$: Er^{3+} 2 mol%, Yb^{3+} 20 mol% codoped sample, 9.6 mg (0.025 mmol) of Er_2O_3, 98.5 mg (0.25 mmol) of Yb_2O_3, and 220.2 mg (0.975 mmol) of Y_2O_3 were dissolved in 10 mL of 50% aqueous trifluoroacetic acid at 80 °C in a three-neck round-bottom flask. The residual water and acid were then slowly evaporated to dryness at 60 °C. Sodium trifluoroacetate (98%) in the amount of 0.3400 g (2.5 mmol) was then added to the reaction vessel with 5 mL of octadecene (90%) and 10 mL of oleic acid (90%). A second solution of 15 mL of octadecene and 10 mL oleic acid was then prepared in a 100 mL three-neck round bottom flask. Both solutions were slowly heated to 125 °C under vacuum with magnetic stirring for 30 minutes to remove residual water and oxygen during which time the flask was purged periodically with dry argon gas. At this point, both solutions were clear with a slight yellow color. The second solution was then heated to 310 °C under Argon and maintained at this temperature. The lanthanide trifluoroacetate solution at 125 °C was then transferred dropwise into the second solution over a period of 15 minutes using a stainless steel cannula at a flow rate of ca. 1 mL/min. During this time the second solution was maintained at 310 °C. During the addition, the evolution of small gas bubbles was observed from the solution indicating the decomposition of the metal trifluoroacetates. Approximately 8-10 minutes into the addition of the trifluoroacetates, the reaction solution became turbid. After the addition was complete, the reaction mixture was lowered to 305 °C and kept at this temperature for 1 hr under dry argon during which time the solution became clear and a yellow colloidal solution was obtained. Subsequently, the mixture was allowed to cool to room temperature at which point the solution became turbid once again. The nanocrystals were precipitated by the addition of ethanol and isolated *via* centrifugation at 2000 rpm corresponding to a relative centrifugal field (RCF) of approximately 1000. The resulting pellet was then washed twice with ethanol and isolated *via* centrifugation at 2000 rpm each time. The resulting nanocrystals were dried in air for a minimum of 24 hrs. The resulting nanocrystals could be dispersed in nonpolar solvents (e.g. hexane, toluene, dichloromethane) by sonicating a suspension of the nanocrystals in a bath sonicator for 10-20 minutes. To aid in the dispersion of the nanocrystals, it was preferable to leave them in a 'muddy' state instead of the dry powder form.

It must be stated that the health and environmental effects of the synthesized $NaYF_4$ nanocrystals have yet to be determined fully. As a result, suitable precautions should be exercised when dealing with the powders and their colloidal solution. The use of appropriate eye and skin protection should always be employed when handling the materials.

7.1.2. NMR Measurements

The ^1H NMR spectrum of an undoped $NaYF_4$ sample dispersed in $CDCl_3$ was recorded using a Varian 300 MHz spectrometer. The spectrometer frequency was 300.03 MHz and 128 transients were recorded. The residual proton signal of the deuterated solvent was used as internal standards ($CDCl_3$ ^1H δ: 7.27 ppm). The ^1H NMR of free oleic acid was also obtained using the same experimental conditions for reference.

7.1.3. Powder X-ray Diffraction Analysis

The powder diffraction patterns were collected at room temperature with the $K\alpha$ (40 kV, 20 mA) radiation of Cu on a PW-1050 Philips diffractometer automated with the Difftech Sie-Ray system. Data accumulation and processing were carried out using the Difftech Sie-122 software. The scanning step size was 0.05° 2θ with a counting time of 10 s per step.

7.1.4. Transmission Electron Microscopy (TEM) Studies

TEM was performed on a $NaYF_4$: Er^{3+} 2%, Yb^{3+} 20% sample using a JEOL JEM-2000 FX microscope operating at 80 kV equipped with a charged-coupled device (CCD)-camera (Gatan). A small amount of the sample (~1 mg) was dispersed in 1 g of hexane to give an approximate 0.1 wt% solution. One drop of the resulting solution was allowed evaporated on a formvar/carbon film supported on a 300 mesh copper grid (3 mm in diameter). High resolution TEM was performed on the same sample using a 200 KeV JEOL JEM-2100F microscope.

7.1.5. Visible and NIR Room Temperature Upconversion Emission Spectroscopy (λ_{exc} = 980 nm)

The upconverted emission spectra were obtained using a Coherent 6-pin fibre-coupled F6 series 980 nm laser diode with a maximum power of 800 mW at 1260 mA. The laser was coupled to a 100 μm (core) fibre. For the upconversion studies, the samples were placed in 1 cm path-length quartz cuvettes (Hellma, QS). The visible emissions were collected from the samples at π/2 from the incident beam and then dispersed by a 1 m Jarrell-Ash Czerny-Turner double monochromator. Resolution of the monochromator was 0.2 nm with slit widths of 200 μm. The visible emissions from the sample exiting the monochromator were detected by a thermoelectrically cooled Hamamatsu R943-02 photomultiplier tube and the photomultiplied signals were processed by a Stanford Research Systems (SRS) model SR440 preamplifier. A Stanford Research Systems model SR 400 gated photon counter data acquisition system was used as an interface between the spectroscopic equipment and the computer running the SRS SR 465 data acquisition software.

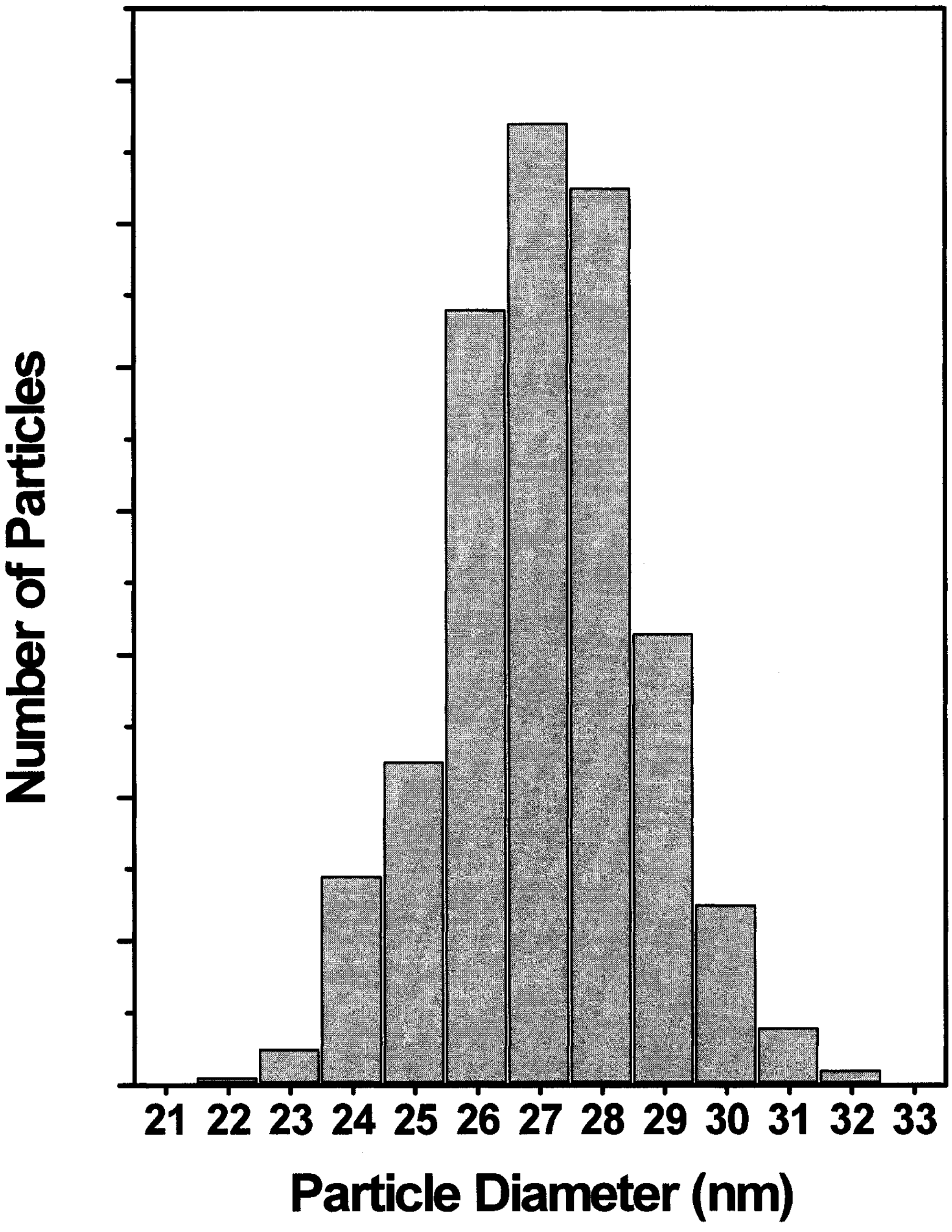

Figure 7.7. Histogram of the particle sizes obtained from TEM images of ~500 $NaYF_4$: 2% Er^{3+}, 20% Yb^{3+} nanocrystals (average particle size = 27.6 ± 1.6 nm).

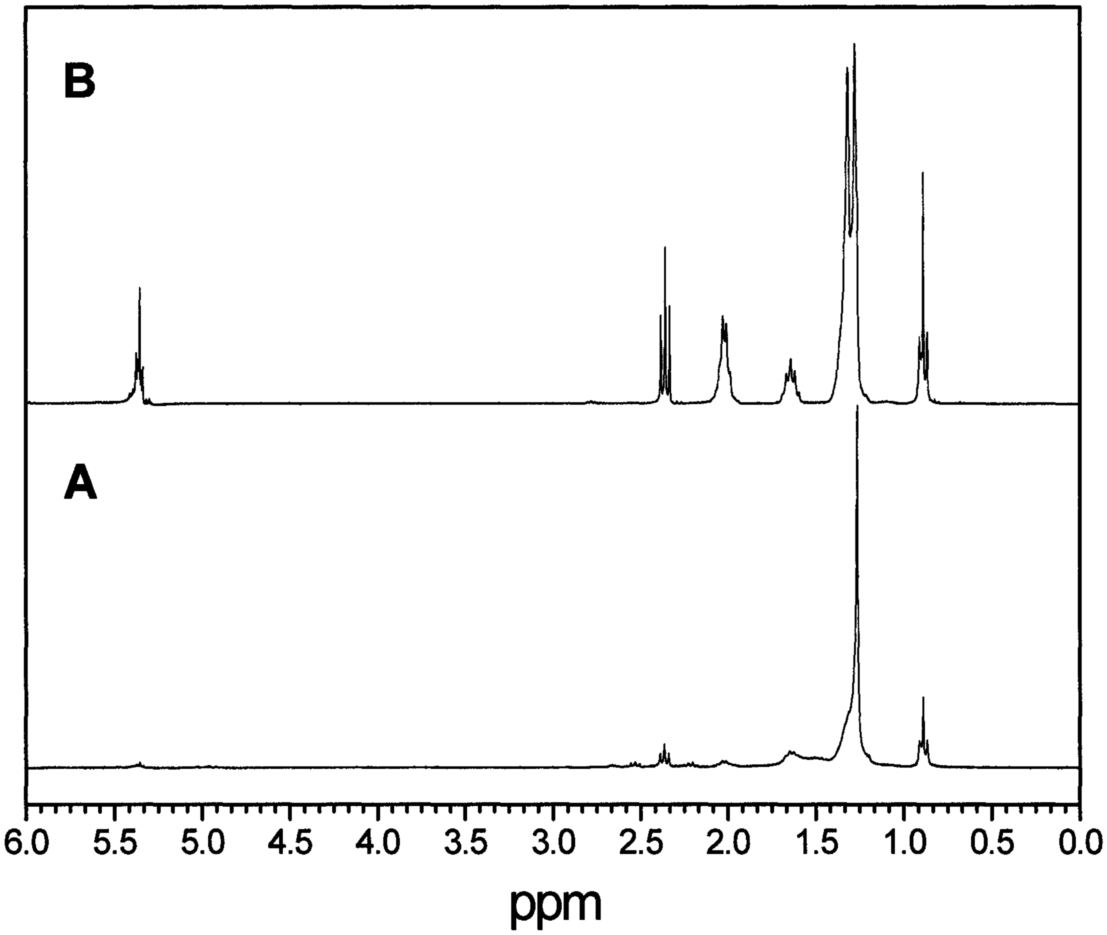

Figure 7.8. The ^{1}H NMR spectra of A) an undoped $NaYF_4$ sample and B) free oleic acid in $CDCl_3$ recorded on a Varian 300 MHz spectrometer. Chemical shifts for $NaYF_4$ sample are reported in parts-per-million δ: 5.3-5.45 (broad, -HC=CH-), 2.3-2.4 (broad, -CH_2-COOH), 2.0-2.1 (broad, CH_3-$(CH_2)_6$-CH_2-CH=CH-CH_2-$(CH_2)_6$-COOH), 1.2-1.4 (broad, -$(CH_2)_6$-) and 0.85-1.00 (broad, -CH_3).

7.2. AUTHOR'S NOTES AND SIGNIFICANCE OF THIS PAPER

The work presented here details our modification to an earlier synthetic method to obtain upconverting nanoparticles with uniform size and shape. This is the first reported synthesis of upconverting $NaYF_4$: Er^{3+}/Yb^{3+} and Tm^{3+}/Yb^{3+} nanocrystals with a truly monodisperse particle size and uniform shape. Previous synthetic methods presented in the literature resulted in particles with non-uniform shapes and a considerable particle size range. All the nanoparticles obtained could be colloidally dispersed in nonpolar solvents and upconvert 980 nm laser radiation to visible emissions. The synthesis used technical grade solvents thus reducing the cost of the synthesized nanoparticles. A relatively inexpensive 980 nm laser diode was use as the excitation source for the upconversion photos and spectra thus demonstrating the potential for commercialization of these nanoparticles. It is hoped that surface modifications can be made to the nanoparticles rendering them water soluble and opening the door to their potential use as biolabels and in biological assays.

Chapter 8

Conclusions and Future Work

8.1. CONCLUSIONS

In this thesis, the luminescence and upconversion properties of lanthanide-doped inorganic nanocrystals, specifically Y_2O_3, Lu_2O_3, $Gd_3Ga_5O_{12}$ and $NaYF_4$, synthesized by two immensely different synthetic methods have been investigated in detail. The Y_2O_3, Lu_2O_3, and $Gd_3Ga_5O_{12}$ nanocrystals were synthesized using a combustion synthesis technique that involved reacting metal nitrates (oxidizer) with an organic fuel such as glycine. In contrast, the lanthanide-doped $NaYF_4$ nanocrystals were synthesized via the thermal decomposition of metal trifluoroacetate precursors in a mixture of octadecene and oleic acid.

The optical and upconversion properties of Ho^{3+} doped nanocrystalline and bulk Y_2O_3 were investigated as a function of holmium concentration (0.1, 0.5, 1, 2, 5 and 10 mol%). Emission in the blue, green, red and NIR portions of the spectrum were observed after 457.9 nm excitation and attributed to the $^5F_3 \rightarrow {}^5I_8$, $({}^5F_4, {}^5S_2) \rightarrow {}^5I_8$, $^5F_5 \rightarrow {}^5I_8$, and $({}^5F_4, {}^5S_2) \rightarrow {}^5I_7$ transitions, respectively. The transition energies were similar for all samples investigated suggesting that the crystal field energy is not significantly affected by the type of host (nanocrystalline or bulk) or the amount of Ho^{3+} doping at the concentrations utilized in this study. However, the luminescence intensities of the emissions between the two sets of samples were shown to differ drastically, with the luminescence emissions in the bulk material being one order of magnitude greater than in the nanocrystalline samples. The decrease in luminescence efficiency in the nanocrystalline samples were attributed to adsorbed CO_3^{2-} and OH^- contaminants on the particle surface.

The presence of these contaminates on the surface of the nanocrystals was also reflected in the excited state lifetimes of these materials. In all nanocrystalline samples the decay curves of the $(^5F_4, ^5S_2) \rightarrow {}^5I_8$ transition were observed to deviate significantly from exponential behavior. This deviation was attributed to a distribution of dopant ions within the individual nanocrystals that are coupled in various degrees to the absorbed surface molecules. The distribution of ions thus results in a non-exponential decay as a significant portion of the dopant atoms reside near the surface of the particles.

Laser excitation at 646 nm resulted in blue and green upconversion luminescence in both the nanocrystalline and bulk samples. The blue and green emissions were assigned to the $^5F_3 \rightarrow {}^5I_8$ and $(^5F_4, ^5S_2) \rightarrow {}^5I_8$ transitions, respectively, and attributed to a two-photon excited-state absorption (ESA) upconversion process. Overall luminescence of the nanocrystalline samples under 646 nm pumping was again severely reduced due to the surface contaminants when compared to that of the bulk sample.

Near-infrared (NIR) excitation (754 nm) was noted to result in blue, green, and red upconversion emissions only in the bulk samples. In the case of the nanocrystalline samples, upconversion was found to be non-existent in the case of the 754 nm pumping, which was again attributed to absorbed atmospheric carbon dioxide and/or water on the surface of the nanocrystals. Similar to the case of 646 nm excitation, an ESA type mechanism was responsible for the observed upconversion luminescence.

The luminescent properties of 1 mol % Eu^{3+}-doped cubic Lu_2O_3 nanocrystals prepared by a combustion synthesis route were also investigated. These results were compared and contrasted to a bulk sample with micron particle sizes synthesized by conventional ceramic techniques. The emission spectra and lifetimes of the excited states of the nanocrystal samples were found to differ significantly from those of the bulk material. After excitation into the Eu^{3+}-O^{2-} charge transfer band with 257.25 nm radiation at room temperature and 78 K, emission was observed in the orange-red region of the spectrum resulting from the $^5D_0 \rightarrow {}^7F_0, {}^7F_1, {}^7F_2$ transitions. The unsplit $^5D_0 \rightarrow {}^7F_0$ line, attributed to Eu^{3+} ions in the C_2 site, in the nanocrystalline sample was found to be significantly broader than in the bulk; indicating a higher disorder of the Eu^{3+} crystalline environment. As well, the ratio of the integrated intensities of the $^5D_0 \rightarrow {}^7F_2$ and $^5D_0 \rightarrow {}^7F_1$ transitions under UV excitation was determined to be higher in the case of the nanocrystalline sample again indicating that the structural environment surrounding the dopant Eu^{3+} ion is distorted when compared to the bulk sample.

Site-selective spectroscopy experiments at room temperature revealed that energy-transfer from Eu^{3+} ions residing in C_{3i} sites to Eu^{3+} ions in C_2 sites occurs readily though the reverse energy-transfer is not nearly as efficient. The same experiments performed at 78 K revealed that the C_2 to C_{3i} energy transfer process is to a great extent reduced as it is a thermally activated process. The reverse is not true for the C_{3i} to C_2 energy transfer at 78 K as C_2 type emissions were still observed in both the bulk and nanocrystalline samples after selective C_{3i} excitation

The lifetimes of the $^5D_0$ excited state for both the C_2 and C_{3i} sites were found to be nearly double that found for the similarly doped bulk sample. This behavior was successfully attributed to a change in the refractive index of the nanocrystalline material that modifies the oscillator strength of the $4f \leftrightarrow 4f$ transitions. By fitting the decay curves of the $^5D_0$ level for both the C_2 and C_{3i} sites obtained by immersing the nanocrystals in media with different refractive indexes, it was found that the nanocrystals have a filling factor of 0.625.

From the emission spectra of the two samples, the Ω_2 and Ω_4 Judd-Ofelt intensity parameters were calculated using techniques adapted from the literature. The Judd-Ofelt parameters confirmed that the Eu^{3+} sites in the nanocrystalline sample are more disordered compared to the bulk sample. In addition, a higher observed R_{02} ratio in the nanocrystalline sample confirms that the Eu^{3+} environment is far more complex in the nanocrystals than in the bulk.

The luminescence and upconversion properties of a nanocrystalline $Gd_3Ga_5O_{12}$: 1% Ho^{3+} sample were investigated. Anti-Stokes blue ${}^5F_3 \rightarrow {}^5I_8$ and the green $({}^5F_4, {}^5S_2) \rightarrow {}^5I_8$ emissions were noted in the nanocrystalline $Gd_3Ga_5O_{12}$:Ho^{3+} sample after excitation into the ${}^5F_5$ level with 647 nm radiation. Power studies performed on both emissions revealed a two-photon upconversion mechanism. Temporal studies on the upconversion emissions demonstrated that the ${}^5I_7$ level was the intermediate state in the upconversion process. Based on these results, the anti-Stokes emissions were attributed to an excited state absorption (ESA) mechanism occurring via the ${}^5I_7$ level.

Excitation at 756 nm into the ${}^5I_4$ level of the nanocrystalline $Gd_3Ga_5O_{12}$: 1% Ho^{3+} sample resulted in green $({}^5F_4, {}^5S_2) \rightarrow {}^5I_8$ and red ${}^5F_5 \rightarrow {}^5I_8$ anti-Stokes emissions. As was the case with 647 nm excitation all of the upconversion emissions demonstrate a quadratic dependence on the excitation power indicating two-photon mechanisms. The temporal evolution of the green luminescence indicated a rise time corresponding to the lifetime of the ${}^5I_7$ level. Hence, a second excited state absorption (ESA) mechanism was proposed with the ${}^5I_7$ level as the intermediate state.

The effect of Yb^{3+} co-doping on the upconversion luminescence in nanocrystalline $Gd_3Ga_5O_{12}$:Ho^{3+} was also examined. Strong and efficient NIR to green anti-Stokes luminescence attributed to the ($^5F_4$, $^5S_2$) → $^5I_8$ transition was noted in nanocrystalline $Gd_3Ga_5O_{12}$:Ho^{3+}, Yb^{3+} after excitation into the $^2F_{5/2}$ level of Yb^{3+} with 978 nm radiation. Weaker blue, red and NIR anti-Stokes luminescence were also observed after 978 nm excitation and assigned to the $^5F_3$ → $^5I_8$, $^5F_5$ → $^5I_8$, and ($^5F_4$, $^5S_2$) → $^5I_7$ transitions, respectively.

Enhancement of the red $^5F_5$ → $^5I_8$ emission is observed relative to the green ($^5F_4$, $^5S_2$) → $^5I_8$ emission when the sample is irradiated with 978 nm radiation. The enhancement is attributed to two distinct energy transfer upconversion (ETU) mechanisms which independently populate the ($^5F_4$, $^5S_2$) and $^5F_5$ states. This was confirmed by measuring the upconversion temporal evolutions and the decay times of the IR levels that indicated the intermediate states in the two upconversion mechanisms are the $^5I_6$ and $^5I_7$ levels, respectively.

Upconverting Er^{3+}, Yb^{3+} and Tm^{3+}, Yb^{3+} doped $NaYF_4$ nanocrystals were synthesized via the thermal decomposition of trifluoroacetate precursors in a mixture of oleic acid and octadecene. This method provides highly luminescent nanoparticles through a simple one-pot technique with only one preparatory step. Transmission electron microscopy (TEM) indicated that the synthesized particles ranged in size from 10 to 50 nm, with the majority falling in the range between 15 to 30 nm. The powder X-ray diffraction (XRD) pattern of the $NaYF_4$: Er^{3+}, Yb^{3+} sample matched closely to the calculated pattern for cubic $NaYF_4$. The cubic $NaYF_4$: 2% Er^{3+}, 20% Yb^{3+} and $NaYF_4$: 2% Tm^{3+}, 20% Yb^{3+} nanocrystals were shown to be colloidally stable in nonpolar organic solvents and exhibit green/red and blue upconversion luminescence, respectively, under 977 nm laser excitation with a power density of 1.3 kW/cm^2.

The synthesis, characterization and spectroscopy of upconverting lanthanide-doped $NaYF_4$ nanocrystals with a defined shape and monodisperse particle size were also presented. The cubic $NaYF_4$ nanocrystals were synthesized via a thermal decomposition reaction of trifluoroacetate precursors in a mixture of technical grade chemicals, octadecene and the coordinating ligand oleic acid. In this straightforward method, the dissolved precursors are added slowly to the reaction solution through a stainless-steel cannula resulting in highly luminescent nanocrystals with an almost monodisperse particle size distribution. The average diameter of the nanocrystals was determined to be ~28 nm on average by Transmission electron microscopy (TEM). High resolution TEM images of individual nanocrystals indicated that they are highly crystalline and are composed of single crystallites. Selected area electron diffraction (SAED) and powder X-ray diffraction (XRD) revealed that the nanocrystals possessed a cubic crystal structure with a lattice cell parameter of 5.52 Å. The present of the oleic acid capping ligand was confirmed via ^1H NMR of an undoped $NaYF_4$ sample. The $NaYF_4$ nanocrystals are capable of being dispersed in nonpolar organic solvents thus forming colloidally stable solutions. The colloids of the Er^{3+}, Yb^{3+} and Tm^{3+}, Yb^{3+} doped nanocrystals exhibited green/red and blue upconversion luminescence, respectively, under 980 nm laser diode excitation with low power densities.

8.2 FUTURE WORK

The next step in the development of upconverting nanomaterials involves optimization of the current synthetic procedure to maximize their upconversion efficiencies. The $NaYF_4$ nanoparticles currently produced by this synthesis are cubic in phase, while the preferred phase for upconversion in the $NaYF_4$ system is the hexagonal phase. Thus it is of utmost importance to investigate modifications to the synthetic parameters to obtain hexagonal phase $NaYF_4$ nanoparticles.

Further increases in the upconversion efficiencies of these materials may also be obtained by changing the lanthanide ion doping levels in the nanoparticles. The current level of doping used in the synthesis of the nanoparticles is the optimal concentration for upconversion in the bulk materials. As it still not fully understood what effect synthesizing these materials in the nanoscale has on their upconversion properties, additional samples should be synthesized with a range of different lanthanide ion concentrations to identify the optimal doping levels. An added benefit of this research would be the synthesis of a range of nanoparticles with slightly different emitting colors, as modifying the dopant levels would also change the emission of the materials. In addition, other hosts should be examined as this will also modify the spectral response of the nanoparticles.

For these materials to ever be utilized in FRET based assays, modification of the surface must still be performed to render the nanoparticles dispersible in polar solvents such as water and buffer solutions. This may be achieved through two possible techniques. The first involves stripping the surface of the current ligand and replacing it with one with a water soluble head group facing out from the particle. This has possible disadvantageous such as irreversible agglomeration of the particles when the original surface ligand is stripped. The second method is the incorporation of phospholipids or surfactants into the hydrocarbon chains of the surface oleate ligands. In essence, a phospholipid bilayer is created that surrounds each individual nanoparticle thus making it water soluble.

Further work must also be directed at understanding the basic spectroscopy of the lanthanide ions in these dispersible nanoparticles. Almost all of the studies on these materials have focused on their synthesis and physical characterization for the most part ignoring their optical properties. No study has of yet fully investigated the effect of particle size on the optical properties of these dispersible upconverting materials. Further development of the synthetic procedure should be investigated to produce a range of samples with different particle sizes. Once synthesized, their optical properties should be thoroughly investigated. Studies on other luminescent lanthanide-doped nanocrystals have shown that a reduction in particle size has a drastic effect on the optical properties of the material due to increased surface effects. Thus it is of the utmost importance to full investigate the effect of particle size on the upconversion processes in nanocrystalline $NaYF_4$.

REFERENCES

1. Alivisatos, A. P. *J. Phys. Chem.* **1996,** *100* (31), 13226-13239.
2. El-Sayed, M. A. *Acc. Chem. Res.* **2004,** *37* (5), 326-333.
3. Brus, L. *J. Phys. Chem. Solids* **1998,** *59* (4), 459-465.
4. Banin, U.; Millo, O. *Annu. Rev. Phys. Chem.* **2003,** *54*, 465-492.
5. Bihari, B.; Eilers, H.; Tissue, B. M. *J. Lumin.* **1997,** *75* (1), 1-10.
6. Tissue, B. M. *Chem. Mater.* **1998,** *10*, 2837-2845.
7. Tissue, B. M.; Bihari, B. *J. Fluoresc.* **1998,** *8* (4), 289-294.
8. Tissue, B. M.; Eilers, H. *J. Soc. Inform. Displ.* **1996,** *4* (3), 213-217.
9. Boyer, J. C.; Vetrone, F.; Capobianco, J. A.; Speghini, A.; Bettinelli, M. *J. Phys. Chem. B* **2004,** *108*, 20137-20143.
10. Vetrone, F.; Boyer, J. C.; Capobianco, J. A., Luminescence, optical spectroscopy, and applications of rare earth doped Y_2O_3 nanocrystals. In *The Handbook of Luminescence, Display Materials and Devices*, Nalwa, H. S.; Rohwer, L. S., Eds. American Scientific Publishers: Los Angeles, CA, 2003; Vol. 2, pp 141-186.
11. Meltzer, R. S.; Feofilov, S. P.; Tissue, B. M.; Yuan, H. B. *Phys. Rev. B.* **1999,** *60*, R14012-R14015.
12. Bhargava, R. N. *J. Cryst. Growth* **2000,** *214-215*, 926-930.
13. Capobianco, J. A.; Boyer, J. C.; Vetrone, F.; Bettinelli, M.; Speghini, A. *Chem. Mater.* **2002,** *14* (7), 2915-2921.
14. Capobianco, J. A.; Vetrone, F.; Boyer, J. C.; Speghini, A.; Bettinelli, M. *J. Phys. Chem. B* **2002,** *106*, 1181-1187.
15. Capobianco, J. A.; Vetrone, F.; D'Alesio, T.; Tessari, G.; Speghini, A.; Bettinelli, M. *Phys. Chem. Chem. Phys.* **2000,** *2*, 3203-3207.
16. Capobianco, J. A.; Vetrone, F.; Boyer, J. C.; Speghini, A.; Bettinelli, M. *Opt. Mater.* **2002,** *19* (2), 259-268.
17. Michalet, X.; Pinaud, F.; Lacoste, T. D.; Dahan, M.; Bruchez, M. P.; Alivisatos, A. P.; Weiss, S. *Single Mol.* **2001,** *2* (4), 261-276.
18. Lee, H. Y.; Riehemann, W.; Mordike, B. L. *Z. Metallk.* **1993,** *84* (2), 79-84.
19. Borsella, E.; Botti, S.; Martelli, S. *Mater. Sci. Forum* **1997,** *235-236*, 261-266.
20. Vogt, G. *Proc. Electrochem. Soc.* **1988,** *88-5*, 572-583.
21. Sharma, P. K.; Jilavi, M. H.; Nab, R.; Schmidt, H. *J. Mater. Sci. Lett.* **1998,** *17* (10), 823-825.
22. Sharma, P. K.; Jilavi, M. H.; Nass, R.; Schmidt, H. *J. Lumin.* **1999,** *82* (3), 187-193.

23. Sharma, P. K.; Jilavi, M. H.; Schmidt, H.; Varadan, V. K. *Int. J. Inorg. Mater.* **2000,** *2* (5), 407-412.

24. Sharma, P. K.; Jilavi, M. H.; Varadan, V. K.; Schmidt, H. *J. Phys. Chem. Solids* **2002,** *63* (1), 171-177.

25. Sharma, P. K.; Nass, R.; Schmidt, H. *Opt. Mater.* **1998,** *10* (2), 161-169.

26. Heer, S.; Lehmann, O.; Haase, M.; Guedel, H.-U. *Angew. Chem. Int. Ed.* **2003,** *42*, 3179-3182.

27. Heer, S.; Koempe, K.; Guedel, H.-U.; Haase, M. *Adv. Mater.* **2004,** *16*, 2102-2105.

28. Aebischer, A.; Heer, S.; Biner, D.; Krämer, K.; Haase, M.; Güdel, H. U. *Chem. Phys. Lett.* **2005,** *407* (1-3), 124-128.

29. Suyver, J. F.; Aebischer, A.; Biner, D.; Gerner, P.; Grimm, J.; Heer, S.; Krämer, K. W.; Reinhard, C.; Güdel, H. U. *Opt. Mat.* **2005,** *27* (6), 1111-1130.

30. Lee, M. H.; Oh, S. G.; Yi, S. C. *J. Colloid Interface Sci.* **2000,** *226* (1), 65-70.

31. Lee, M. H.; Oh, S. G.; Yi, S. C.; Seo, D. S.; Hong, J. P.; Kim, C. O.; Yoo, Y. K.; Yoo, J. S. *J. Electrochem. Soc.* **2000,** *147* (8), 3139-3142.

32. Lemyre, J.-L.; Ritcey, A. M. *Chem. Mater.* **2005,** *17* (11), 3040-3043.

33. Hirai, T.; Orikoshi, T. *J. Colloid Interface Sci.* **2004,** *273* (2), 470-477.

34. Hirai, T.; Orikoshi, T. *J. Colloid Interface Sci.* **2004,** *269* (1), 103-108.

35. Hirai, T.; Orikoshi, T.; Komasawa, I. *Chem. Mater.* **2002,** *14* (8), 3576-3583.

36. Li, Q.; Gao, L.; Yan, D. *Chem. Mater.* **1999,** *11* (3), 533-535.

37. Feofilov, S. P.; Kaplyanskii, A. A.; Kulinkin, A. B.; Kutsenko, A. B.; Vasilevskaya, T. N.; Zakharchenya, R. I. *J. Sol-Gel Sci. Technol.* **2001,** *21* (3), 135-145.

38. Goldburt, E. T.; Kulkarni, B.; Bhargava, B. N.; Taylor, J.; Libera, M. *J. Lumin.* **1997,** *72-74*, 190-192.

39. Xu, C.; Watkins, B. A.; Sievers, R. E.; Jing, X.; Trowga, P.; Gibbons, C. S.; Vecht, A. *Appl. Phys. Lett.* **1997,** *71* (12), 1643-1645.

40. Ye, T.; Guiwen, Z.; Weiping, Z.; Shangda, X. *Mat. Res. Bull.* **1997,** *32*, 501-506.

41. Yu, X.; Xie, P.; Su, Q. *Phys. Chem. Chem. Phys.* **2001,** *3* (23), 5266-5269.

42. Tessari, G.; Bettinelli, M.; Speghini, A.; Ajò, D.; Pozza, G.; Depero, L. E.; Allieri, B.; Sangaletti, L. *Appl. Surf. Sci.* **1999,** *144-145*, 686-689.

43. Polizzi, S.; Fagherazzi, G.; Battagliarin, M.; Bettinelli, M.; Speghini, A. *J. Mater. Res.* **2001,** *16*, 146-154.

44. Fagherazzi, G.; Polizzi, S.; Bettinelli, M.; Speghini, A. *J. Mater. Res.* **2000,** *15*, 586-589.

45. Shea, L. E.; McKittrick, J.; Lopez, O. A. *J. Am. Ceram. Soc.* **1996,** *79* (12), 3257-3265.

46. Matteazzi, P.; Alcala, M. *Mater. Sci. Eng. A* **1997,** *A230* (1-2), 161-170.

47. Vetrone, F.; Boyer, J. C.; Capobianco, J. A.; Speghini, A.; Bettinelli, M. *Nanotechnology* **2004,** *15*, 75-81.

48. Cotton, F. A.; Wilkinson, G., *Advanced Inorganic Chemistry - 5th Edition*. John Wiley & Sons: New York, 1988.

49. Barrett, S. D.; Dhesi, S. S., *The Structure of Rare-Earth Metal Surfaces*. Imperial College Press: London, 2001.

50. Marinsky, J. A.; Glendenin, L. E.; Coryell, C. D. *J. Am. Chem. Soc.* **1947,** *69*, 2781-2785.

51. Hedrick, J. B. *J. Alloy Compd.* **1995,** *225*, 609-618.

52. Hedrick, J. B., Rare Earths. In *Minerals Yearbook, Vol. I, Metals & Minerals*, 1999.

53. Kramers, H. A. *Proc. Acad. Sci. Amsterdam* **1930,** *33*, 959-972.

54. Bethe, H. *Ann. Physik* **1930,** *60*, 218-233.

55. Becquerel, J. *Physik. Z.* **1908,** *9*, 94-100.

56. Vleck, J. H. V. *J. Phys. Chem.* **1937,** *41*, 67-80.

57. Carnall, W. T.; Crosswhite, H.; Crosswhite, H. M. *Energy level structure and transition probabilities in the spectra of the trivalent lanthanides in LaF_3*; Argonne National Laboratory: Argonne, IL, USA, 1978.

58. Carnall, W. T.; Fields, P. R.; Rajnak, K. *J. Chem. Phys.* **1968,** *49*, 4424-4442.

59. Carnall, W. T.; Fields, P. R.; Rajnak, K. *J. Chem. Phys.* **1968,** *49*, 4443-4446.

60. Carnall, W. T.; Fields, P. R.; Rajnak, K. *J. Chem. Phys.* **1968,** *49*, 4447-4449.

61. Carnall, W. T.; Fields, P. R.; Rajnak, K. *J. Chem. Phys.* **1968,** *49*, 4450-4455.

62. Dieke, G. H., *Spectra and Energy Levels of Rare Earth Ions in Crystals*. Interscience Publishers: New York, 1968; p 401.

63. Judd, B. R. *Phys. Rev.* **1962,** *127*, 750-761.

64. Ofelt, G. S. *J. Chem. Phys.* **1962,** *37*, 511-520.

65. Weber, M. J. *Phys. Rev.* **1967,** *157* (2), 262-272.

66. Weber, M. J. *Phys. Rev.* **1968,** *171* (2), 283-291.

67. Weber, M. J. *Phys. Rev. B* **1973,** *8* (1), 54-64.

68. Ronda, C. R.; Jüstel, T.; Nikol, H. *J. Alloy Compd.* **1998,** *275-277*, 669-676.

69. Buenzli, J.-C. G.; Piguet, C. *Chem. Soc. Rev.* **2005,** *34* (12), 1048-1077.

70. Evanics, F.; Diamente, P. R.; Veggel, F. C. J. M. V.; Stanisz, G. J.; Prosser, R. S. *Chem. Mater.* **2006,** *18* (10), 2499-2505.

71. Scheps, R. *Prog. Quant. Electron.* **1996,** *20* (4), 271-358.

72. Auzel, F. *Chem. Rev.* **2004,** *104* (1), 139-173.

73. Auzel, F. E. *Proc. IEEE* **1973,** *61*, 758-786.

74. Auzel, F. *J. Lumin.* **1990,** *45*, 341-345.

75. Wright, J., Up-conversion and excited-state energy transfer in rare-earth doped materials. In *Radiationless Processes in Molecules and Condensed Phases*, Fong, F. K., Ed. Springer: New York, 1976; Vol. 15, p 239.

76. Bloembergen, N. *Phys. Rev. Lett.* **1959,** *2*, 84-85.

77. Auzel, F. *C. R. Acad. Sci. (Paris)* **1966,** *262*, 1016-1019.

78. Joubert, M. F. *Opt. Mater.* **1999,** *11* (2), 181-203.

79. Boyer, J. C.; Vetrone, F.; Capobianco, J. A.; Speghini, A.; Bettinelli, M. *J. Appl. Phys.* **2003,** *93*, 9460-9465.

80. Boyer, J. C.; Vetrone, F.; Capobianco, J. A.; Speghini, A.; Bettinelli, M. *Chem. Phys. Lett.* **2004,** *390*, 403-407.

81. Boyer, J. C.; Vetrone, F.; Capobianco, J. A.; Speghini, A.; Zambelli, M.; Bettinelli, M. *J. Lumin.* **2004,** *106* (3-4), 263-268.

82. Boyer, J.-C.; Vetrone, F.; Cuccia, L. A.; Capobianco, J. A. *J. Am. Chem. Soc.* **2006,** *128* (23), 7444-7445.

83. Vetrone, F.; Capobianco, J. A.; Boyer, J. C.; Speghini, A.; Bettinelli, M. *J. Phys. Chem. B* **2002,** *106*, 5622-5628.

84. Vetrone, F.; Boyer, J. C.; Capobianco, J. A.; Speghini, A.; Bettinelli, M. *J. Phys. Chem. B* **2003,** *107* (5), 1107-1112.

85. Igarashi, T.; Ihara, M.; Kusunoki, T.; Ohno, K. *Appl. Phys. Lett.* **2000,** *76* (12), 1549-1551.

86. Wakefield, G.; Holland, E.; Dobson, P. J.; Hutchison, J. L. *Adv. Mater.* **2001,** *13* (20), 1557-1560.

87. Wakefield, G.; Keron, H. A.; Dobson, P. J.; Hutchison, J. L. *J. Colloid Interface Sci.* **1999,** *215* (1), 179-182.

88. Vetrone, F.; Boyer, J. C.; Capobianco, J. A.; Speghini, A.; Bettinelli, M. *J. Phys. Chem. B* **2002,** *106* (22), 5622-5628.

89. Laversenne, L.; Guyot, Y.; Goutaudier, C.; Cohen-Adad, M. T.; Boulon, G. *Opt. Mater.* **2001,** *16* (4), 475-483.

90. Laversenne, L.; Kairouani, S.; Guyot, Y.; Goutaudier, C.; Boulon, G.; Cohen-Adad, M. T. *Opt. Mater.* **2002,** *19* (1), 59-66.

91. Sugak, D.; Matkovskii, A.; Durygin, A.; Suchocki, A.; Solskii, I.; Ubizskii, S.; Kopczynski, K.; Mierczyk, Z.; Potera, P. *J. Lumin.* **1999,** *82* (9-15).

92. Gill, D. S.; Anderson, A. A.; Eason, R. W.; Warburton, T. J.; Shepherd, D. P. *Appl. Phys. Lett.* **1996,** *69*, 10-12.

93. Brenier, A.; Courrol, L. C.; Pédrini, C.; Madej, C.; Boulon, G. *Phys. Rev. B* **1994,** *49* (2), 881-887.

94. Brenier, A.; Courrol, L. C.; Pédrini, C.; Madej, C.; Boulon, G. *Opt. Mater.* **1994,** *3*, 25-33.

95. Brenier, A.; Courrol, L. C.; Pédrini, C.; Madej, C.; Boulon, G. *J. Lumin.* **1994,** *58*, 284-286.

96. Brenier, A.; Courrol, L. C.; Pédrini, C.; Madej, C.; Boulon, G. *J. Lumin.* **1994,** *60&61*, 870-873.

97. Brenier, A.; Garapon, C.; Madej, C.; Pédrini, C.; Boulon, G. *J. Phys. IV* **1994,** *4*, 431-434.

98. Brenier, A.; Madej, C.; Pédrini, C.; Boulon, G. *Radiat Eff. Defects Solids* **1995,** *135*, 73-76.

99. Boulon, G.; Laversenne, L.; Goutaudier, C.; Y.Guyot; Cohen-Adad, M. T. *J. Lumin.* **2003,** *102-103*, 417-425.

100. Polizzi, S.; Battagliarin, M.; Bettinelli, M.; Speghini, A.; Fagherazzi, G. *J. Mater. Chem.* **2002,** *12* (3), 742-747.

101. Zhang, Y.-W.; Sun, X.; Si, R.; You, L.-P.; Yan, C.-H. *J. Am. Chem. Soc.* **2005,** *127* (10), 3260-3261.

102. Mai, H.-X.; Zhang, Y.-W.; Si, R.; Yan, Z.-G.; Sun, L.; You, L.-P.; Yan, C.-H. *J. Am. Chem. Soc.* **2006,** *128* (19), 6426-6436.

103. Zeng, J.-H.; Su, J.; Li, Z.-H.; Yan, R.-X.; Li, Y.-D. *Adv. Mater.* **2005,** *17* (17), 2119-2123.

104. Suyver, J. F.; Grimm, J.; Veen, M. K. v.; Biner, D.; Krämer, K. W.; Güdel, H. U. *J. Lumin.* **2006,** *117* (1), 1-12.

105. Suyver, J. F.; Grimm, J.; Krämer, K. W.; Güdel, H. U. *J. Lumin.* **2005,** *114* (1), 53-59.

106. Wang, L.; Li, Y. *Chem. Comm.* **2006,** *24*, 2557-2559.

107. Wang, L.; Yan, R.; Huo, Z.; Wang, L.; Zeng, J.; Bao, J.; Wang, X.; Peng, Q.; Li, Y. *Angew. Chem. Int. Ed.* **2005,** *44* (37), 6054-6057.

108. Wagner, C. N. J. In *Local atomic arrangements studied by X-ray diffraction*, Metallurgical Society Conference, New York, 1966; Cohen, J. B.; Hilliard, J. E., Eds. Gordon & Breach: New York, 1966; pp 219-268.

109. Rüssel, C. *J. Non-Cryst. Solids* **1993,** *152* (2-3), 161-166.

110. Rüssel, C. *J. Mater. Sci. Lett.* **1992,** *11* (3), 152-154.

111. Rillings, K. W.; Roberts, J. E. *Thermochim. Acta* **1974,** *10* (3), 285-98.

112. Yu, W. W.; Peng, X. *Angew. Chem. Int. Ed.* **2002,** *41* (13), 2368-2371.

113. Park, J.; An, K.; Hwang, Y.; Park, J.-G.; Noh, H.-J.; Kim, J.-Y.; Park, J.-H.; Hwang, N.-M.; Hyeon, T. *Nat. Mater.* **2004,** *3* (12), 891-895.

114. Kuningas, K.; Rantanen, T.; Ukonaho, T.; Lövgren, T.; Soukka, T. *Anal. Chem.* **2005,** *77* (22), 7348-7355.

115. Holm, B. A.; Bergey, E. J.; De, T.; Rodman, D. J.; Kapoor, R.; Levy, L.; Friend, C. S.; Prasad, P. N. *Mol. Cryst. Liq. Cryst.* **2002,** *374*, 589-598.

116. Hampl, J.; Hall, M.; Mufti, N. A.; Yao, Y.-M. M.; MacQueen, D. B.; Wright, W. H.; Cooper, D. E. *Anal. Biochem.* **2001,** *288* (2), 176-187.

117. Niedbala, R. S.; Feindt, H.; Kardos, K.; Vail, T.; Burton, J.; Bielska, B.; Li, S.; Milunic, D.; Bourdelle, P.; Vallejo, R. *Anal. Biochem.* **2001,** *293* (1), 22-30.

118. Morgan, C. G.; Mitchell, A. C. *Biosens. Bioelectron.* **2006,** *doi:10.1016/j.bios.2006.08.024.*

119. Franz, K. A.; Kehr, W. G.; Siggel, A.; Wieczoreck, J., Luminescent Materials. In *Ullman's Encyclopedia of Industrial Chemistry*, Elvers, B.; Hawkins, S.; Schulz, G., Eds. VCH Publishers: Weinheim, Germany, 1985; Vol. A15.

120. Eilers, H.; Tissue, B. M. *Chem. Phys. Lett.* **1996,** *251*, 74-78.

121. Williams, D. K.; Bihari, B.; Tissue, B. M.; McHale, J. M. *J. Phys. Chem. B* **1998,** *102*, 916-920.

122. Williams, D. K.; Yuan, H.; Tissue, B. M. *J. Lumin.* **1999,** *83-84*, 297-300.

123. Kuck, S.; Sokolska, I. *Chem. Phys. Lett.* **2000,** *325*, 257-263.

124. Malinowski, M.; Wnuk, A.; Frukacz, Z.; Chadeyron, G.; Mahiou, R.; Guy, S.; Joubert, M. F. *J. Alloys Comp.* **2001,** *323-324*, 721-735.

125. Allain, J. Y.; Monerie, M.; Poignant, H. *Electron. Lett.* **1990,** *26* (4), 261-262.

126. Funk, D. S.; Eden, J. G. *IEEE J. Sel. Top. Quant.* **1995,** *1* (3), 784-791.

127. Funk, D. S.; Stevens, S. B.; Wu, S. S.; Eden, J. G. *IEEE J. Quantum Electron.* **1996,** *32* (4), 638-645.

128. Funk, D. S.; Eden, J. G.; Osinski, J. S.; Lu, B. *Electron. Lett.* **1997,** *33* (23), 1958-1960.

129. Zhang, H. X.; Kam, C. H.; Zhou, Y.; Han, H. Q.; Buddhudu, S.; Lam, Y. L. *Opt. Mater.* **2000,** *15* (1), 47-50.

130. Blasse, G. *Prog. Solid St. Chem.* **1988,** *18*, 79-171.

131. Leavitt, R. P.; Gruber, J. B.; Chang, N. C.; Morrison, C. A. *J. Chem. Phys.* **1982,** *76* (10), 4775-4788.

132. Riseberg, L. A.; Moos, H. W. *Phys. Rev.* **1968,** *174* (2), 429-438.

133. Shojiya, M.; Kawamoto, Y.; Kadona, K. *J. Appl. Phys.* **2001,** *89* (9), 4944-4950.

134. Malinowski, M.; Piramidowicz, R.; Frukacz, Z.; Chadeyron, G.; Mahiou, R.; Joubert, M. F. *Opt. Mater.* **1999,** *12*, 409-423.

135. Layne, C. B.; Lowdermilk, W. H.; Weber, M. J. *Phys. Rev. B* **1977,** *16* (1), 10-20.

136. Chamarro, A.; Cases, R. *J. Lumin.* **1990,** *46*, 59.

137. Hirao, K.; Kishimoto, S.; Tanaka, K.; Tanabe, S.; Soga, N. *J. Non-Cryst. Solids* **1992,** *139*, 151-156.

138. Vetrone, F.; Boyer, J. C.; Capobianco, J. A.; Speghini, A.; Bettinelli, M. *Chem. Mater.* **2003,** *15*, 2737-2743.

139. Polizzi, S.; Bucella, S.; Speghini, A.; Vetrone, F.; Naccache, R.; Boyer, J. C.; Capobianco, J. A. *Chem. Mater.* **2004,** *16* (7), 1330-1335.

140. Laroche, M.; Girard, S.; Moncorg, R.; Bettinelli, M.; Abdulsabirov, R.; Semashko, V. *Opt. Mater.* **2003,** *22*, 147-154.

141. Rambaldi, P.; Moncorgé, R.; Wolf, J. P.; Pédrini, C.; Gesland, J. Y. *Optics Commun.* **1998,** *146*, 163-166.

142. Guillot-Noel, O.; Bellamy, B.; Viana, B.; Gourier, D. *Phys. Rev. B* **1999,** *66* (3), 1668-1677.

143. Maunier, C.; Doualan, J. L.; Moncorgé, R.; Speghini, A.; Bettinelli, M.; Cavalli, E. *J. Opt. Soc. Am. B* **2002,** *19* (8), 1794-1800.

144. Moine, B.; Dujardin, C.; Lautesse, H.; Pedrini, C.; Combes, C. M.; Belski, A.; Martin, P.; Gesland, J. Y. *Mat. Sci. Forum* **1997,** *239-241*, 245-248.

145. Zych, E. *J. Phys.: Condens. Matter* **2002,** *14* (22), 5637-5650.

146. Zych, E. *J. Alloys Compd.* **2002,** *344* (1-2), 332-336.

147. Zych, E.; Hreniak, D.; Strek, W. *J. Phys. Chem. B* **2002,** *106* (15), 3805-3812.

148. Lempicki, A.; Brecher, C.; Szupryczynski, P.; Lingertat, H.; Nagarkar, V. V.; Tipnis, S. V.; R.Miller, S. *Nucl. Instrum. Methods Phys. Res., Sect. A* **2002,** *488* (3), 579-590.

149. Saiki, A.; Ishizawa, N.; Mizutani, N.; Kato, M. *J. Ceram. Soc. Japan* **1985,** *93*, 649-654.

150. Concas, G.; Spano, G.; Bettinelli, M.; Speghini, A. *Z. Naturforsch., A: Phys. Sci.* **2003,** *58* (9/10), 551-557.

151. Buijs, m.; Meyerink, A.; Blasse, G. *J. Lumin.* **1987,** *37*, 9-20.

152. Heber, J.; Hellwege, K. H.; Köbler, U.; Murmann, H. *Z. Physik.* **1970,** *237*, 189-204.

153. Zych, E.; Karbowiak, M.; Domagala, K.; Hubert, S. *J. Alloys Compd.* **2002,** *341* (1-2), 381-384.

154. M. Karbowiak, E. Z., J. Hölsä. *J. Phys.: Condens. Matter* **2003,** *15* (13), 2169-2181.

155. Oomen, E. W. J. L.; Dongen, A. M. A. v. *J. Non-Cryst. Solids* **1989,** *111* (2-3), 205-13.

156. Peacock, R. D., *The Intensities of Lanthanide f - f Transitions*. Springer - Verlag: New York, 1975; Vol. 22, p 39.

157. Kashida, T. *Phys. Rev.* **1969,** *185*, 500-508.

158. Yen, W. M.; Scott, W. C.; Schawlow, A. L. *Phys. Rev.* **1964,** *136*, A271-A283.

159. Chen, G.; Haire, R. G.; Peterson, J. R. *J. Solid State Chem.* **1993,** *102*, 126-131.

160. Henderson, B.; Imbusch, G. F., *Optical Spectroscopy of Inorganic Solids*. Clarendon Press: Oxford, 1989.

161. Medenbach, O.; Dettmar, D.; Shannon, R. D.; Fischer, R. X.; Yen, W. M. *J. Opt. A: Pure Appl. Opt.* **2001,** *3* (3), 174-177.

162. Huang, J.; Loriers, J.; Porcher, P. *C.R. Acad. Sci., Ser. II* **1982,** *294* (9), 545-548.

163. Malta, O. L.; Brito, H. F.; Menezes, J. F. S.; Goncalves de Silva, F. R.; Alves, S.; Farias, F. S.; de Andrade, A. V. M. *J. Lumin.* **1997,** *75* (3), 255-268.

164. Thorne, A. P., *Spectrophysics*. 2 ed.; Chapman and Hall: New York, 1988; p 390.

165. Kodaira, C. A.; Claudia, A.; Brito, H. F.; Felinto, M. C. F. C. *J. Solid State Chem.* **2003,** *171* (1-2), 401-407.

166. Lupei, V. *Opt. Mater.* **2002,** *19*, 95-107.

167. Wang, Q.; Zhang, S.; Wu, S.; Dong, X. *J. Lumin.* **1988,** *40-41*, 181-182.

168. Kir'yanov, A. V.; Aboites, V.; Belovolov, A. M.; Timoshechkin, M. I.; Belovolov, M. I.; Damzen, M. J.; Minassian, A. *Opt. Express* **2002,** *10*, 832-839.

169. Suchocki, A.; Koziarsha, B.; Brenier, A.; Pedrini, C.; Boulon, G. *J. Alloys Compd.* **1995,** *225* (1-2), 559-563.

170. Polizzi, S. *In preparation.*

171. Capobianco, J. A.; Raspa, N.; Monteil, A.; Malinowski, M. *J. Phys.: Condens. Matter* **1993,** *5*, 6083-6090.

172. Zou, X.; Torantani, H. *J. Non-Cryst. Solids* **1996,** *201*, 37-46.

173. Vetrone, F.; Boyer, J. C.; Capobianco, J. A.; Speghini, A.; Bettinelli, M. *J. Chem. Phys. B* **2003,** *submitted.*

174. Zhang, X.; Jouart, J.-P.; Mary, G. *J. Phys. : Condens. Matter* **1998,** *10*, 493-500.

175. Martín, I. R.; Rodríquez, V. D.; Lavín, V.; Rodríguez-Mendoza, U. R. *J. Alloys Compd.* **1998,** *275-277*, 345-348.

176. Diening, A.; Kück, S. *J. Appl. Phys.* **2000,** *87* (9), 4063-4068.

177. Nakazawa, E., In *Phosphor Handbook*, Shionoya, S.; Yen, W. M., Eds. CRC Press: Boca Raton, 1999; pp 101-112.

178. Pollnau, M.; Gamelin, D. R.; Lüthi, S. R.; Güdel, H. U.; Hehlen, M. P. *Phys. Rev. B* **2000,** *61* (5), 3337-3346.

179. Nakazawa, E. *J. Lumin.* **1976,** *12-13*, 675-680.

180. Nakazawa, E.; Shionoya, S. *Phys. Rev. Lett.* **1970,** *25* (25), 1710-1712.

181. Corstjens, P. L. A. M.; Li, S.; Zuiderwijk, M.; Kardos, K.; Abrams, W. R.; Niedbala, R. S.; Tanke, H. J. *IEEE Proc.-Nanobiotechnol.* **2005,** *152* (2), 64-72.

182. Rijke, F. v. d.; Zijlmans, H.; Li, S.; Vail, T.; Raap, A. K.; Niedbala, R. S.; Tanke, H. J. *Nat. Biotechnol.* **2001,** *19* (3)), 273-276.

183. Zijlmans, H. J. M. A. A.; Bonnet, J.; Burton, J.; Kardos, K.; Vail, T.; Niedbala, R. S.; Tanke, H. J. *Anal. Biochem.* **1999,** *267* (1), 30-36.

184. Denk, W.; Strickler, J. H.; Webb, W. W. *Science* **1990,** *248* (4951), 73-76.

185. König, K. *J. Microsc.* **2000,** *200* (2), 83-104.

186. Larson, D. R.; Zipfel, W. R.; Williams, R. M.; Clark, S. W.; Bruchez, M. P.; Wise, F. W.; Webb, W. W. *Science* **2003,** *300* (5624), 1434-1437.

187. Krämer, K. W.; Biner, D.; Frei, G.; Güdel, H. U.; Hehlen, M. P.; Lüthi, S. R. *Chem. Mater.* **2004,** *16* (7), 1244-1251.

188. Roy, D. M.; Roy, R. *J. Electrochem. Soc.* **1964,** *111* (4), 421-429.

189. Lu, H.; Yi, G.; Zhao, S.; Chen, D.; Guo, L.-H.; Cheng, J. *J. Mater. Chem.* **2004,** *14* (8), 1336-1341.

190. Yi, G.; Lu, H.; Zhao, S.; Ge, Y.; Yang, W.; Chen, D.; Guo, L.-H. *Nano Lett.* **2004,** *4* (11), 2191-2196.

191. Sivakumar, S.; Veggel, F. C. J. M. V.; Raudsepp, M. *J. Amer. Chem. Soc.* **2005,** *127* (36), 12464-12465.

192. Lim, S. F.; Riehn, R.; Ryu, W. S.; Khanarian, N.; Tung, C.-K.; Tank, D.; Austin, R. H. *Nano Lett.* **2006,** *6* (2), 169-174.

193. Wagener, U.; Rüssel, C. *J. Non-Cryst. Solids* **1993,** *152* (2-3), 167-171.

194. Pol, P. G.; Rao, V. J. *Indian J. Pure Appl. Phys.* **1973,** *11* (12), 886-8.

195. Reddy, K.; Narasimha, S.; Shareef, M. A. H.; Pandaraiah, N. *J. Mater. Sci. Lett.* **1983,** *2* (2), 83-84.

196. Wang, Z. L. *J. Phys. Chem. B* **2000,** *104* (6), 1153-1175.

197. Sudarsan, V.; Sivakumar, S.; Veggel, F. C. J. M. v. *Chem. Mater.* **2005,** *17* (18), 4736-4742.

198. Sachleben, J. R.; Wooten, E. W.; Emsley, L.; Pines, A.; Colvin, V. L.; Alivisatos, A. P. *Chem. Phys. Lett.* **1992,** *198* (5), 431-436.

199. Kuno, M.; Lee, J. K.; Dabbousi, B. O.; Mikulec, F. V.; Bawendi, M. G. *J. Chem. Phys.* **1997,** *23*, 9869-9882.

200. Pollnau, M.; Gamelin, D. R.; Lüthi, S. R.; Güdel, H. U. *Phys. Rev. B* **1999,** *61* (5), 3337-3346.

201. Page, R. H.; Schaffers, K. I.; Waide, P. A.; Tassano, J. B.; Payne, S. A.; Krupke, W. F. *J. Opt. Soc. Am. B* **1998,** *15*, 996-1008.